PRESSURE DROP DURING REFLUX CONDENSATION OF STEAM IN AN INCLINED ELLIPTICAL TUBE

By

Paul David Schoenfeld

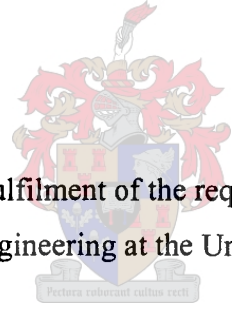

Thesis presented in partial fulfilment of the requirements for the degree of Master of Mechanical Engineering at the University of Stellenbosch

Promoter: PROF. DR.-ING D.G. KRÖGER

Department of Mechanical Engineering
University of Stellenbosch
September 1998

DECLARATION

I, the undersigned, hereby declare that the work contained in this thesis is my own original work and has not previously in its entirety or in part been submitted at any university for a degree.

This 30 th day of November 1998

OPSOMMING

'n Model is deur Zapke en Kröger ontwikkel om die drukval in plat buise wat in teenvloei kondensers gebruik word te bereken. Hierdie model is op adiabatiese twee-fase teenvloei eksperimente gebaseer en sluit die teorie oor wrywing tydens kondensasie deur Groenewald in. Zapke het ook 'n korrelasie ontwikkel waarmee die vloedingsnelheid tydens adiabatiese teenvloei voorspel mag word. Die toepaslikheid van beide die drukval model en die vloedingskorrelasie op teenvloei kondensasie is egter voor hierdie ondersoek nog nie eksperimenteel bevestig nie.

In hierdie ondersoek is 'n lugverkoelde elliptiese buis waarin teenvloei kondensasie van stoom plaasvind gebruik om die drukval en vloeding in die buis asook die warmteoordragsvermoë van die buis te bestudeer. Die aanwesigheid van 'n terugvloei gebied op die buis se verrigting is ook ondersoek. Die 7 m lange buis het 'n hoogte van 97 mm (hoof-as) en 'n breedte van 16 mm en is teen 'n hoek van 60° met die horisontaal gemonteer. Dit het 'n skerp (90°) inlaat. Die stoom temperature wissel tussen 45 °C en 65 °C.

Die drukval metings wat tydens hierdie ondersoek geneem is, het dit duidelik gemaak dat die drukval oor die buis hoofsaaklik afhanklik is van die damp Froude getal by die buis inlaat. Die drukval word ook akkuraat deur die Zapke-Kröger drukval model voorspel in die gebied $0.1 \leq Fr_{Hsv} \leq 0.4$. By 'n sekere stoom snelheid vind daar 'n skerp styging in die drukval in die buis plaas. Hierdie verskynsel staan bekend as vloeding. Daar is bevind dat die densimetriese damp Froude getal met die buishoogte as die karakteristieke afmeting vloeding domineer. The gemete vloedingsnelhede stem ook goed ooreen met die wat deur die Zapke vloedingskorrelasie voorspel word. Vloeding blyk ook 'n beperkende effek op die warmteoordragstempo van die elliptiese buis te hê wanneer al die stoom in 'n teenvloei wyse gekondenseer word. Ten slotte, as gevolg van die aanwesigheid van 'n stoom terugvloeigebied het nie-kondenseerbare gasse in die buis versamel wat tot die vorming van 'n dooie of koue sone gelei het. Dit het tot 'n vermindering in die buis se warmteoordragsvermoë gelei.

SYNOPSIS

Zapke and Kröger developed a model for the pressure drop across flattened tubes employed in reflux condensers. This model is based on adiabatic two-phase countercurrent experiments and incorporates the theory on fluid friction during condensation by Groenewald. Zapke also developed a correlation with which the flooding velocity during adiabatic countercurrent flow may be predicted. The applicability of both the pressure drop model and the flooding correlation to reflux condensation had prior to this investigation not been verified by experiment.

In this investigation the header-to-header pressure drop, the occurrence of flooding and the heat transfer performance of an inclined air-cooled elliptical tube in which reflux condensation of steam occurs were studied. The qualitative effect of the presence of a backflow region on the performance of the tube was also investigated. The 7 m long tube has a height of 97 mm (major axis) and a width of 16 mm (minor axis) and a sharp-edged (90°) inlet. The tube is inclined at 60° to the horizontal. Steam temperatures are in the range of 45 °C to 65 °C.

The pressure drop measurements obtained in this investigation showed that the header-to-header pressure drop in the tube is predominantly dependent upon the superficial vapor Froude number at the tube entrance. The pressure drop is also accurately predicted by the Zapke-Kröger pressure drop model in the range $0.1 \leq Fr_{Hsv} \leq 0.4$. At a certain steam flow rate a sudden sharp increase in the pressure drop occurs. This phenomenon is known as flooding. It was found that flooding during reflux condensation is governed by the superficial densimetric vapor Froude number with the duct height taken as the characteristic dimension. The measured vapor velocities at flooding are also in close agreement with those predicted by the Zapke flooding correlation. Flooding was found to have a limiting effect on the heat transfer rate of the elliptical tube in which all the steam condenses in the reflux mode. Finally, the formation of a steam backflow region in the tube resulted in the accumulation of non-condensable gases and the formation of a dead or cold zone. This led to a decrease in the heat transfer rate of the tube.

ACKNOWLEDGEMENTS

I would like to express my gratitude to my promoter, Prof. Detlev Kröger for his guidance and support during the course of my studies. His input on an academic as well as on a personal level was invaluable.

My thanks also to Kobus Zietsman for his continued and ever willing assistance during the building of the experimental apparatus and in the testing thereof. Many thanks for the advice and encouragement during the course of my thesis. I would also like to thank the various staff members in the mechanical engineering workshop for their assistance in the building of the experimental apparatus.

I would also like to express my appreciation to De Beers Consolidated Mines for postponing my employment obligation and allowing me to continue my studies in the pursuit of a Masters of Mechanical Engineering degree.

A very special word of thanks to my parents who have continually supported and encouraged me, especially during the difficult stages of my thesis. Thank you for your continued love, patience, encouragement and faith in me.

Finally to all my friends, especially those in 8 Villa Campanula and in 12 Pieke in Stellenbosch and those in Lime Acres, thank you for your patience and encouragement.

TABLE OF CONTENTS

		Page
	Declaration	ii
	Opsomming	iii
	Synopsis	iv
	Acknowledgements	v
	Nomenclature	x
1	**CHAPTER 1 INTRODUCTION**	1.1
2	**CHAPTER 2 PRESSURE DROP AND THE OCCURRENCE OF FLOODING INSIDE A DEPHLEGMATOR TUBE**	2.1
2.1	**The two-phase pressure change in a duct**	2.2
	2.1.1 The separated flow model and accompanying correlations	2.3
	2.1.2 The stratified flow model	2.6
	2.1.3 The effect of condensation on the frictional pressure gradient	2.11
2.2	**The contraction pressure loss at the dephlegmator tube entrance**	2.13
	2.2.1 The single-phase contraction losses	2.14
	2.2.2 Two-phase contraction losses	2.16
2.3	**Flooding in a dephlegmator tube**	2.18
2.4	**The Zapke-Kröger dephlegmator header-to-header pressure drop model**	2.22
3	**CHAPTER 3 PREDICTING THE HEAT TRANSFER RATE OF A DEPHLEGMATOR TUBE**	3.1
3.1	**An analytical method of predicting the heat transfer rate in an air-cooled dephlegmator tube**	3.1
3.2	**The effect of the accumulation of non-condensable gases**	3.5

4	**CHAPTER 4**	4.1
	THE EXPERIMENTAL APPARATUS	
4.1	**Design specifications and basic design of the apparatus**	4.1
4.2	**The steam generator**	4.2
4.3	**The radial steam inlet and inlet header**	4.4
4.4	**The finned tube**	4.6
4.5	**The steam outlet header**	4.7
4.6	**The wooden casing and support frame**	4.8
4.7	**The flow-measuring ducts and outlet manifold**	4.9
4.8	**The steam by-pass pipe**	4.10
4.9	**The aftercondenser**	4.11
4.10	**The vacuum pump**	4.11
4.11	**Measuring instrumentation**	4.12
	4.11.1 Temperature measurements	4.12
	4.11.2 Pressure measurements	4.12
	4.11.3 Volume flow rate measurements	4.13
4.12	**The data logging system**	4.14
4.13	**A description of the entire system**	4.14
4.14	**Experimental procedure**	4.18
5	**CHAPTER 5**	5.1
	EXPERIMENTAL RESULTS	
5.1	**The dephlegmator tube header-to-header pressure drop**	5.1
5.2	**Flooding in the dephlegmator tube**	5.6
5.3	**The heat transfer rate of the dephlegmator tube**	5.12
5.4	**The effect of a backflow region on the performance of the dephlegmator tube**	5.14
6	**CHAPTER 6**	6.1
	CONCLUSIONS AND RECOMMENDATIONS	
	REFERENCES	R.1

A	**APPENDIX A** **APPLICATION OF THE ZAPKE-KRöGER PRESSURE DROP MODEL TO TWO TUBES OF A DOUBLE ROW DEPHLEGMATOR**	A.1
B	**APPENDIX B** **HEAT TRANSFER, PRESSURE DROP AND FLOODING SAMPLE CALCULATION**	B.1
B.1	**Measured and processed heat transfer and pressure drop data**	B.1
B.2	**The predicted header-to-header pressure drop**	B.5
B.3	**Prediction of flooding**	B.8
B.4	**The predicted heat transfer rate**	B.9
C	**APPENDIX C** **CALIBRATION OF THE ANEMOMETERS USED TO MEASURE THE AIR FLOW**	C.1
C.1	**The calibration apparatus and procedure**	C.1
C.2	**Calibration sample calculation**	C.2
C.3	**The calibration curves of the anemometers**	C.6
D	**APPENDIX D** **PROPERTIES OF FLUIDS**	D.1
D.1	**The thermophysical properties of saturated water vapor from 273.16 K to 380 K.**	D.1
	D.1.1 Vapor pressure	D.1
	D.1.2 Dynamic viscosity	D.1
	D.1.3 Density	D.1
D.2	**The thermophysical properties of saturated water liquid from 273.16 K to 380 K.**	D.2
	D.2.1 Density	D.2
	D.2.2 Dynamic viscosity	D.2
	D.2.3 Surface tension	D.2
	D.2.4 Specific heat	D.3

D.2.5 Thermal conductivity D.3

D.2.6 Latent heat of vaporization D.3

D.3 The thermophysical properties of dry air from 220 K to 380 K at standard atmospheric pressure (101325 N/m^2). D.3

D.3.1 Density D.3

D.3.2 Specific heat D.4

D.3.3 Dynamic viscosity D.4

D.3.4 Thermal conductivity D.4

E APPENDIX E E.1

GRAPHICAL AND EXPERIMENTAL DATA

E.1 Tables of the data used to generate the graphs in Chapter 5 E.1

E.2 Tables of measured experimental data E.8

NOMENCLATURE

A	area	m^2
c_p	specific heat at constant pressure	J/kgK
c_v	specific heat at constant volume	J/kgK
C	heat capacity rate	W/K
C_n	nozzle discharge coefficient	
d	diameter	m
d_H	hydraulic diameter	m
e	heat exchanger effectiveness	
E	Voltage	V
f	friction factor	
F	force	N
g	gravitational acceleration	m/s^2
G	mass flux	kg/m^2s
h	convective heat transfer coefficient	W/m^2K
H	height	m
i_{fg}	latent heat	J/kg
k	thermal conductivity	W/mK
K	coefficient	
L	length	m
m	mass flow rate	kg/s
n	number	
NTU	number of transfer units	
Ny	dimensional characteristic heat transfer parameter	m^{-1}
p	pressure	Pa
P	pitch	m
P_e	perimeter	m
Q	heat transfer rate	W
r	radius	m
R	thermal resistance	m^2K/W
	gas constant	J/kgK
Ry	dimensional characteristic heat exchanger flow parameter	m^{-1}

T	temperature	°C, K
U	overall heat transfer coefficient	W/m^2K
v	velocity	m/s
v	specific volume	m^3/kg
V	volume flow rate	m^3/s
w	mass flow rate per unit length	kg/sm
x	vapor mass fraction (quality)	
Y	approach velocity factor	
z	coordinate	m

Greek symbols

α	void fraction	
β	friction enhancement factor	
Γ	film flow rate per unit width	kg/sm
δ	film thickness	m
ϕ_g	gas expansion factor	
φ	suction parameter (Eqns. 2.28, 2.29)	
θ	tube inclination angle	°
μ	dynamic viscosity	kg/ms
ρ	density	kg/m^3
σ	surface tension	N/m^2
	area ratio	
τ	shear stress	N/m^2
$\angle$	angle	°

Dimensionless Groups

Fr_{Hsn}	Superficial densimetric Froude number with the duct height used as the characteristic dimension	$\frac{\rho_n v_n^2}{(\rho_l - \rho_v)gH}$
Fr_{dsn}	Superficial densimetric Froude number with the hydraulic diameter used as the characteristic dimension	$\frac{\rho_n v_n^2}{(\rho_l - \rho_v)gd_h}$

Ku_n	Kutateladze number	$\frac{\rho_n^{0.5} v_n}{[(\rho_l - \rho_v)g\sigma]^{0.25}}$
Pr	Prandtl number	$\frac{\mu c_p}{k}$
Re	Reynolds number	$\frac{\rho v d_h}{\mu}$
v_{sn}^*	dimensionless superficial velocity	$\frac{\rho_n^{0.5} v_{sn}}{[(\rho_l - \rho_v)g d_h]^{0.5}}$
Zk	Zapke-Kröger number	$\frac{\sqrt{\rho_l d_h \sigma}}{\mu_l}$
ϕ_k^2	two-phase multiplier	$\left(\frac{dp_f}{dz}\right) \Big/ \left(\frac{dp}{dz}\right)_k$
ψ^2	Funnell gas only two-phase multiplier	$\left(\frac{dp}{dz}\right)_{TP} \Big/ \left(\frac{dp}{dz}\right)_{go}$

Subscripts

a	air
amb	ambient
anem	anemometer
c	condensate, condensation, contraction, cross-sectional
d	diameter
e	effective, expansion
f	friction, film
fl	flooding
fr	frontal
g	gravity
go	gas only
H	tube height
i	interfacial, in
in	inside
irrev	irreversible
l	liquid
lat	latitude

lo	liquid only
m	momentum, with mass transfer, mean
min	mimimum
n	normal, nozzle
o	out
r	row
rev	reversible
s	superficial, steam
SP	single-phase
t	tube
temp	temperature
tf	tube flange
tus	windtunnel cross-section
T	total
TP	two-phase
u	upstream
v	vapor
vo	vapor only
w	wall
y	coordinate
∞	free stream

Superscripts

+	dimensionless

CHAPTER 1

INTRODUCTION

In a power generating plant with a steam cycle, low pressure steam exiting the steam turbine needs to be condensed before it can be pumped back to the boiler. Forced draft air-cooled or direct dry-cooled condensers are used especially in arid regions for this purpose. The condensers consist of finned tube bundles arranged in an A-frame configuration above the fans. The inclination angle of the finned tubes, which generally have a round, elliptical or flat-profile cross-sectional geometry, is approximately 60° to the horizontal. In the finned tubes the steam and condensate flow cocurrently downward into the condensate return header.

A difference in the heat transfer rate between finned tubes of multiple-row or single row condensers may result in a steam backflow region in certain tubes [80BE1]. This can result in non-condensable gases being trapped in the bottom of the condenser, causing amongst others the thermal effectiveness of the condenser to decrease. To prevent the formation of a backflow region and the subsequent accumulation of non-condensable gases, a secondary condenser known as a dephlegmator is connected in series with the main condenser as shown in Figure 1.1. The dephlegmator ensures that there is a net outflow of steam from the bottom of the main condenser. This steam condenses in a reflux mode in the dephlegmator, the steam flow being countercurrent to the condensate flow. Non-condensable gases that may have leaked into the system are removed at the top of the dephlegmator by means of an ejector.

When designing a dephlegmator, it is important that one have a good understanding of the two-phase fluid flow modes and heat transfer characteristics in the dephlegmator. A substantial amount of literature is available regarding the two-phase pressure drop inside tubes, but most of it is not applicable to stratified flow that occurs during reflux condensation in inclined dephlegmator tubes. Zapke and Kröger [97ZA1] conducted adiabatic countercurrent experiments and incorporating the theory on fluid friction during condensation by Groenewald [93GR1] developed a model for the pressure drop

across flattened tubes employed in reflux condensers. The applicability of the model to vapor flow during reflux condensation has however not been verified by experiment.

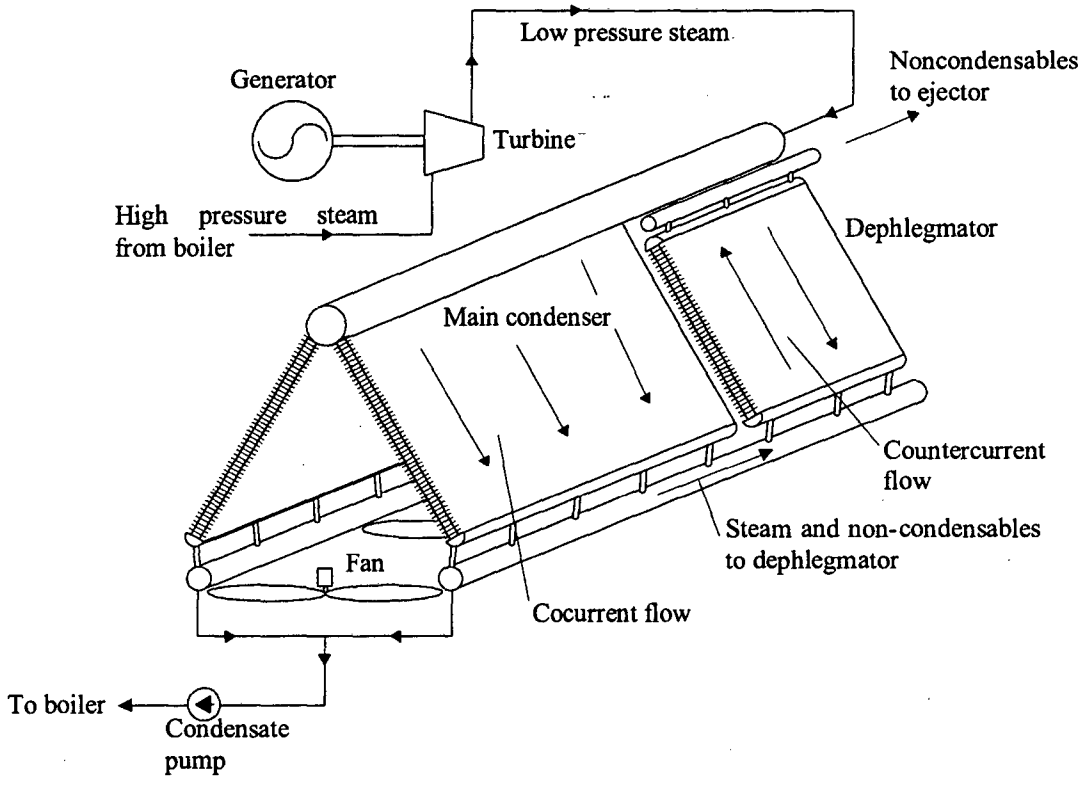

Figure 1.1: A schematic of the main condenser and dephlegmator of a forced draught air-cooled condenser used in direct dry-cooled power stations.

Since the dephlegmator operates in the reflux condensation mode, flooding is a potential problem. At a certain vapor inlet velocity, the condensate does not drain freely into the bottom header of the dephlegmator. The condensate starts to accumulate in the tubes, resulting in a large pressure drop across the dephlegmator headers and reduced thermal performance. Ultimately this has a detrimental effect on the efficiency of the entire power generating system. It is therefore important to know at which vapor velocity this sharp increase in pressure drop occurs so that this phenomenon may be avoided. Zapke [97ZA2] presented a correlation for adiabatic two-phase countercurrent flow in flattened tubes with which the flooding velocity may be predicted. It is unsure though, whether this correlation may be applied to reflux condensation.

In this investigation, experimental tests are performed using a commercially available elliptical finned tube inclined at 60° to the horizontal. Working with a steam temperature between 45 °C and 65 °C, the header-to-header pressure drop and the tube heat transfer rate are measured. The flooding vapor velocity was also determined for a number of steam temperatures. The results are compared to the predicted pressure drop and flooding velocity values calculated using the Zapke-Kröger pressure drop model and the Zapke flooding correlation. In a multi-tube row dephlegmator or in cases where there is as maldistribution of fluid flow, backflow of vapor in certain tubes may occur. Tests are also performed to qualitatively determine the effect of the formation of a steam backflow region on the heat transfer and pressure drop inside a dephlegmator tube. The findings of the investigation should serve to establish the validity of the above-mentioned pressure drop model and flooding correlation while also contributing to the understanding of the heat transfer and fluid flow mechanisms in a dephlegmator tube.

CHAPTER 2

PRESSURE DROP AND THE OCCURRENCE OF FLOODING INSIDE A DEPHLEGMATOR TUBE

The header-to-header two-phase pressure drop and the occurrence of flooding are important flow characteristics of a dephlegmator that can influence the heat transfer performance thereof. In order to improve on current dephlegmator design methods, a good understanding of the dephlegmator flow characteristics is necessary. In this chapter, analytical and empirical methods for predicting the header-to-header pressure drop and the occurrence of flooding in a single dephlegmator tube will be considered.

A schematic of a single air-cooled finned tube inclined at 60° to the horizontal is shown in Figure 2.1. Denoting a decrease in the static pressure in the positive z-direction as being positive, the header-to-header pressure drop in the tube can symbolically be expressed as

$$\Delta p_{14} = \Delta p_{12} + \Delta p_{23} + \Delta p_{34} \tag{2.1}$$

The inlet static pressure change, Δp_{12}, is a result of the contraction in the flow area at the tube entrance, while the exit static pressure change, Δp_{34} is caused by the expansion of the flow area at the tube exit. The static pressure change in the tube, Δp_{23}, is actually a combination of three individual pressure change components [75TO1], namely a frictional component, a gravitational component and a momentum change component. This relationship can be expressed as follows:

$$\Delta p_{23} = \Delta p_{f23} + \Delta p_{g23} + \Delta p_{m23} \tag{2.2}$$

In order to accurately calculate the tube header-to-header pressure change, each term on the right hand side of equation (2.1) needs to be evaluated. This is potentially a

complex problem since these terms need to be calculated for two-phase flow. In the following sections each of the pressure change components will be discussed.

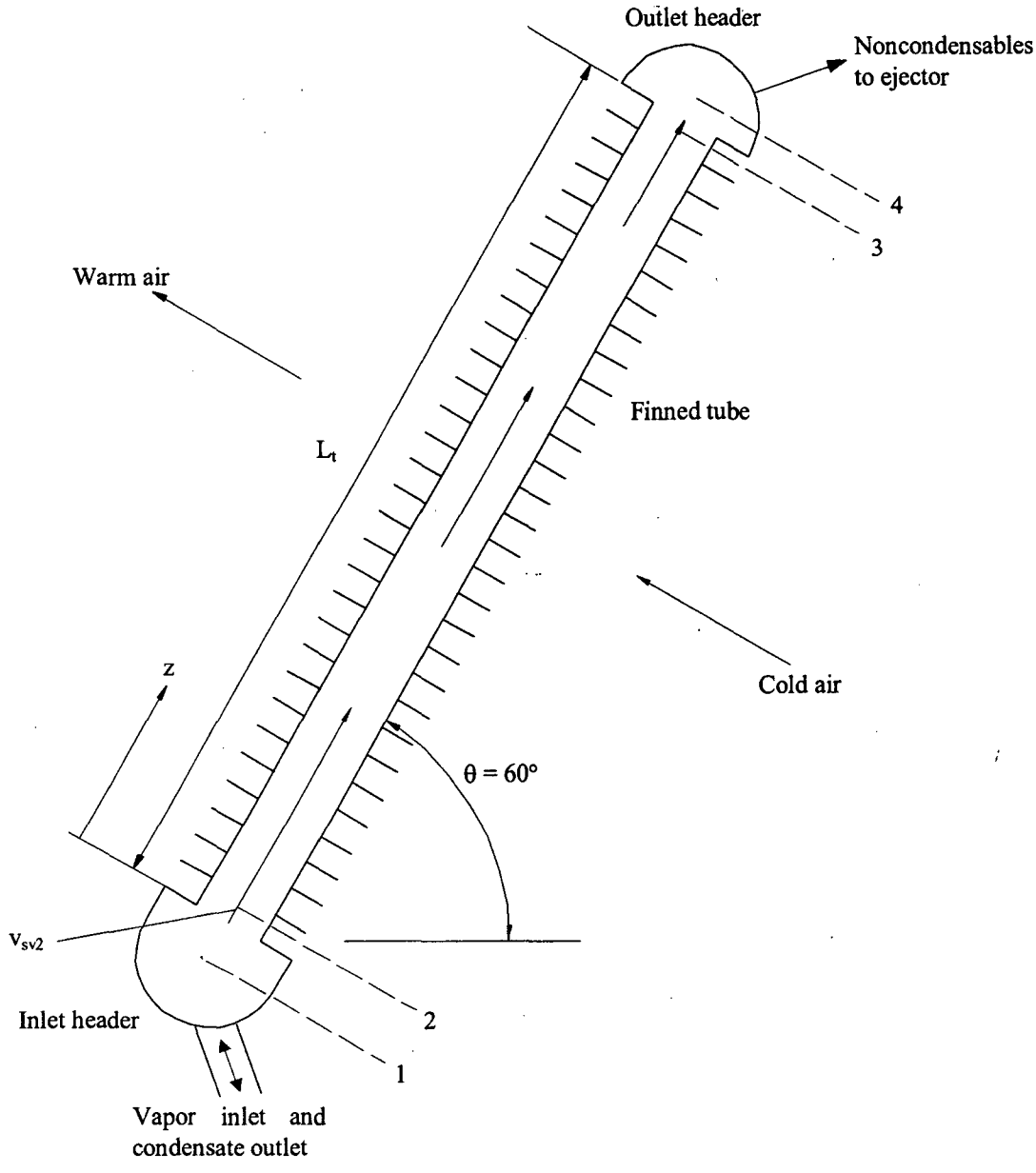

Figure 2.1: A schematic of an air-cooled dephlegmator tube.

2.1. The two-phase pressure change in a duct

Numerous models and correlations have been developed with which the two-phase pressure drop in a duct can be calculated. Since certain models are only applicable to the specific flow regime for which they were developed, it is important to ascertain the

type of two-phase flow regime in the duct under investigation. Under normal design operating conditions stratified countercurrent flow is the dominant flow regime in a dephlegmator tube and therefore models such as the homogenous and annular flow models cannot be used to calculate pressure drops therein. The models and correlations applicable to the flow mode in a dephlegmator tube will now be discussed.

2.1.1 The separated flow model and accompanying correlations

The separated flow model represents the general case of two-phase flow [92CA1]. It is developed using the basic conservation equations for two-phase flow with the assumptions that the two phases are separate and the phase velocities are constant but not necessarily the same. On this basis, it is applicable to stratified flow, but it is, however, also used to determine the pressure drop in other two-phase flow regimes.

Figure 2.2 is a diagram of a simplified one-dimensional two-phase gas-liquid flow system, with the z-axis being in the axial direction of the duct. Assuming there is no mass transfer through the walls of the tube, the conservation of mass expressed in differential form requires that

$$dm_v = -dm_l \tag{2.3}$$

or

$$\frac{d}{dz}(\rho_v GAx) + \frac{d}{dz}(\rho_l GA(1-x)) = 0 \tag{2.4}$$

where G is the total mass flux.

The momentum equation is obtained from a force–momentum balance performed in the axial direction on the fluid element in Figure 2.2. Performing such a balance on the vapor phase alone yields

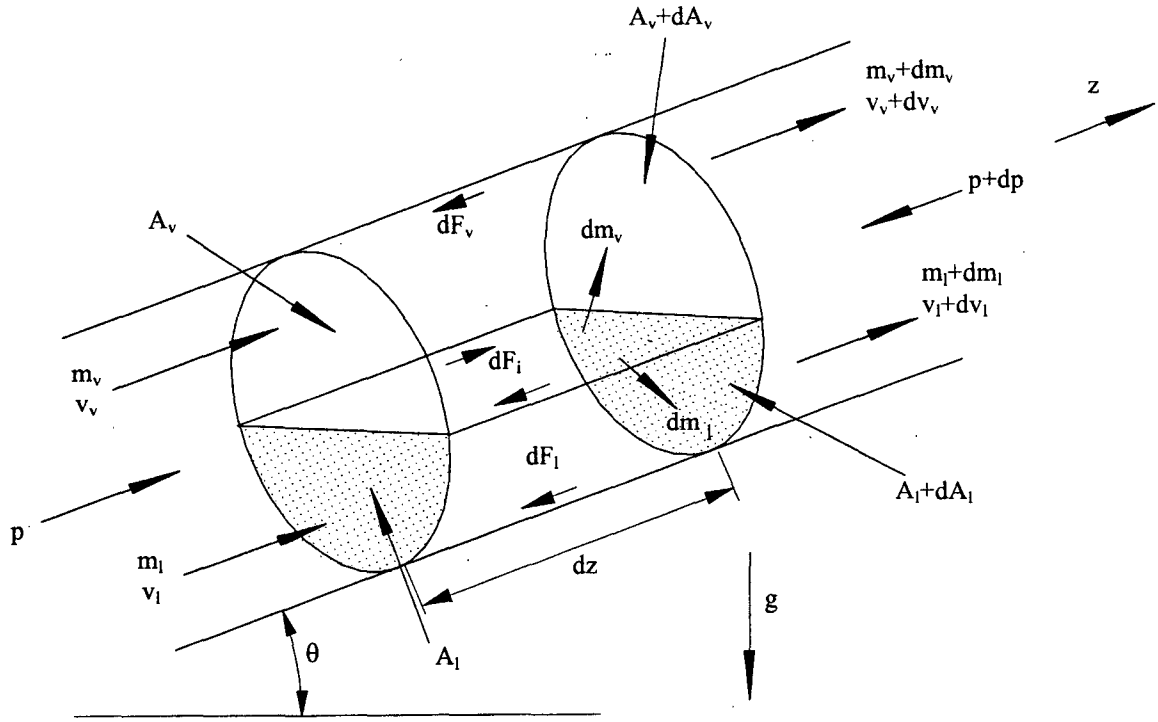

Figure 2.2: Idealized model of momentum transport during vapor-liquid two-phase flow in an inclined tube.

$$\begin{aligned} &pA_v - (p+dp)(A_v + dA_v) - dF_v - dF_{i,v} - A_v dz\,\rho_v g \sin\theta \\ &\quad = (m_v + dm_v)(v_v + dv_v) - m_v v_v - dm_v v_v \end{aligned} \tag{2.5}$$

The terms dF_v and $dF_{i,v}$ represent the frictional effect of the vapor on the channel wall, and the shear force at the liquid-vapor interface, respectively. In the same way, a momentum balance for the liquid phase can be written as

$$\begin{aligned} &pA_l - (p+dp)(A_l + dA_l) - dF_l + dF_{i,l} - A_l dz\,\rho_l g \sin\theta \\ &\quad = (m_l + dm_l)(v_l + dv_l) - m_l v_l - dm_l v_l \end{aligned} \tag{2.6}$$

The shear forces at the liquid-vapor interface must balance so that

$$dF_{i,l} = -dF_{i,v} \tag{2.7}$$

Therefore, by adding equations (2.5) and (2.6) and using equation (2.3), the following relation may be obtained for the overall momentum balance:

$$-Adp - pdA - dF_l - dF_v - (A_l\rho_l + A_v\rho_v)g\,dz\sin\theta = d(m_v v_v + m_l v_l) \tag{2.8}$$

Defining a frictional two-phase pressure gradient to account for the frictional forces experienced by the two phases on the wall such that

$$-\left(\frac{dp_f}{dz}\right)_{TP} A\,dz = dF_l + dF_v \tag{2.9}$$

and making use of the expressions for void fraction, liquid velocity and vapor velocity in two-phase flow, the momentum balance for separated two-phase flow in a duct can be expressed as

$$-\left(\frac{dp}{dz}\right) = -\left(\frac{dp_f}{dz}\right)_{TP} + [(1-\alpha)\rho_l + \alpha\rho_v] \times g\sin\theta + G^2\frac{d}{dz}\left[\frac{x^2}{\rho_v\alpha} + \frac{(1-x)^2}{\rho_l(1-\alpha)}\right] \tag{2.10}$$

if it is assumed that the cross-sectional area of the duct does not change. The first term on the right hand side of equation (2.10) represents the static pressure loss due to friction, the second term the pressure difference due to a static head difference and the third term the pressure change due to a change in momentum. The two-phase frictional pressure gradient is often expressed in terms of a so-called two-phase multiplier and a single-phase pressure gradient:

$$\left(\frac{dp_f}{dz}\right)_{TP} = \phi_k^2\left(\frac{dp_f}{dz}\right)_k \qquad k = l, lo, v \text{ or } vo \tag{2.11}$$

where the subscripts 'l' and 'v' denotes the frictional pressure gradient that would result if liquid or the vapor flowed alone through the tube at a mass flow rate of G(1-x)A and GAx respectively . The subscripts 'lo' and 'vo' are used when the entire flow is considered solely a liquid or a vapor flow, i.e. liquid or vapor flow at a mass flow rate of GA. Using the liquid only two-phase multiplier, equation (2.10) can then be written as

$$-\left(\frac{dp}{dz}\right)=-\phi_{lo}^{2}\left(\frac{dp_f}{dz}\right)_{lo}+[(1-\alpha)\rho_l+\alpha\rho_v]\times g\sin\theta+G^2\frac{d}{dz}\left[\frac{x^2}{\rho_v\alpha}+\frac{(1-x)^2}{\rho_l(1-\alpha)}\right] \quad (2.12)$$

The liquid only frictional pressure gradient may be evaluated in terms of the liquid only friction factor:

$$-\left(\frac{dp_f}{dz}\right)_{lo}=\frac{2f_{lo}G^2}{\rho_l d_h}, \quad (2.13)$$

where the liquid only friction factor is calculated using, for example, the Blasius equation. In order to calculate the pressure drop in a duct, equation (2.12) needs to be integrated over the duct length. This can only be done if expressions for the void fraction, quality and the two-phase multiplier are known. A number of correlations have been developed with which the void fraction and two-phase multiplier may be calculated and are well documented in literature [72CO1, 82HE1, 87WH1, 92CA1]. The Lockhart-Martinelli correlation is perhaps the most well known two-phase multiplier correlation and according to Hewitt [82HE1], despite its deficiencies, it is still probably the most widely used two-phase flow correlation. Other correlations for the two-phase multiplier that are used fairly extensively today are those presented by Friedel and Baroczy respectively [92CA1]. Ide and Matsumura [90ID1] found that the above-mentioned correlations, which were developed from experimental data obtained using tubes, do not always yield accurate results for the pressure drop in non-circular ducts. They therefore developed a correlation for the liquid two-phase multiplier to be used for flows with a small liquid superficial velocity in rectangular ducts. To determine the void fraction, Whalley [87WH1] recommends the CISE-correlation for general use, while Carey [92CA1] suggests the correlation proposed by Lockhart and Martinelli. Using these correlations in conjunction with equation (2.12), the pressure change in the duct may be determined by numerical integration.

2.1.2 The stratified flow model

The stratified flow model, like the separated flow model, is developed using the basic two-phase flow conservation equations. However, the wall and interfacial friction

forces experienced by the vapor and liquid as depicted in Figure 2.2 are expressed in terms of shear stresses as follows:

$$dF_v = \tau_{w,v} P_{c,v} dz \tag{2.14}$$

$$dF_l = \tau_{w,l} P_{c,l} dz \tag{2.15}$$

$$dF_{i,v} = -dF_{i,l} = \tau_i P_{c,i} dz \tag{2.16}$$

where $P_{e,v}$ and $P_{e,l}$ are the tube perimeters in contact with the vapor and liquid phases respectively and $P_{e,i}$ is the perimeter at the liquid-vapor interface. After substituting equations (2.14) to (2.16) into equations (2.5) and (2.6) and rearranging, the momentum equations for the vapor and liquid phases in stratified flow are

$$-\frac{dp}{dz} - \frac{\tau_{w,v} P_{c,v}}{\alpha A} - \frac{\tau_i P_{c,i}}{\alpha A} - \rho_v g \sin\theta = \frac{d}{dz}\left[\frac{G^2 x^2}{\rho_v \alpha^2}\right] \tag{2.17}$$

$$-\frac{dp}{dz} - \frac{\tau_{w,l} P_{c,l}}{(1-\alpha)A} + \frac{\tau_i P_{c,i}}{(1-\alpha)A} - \rho_l g \sin\theta = \frac{d}{dz}\left[\frac{G^2 (1-x)^2}{\rho_l (1-\alpha)^2}\right] \tag{2.18}$$

Agrawal et al. [73AG1], Taitel and Dukler [76TA1] and Cherimisinoff and Davis [79CH1] have all presented methods to determine the pressure drop for two-phase stratified flow in horizontal pipes with no mass transfer between the phases. No mass transfer implies that the terms on the right hand side of equations (2.17) and (2.18) are equal to zero. Their methods are similar in the sense that they all make use of iterative techniques to solve for the pressure drop using equations (2.17) and (2.18). The shear stresses in the equations above are expressed in terms of the appropriate friction factors:

$$\tau_{w,v} = f_v \frac{\rho_v v_v^2}{2}, \qquad \tau_{w,l} = f_l \frac{\rho_l v_l^2}{2}, \qquad \tau_i = f_i \frac{\rho_v v_v^2}{2} \tag{2.19}$$

The vapor and liquid friction factors are calculated as follows for turbulent flow:

$$f_k = 0.046\left(\frac{\rho_k d_{h,k} v_k}{\mu_k}\right)^{-0.2} \qquad k = v, l \tag{2.20}$$

The hydraulic diameters are evaluated in the manner suggested by Agrawal et al.:

$$d_{h,v} = \frac{4A_v}{P_{e,v} + P_{e,i}} \qquad d_{h,l} = \frac{4A_l}{P_{e,l}} \tag{2.21}$$

For the interfacial friction factor, Agrawal et al. use the friction factor as proposed by Ellis and Gay (1959):

$$f_i = 2.587\,\mathrm{Re}_v^{-0.57} \tag{2.22}$$

For small amplitude waves, Cheremisinoff and Davis [79CH1] used $f_i = 0.00355$ and for roll waves they used the correlation of Cohen and Hanratty (1968):

$$f_i = 0.0080 + 2.00 \times 10^{-5}\,\mathrm{Re}_l \qquad \text{for} \qquad 100 \le \mathrm{Re}_l \le 1700 \tag{2.23}$$

and although the liquid Reynolds number range is rather limited for this correlation, they still obtained good results for liquid Reynolds numbers outside this domain.

In an inclined dephlegmator tube, the liquid flow area usually occupies only a very small portion of the tube cross-sectional area and only the pressure drop as a result of the flowing vapor is generally considered. Zapke and Kröger [97ZA1] therefore neglected the liquid momentum equation (2.18). Referring to the vapor momentum equation, they combined the second and third term on the left-hand side of equation (2.17) and expressed them in terms of an effective frictional pressure gradient. The pressure gradient in turn is a function of an effective two-phase Darcy friction factor based on the superficial velocity of the vapor. Zapke [97ZA2] conducted experiments to determine the pressure gradient for adiabatic two-phase countercurrent flow in an inclined flat-profile tube made of perspex. The tube had a width and height of 9.95 mm and 100 mm respectively. Various gases and liquids were used as the working fluids. For a complete description of the apparatus consult [96ZA3] or [97ZA2]. Using the measured pressure gradient Zapke calculated an adiabatic two-phase friction factor.

This was correlated in terms of the superficial vapor Reynolds number in the form of a Blasius-type equation as follows:

$$f_{sv,TP} = K_f \, Re_{sv}^{n_f} = \left(\frac{dp_f}{dz}\right)_{TP} d_h / \left(0.5 \rho_v v_{sv}^2\right) \tag{2.24}$$

where $K_f = 0.2259$ and $n_f = -0.2088$ for the particular test tube. The results of these experiments are also given graphically in Figure 2.3.

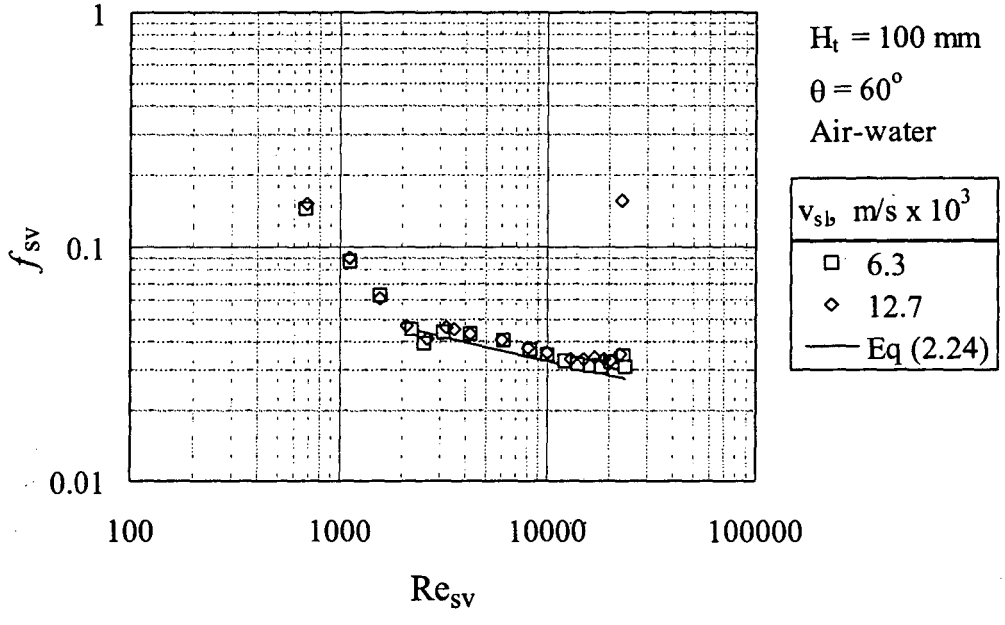

Figure 2.3: The measured adiabatic two-phase countercurrent flow vapor friction factor plotted against the vapor Reynolds number as obtained by Zapke and Kröger [96ZA3].

Note that in this approach, turbulent flow is assumed for the entire tube since in a dephlegmator tube the transition from turbulent to laminar flow occurs close to the top of the tube. The pressure drop in the laminar region is very small compared to the total pressure drop in the tube and can be approximated by the relations for turbulent flow without any loss in accuracy [96ZA3]. It is therefore acceptable to assume only turbulent flow and thus only make use of Equation (2.24) when calculating the friction factor in a dephlegmator tube.

Funnell [91FU1] made use of a method to determine the two-phase pressure gradient for stratified flow in a flattened tube that was similar to the approach used by Bergelin to

measure the two-phase friction factor for annular flow in vertical tubes. According to Blangetti et al. [82BL1] the results of Bergelin (1949) are such that the measured two-phase friction factor can be split up into two terms as follows:

$$f_{TP} = f_{SP} + \Delta f_{TP} \tag{2.25}$$

The first term accounts for the single-phase friction inside the tube while the second term takes into account the work for the deformation of the liquid film surface at the liquid-vapor interface. Instead of considering the interfacial friction factor, Funnell worked with the measured adiabatic two-phase pressure gradient and a gas-only pressure gradient. He performed adiabatic air-water countercurrent pressure drop tests in a flat-profile perspex tube inclined at 60° to the horizontal. The width and height of this tube were 16.6 mm and 176.3 mm respectively. During the tests the combined frictional and gravitational pressure gradient was measured.

Funnell correlated the test data for adiabatic conditions in terms of a non-dimensional pressure gradient difference defined as follows:

$$\psi^2 - 1 = \frac{\left(\frac{\Delta p}{\Delta z}\right)_{TP} - \left(\frac{\Delta p}{\Delta z}\right)_{go}}{\left(\frac{\Delta p}{\Delta z}\right)_{go}} = \frac{\left(\frac{\Delta p}{\Delta z}\right)_{TP}}{\left(\frac{\Delta p}{\Delta z}\right)_{go}} - 1 \tag{2.26}$$

It is important to note that ψ^2 is not the same as the general two-phase multiplier ϕ^2, which is defined in terms of the frictional pressure gradients, whereas ψ^2 is defined in terms of the total pressure gradient. Groenewald [93GR1] presented the results of these tests graphically for a tube inclination angle of 60°. These graphical results are given in Figure 2.4. A very complex correlation for this data consisting of at least 8 different functions of the superficial gas Froude number was also developed. [93GR1] describes this correlation in detail.

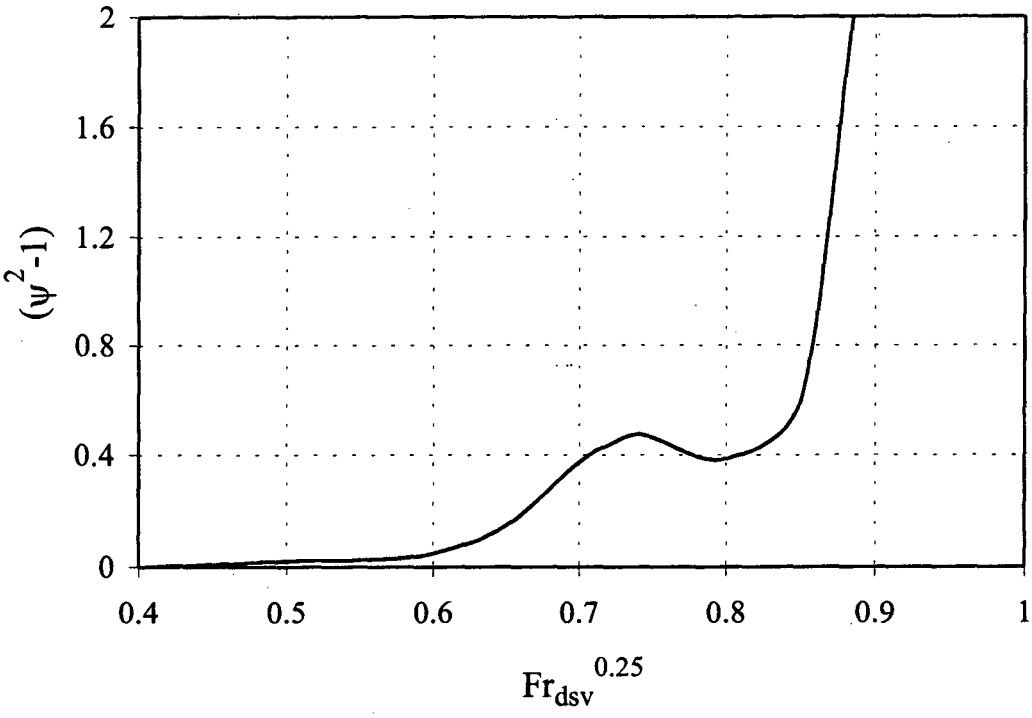

Figure 2.4: A graphic representation of Funnell's [91FU1] correlation for the adiabatic two-phase countercurrent pressure gradient in a flat-profile tube inclined at 60°.

2.1.3 The effect of condensation on the frictional pressure gradient

Most of the models and correlations described above have been for adiabatic two-phase flow. However, during a condensation process in a tube, the movement of mass across the vapor boundary layer causes a flattening of the vapor velocity profile. As a result, the velocity gradient at the liquid-vapor interface increases, causing a higher interfacial shear stress. An adiabatic friction factor or pressure gradient can therefore not be directly applied to two-phase flow with condensation. Groenewald [93GR1] describes various methods that are used to take the effect of condensation into account. One such method to account for the effect of mass transfer is to correct the adiabatic shear stress, τ_i, with a condensation enhancement factor, β to find the effective shear stress with mass transfer:

$$\tau_{im} = \beta\tau_i \tag{2.27}$$

where 'm' denotes 'with mass transfer'.

Blangetti et al. [82BL1] derived an expression for β for cocurrent flow by integrating across the laminar boundary layer of the vapor adjacent to the liquid condensate film. Assuming that the boundary layer thickness with or without mass transfer remains the same, Blangetti et al. showed that

$$\beta = \frac{\varphi}{\exp(\varphi) - 1} \tag{2.28}$$

where

$$\varphi = \frac{v_{yw}/v_{\infty}}{f/2} = \frac{m_c}{P_{ci} L_t \rho_v v_{\infty} f/2} \tag{2.29}$$

[82BL1] states that this enhancement factor must only be applied to the single-phase portion of the two-phase friction factor of equation (2.25). The interfacial friction factor taking condensation into account is then

$$f_{TP} = \beta f_{SP} + \Delta f_{TP} \tag{2.30}$$

Groenewald [93GR1] also derived an expression for β for turbulent flow between two parallel plates. This was obtained by applying the differential momentum equation to the flow and adding uniform suction to account for condensation. The equation was simplified and then integrated numerically. A correlation presented by [93GR1] that approximates the numerical results is given as

$$\beta = \frac{f_m}{f} = a_n + \frac{b_n}{Re_{d_h}} \tag{2.31}$$

where the constants a_n and b_n are functions of the suction Reynolds number, Re_{vn}, and

$$a_n = 1.041 \times 10^{-3} Re_{vn} - 2.011 \times 10^{-7} Re_{vn}^3 + 1.0649 \tag{2.32}$$

$$b_n = 59.3153 Re_{vn} + 1.5995 \times 10^{-2} Re_{vn}^3 + 290.1479 \tag{2.33}$$

for $0 \leq Re_{vn} \leq 40$. The friction factor with zero mass transfer, f to which the friction factor with mass transfer, f_m, is compared in equation (2.31), is obtained from the Blasius equation for smooth walls:

$$f = 0.0791 / Re_{d_h}^{0.25} \tag{2.34}$$

using the hydraulic diameter for flow between parallel plates. Note that the suction Reynolds number, Re_{vn} can be expressed in terms of the total condensate mass flow rate flowing out of the bottom of a dephlegmator tube:

$$Re_{vn} = m_c d_h / (\mu_v L_t P_{et}) \tag{2.35}$$

Groenewald [93GR1], like Blangetti et al. [82BL1], also only applied the enhancement factor to the single-phase friction factor. Taking the wall suction effect due to condensation into account Groenewald modified equation (2.26) as follows:

$$\begin{aligned}\left(\frac{dp}{dz}\right)_{TP} &= \left(\frac{dp_f}{dz}\right)_{TP} + \left(\frac{dp_g}{dz}\right)_{TP} \\ &= (\psi^2 - 1)\left(\frac{dp}{dz}\right)_{go} + \beta\left(\frac{dp_f}{dz}\right)_{go} + \left(\frac{dp_g}{dz}\right)_{go} \\ &= [(\psi^2 - 1) + \beta]\left(\frac{dp_f}{dz}\right)_{go} + [(\psi^2 - 1) + 1]\left(\frac{dp_g}{dz}\right)_{go}\end{aligned} \tag{2.36}$$

Zapke and Kröger [97ZA1] applied Groenewald's condensation enhancement factor to the total adiabatic two-phase friction factor. This was done since the two-phase vapor frictional pressure drop does not deviate significantly from the corresponding single-phase values.

2.2. The contraction pressure loss at the dephlegmator tube entrance

The other major contribution to the header-to-header pressure drop is the pressure change over the tube inlet, Δp_{12}, which is caused by a sudden contraction in flow area at the tube entrance. In a dephlegmator, the inlet pressure drop has to be evaluated for

two-phase flow, but before this pressure loss is considered, it is useful to first consider the contraction pressure change for single-phase flow.

2.2.1 The single-phase contraction losses

In Figure 2.5 a fluid flowing in a duct that has a sudden contraction is depicted. Downstream of the contraction, a vena contracta, which is narrower than the diameter of the smaller pipe, is formed. From the vena contracta, the flow expands again to fill the pipe. Eddies form between the vena contracta and the point at which the streamlines reattach themselves to the pipe wall causing the dissipation of mechanical energy as heat. The loss of mechanical energy is evident as an irreversible pressure loss over the contraction. Symbolically the irreversible pressure loss can be expressed as follows:

$$\Delta p_{irrev} = p_{T1} - p_{T2} = \left(p_1 + \rho v_1^2/2\right) - \left(p_2 + \rho v_2^2/2\right) = K_c\, \rho v_2^2/2 \tag{2.37}$$

where p_{T1} and p_{T2} are the total pressures at sections 1 and 2 and K_c is the contraction loss coefficient based on the velocity in the duct after the contraction, i.e. v_2. It is usually assumed that the contraction of the fluid is reversible, while the irreversible pressure losses occur during the flow expansion from the vena contracta to the wall of the smaller pipe [50KA1]. The change in static pressure over the flow contraction can therefore be expressed as

$$p_1 - p_2 = \Delta p_{rev} + \Delta p_{irrev} = \left[\left(1 - \sigma_{21}^2\right) + K_c\right]\rho v_2^2/2 \tag{2.38}$$

where $\sigma_{21} = A_2/A_1$ is the area contraction ratio.

According to Kays [50KA1], if a uniform velocity profile and fully turbulent incompressible flow is assumed, then the contraction loss coefficient can be expressed as

$$K_c = \left(1 - 1/\sigma_c\right)^2 \tag{2.39}$$

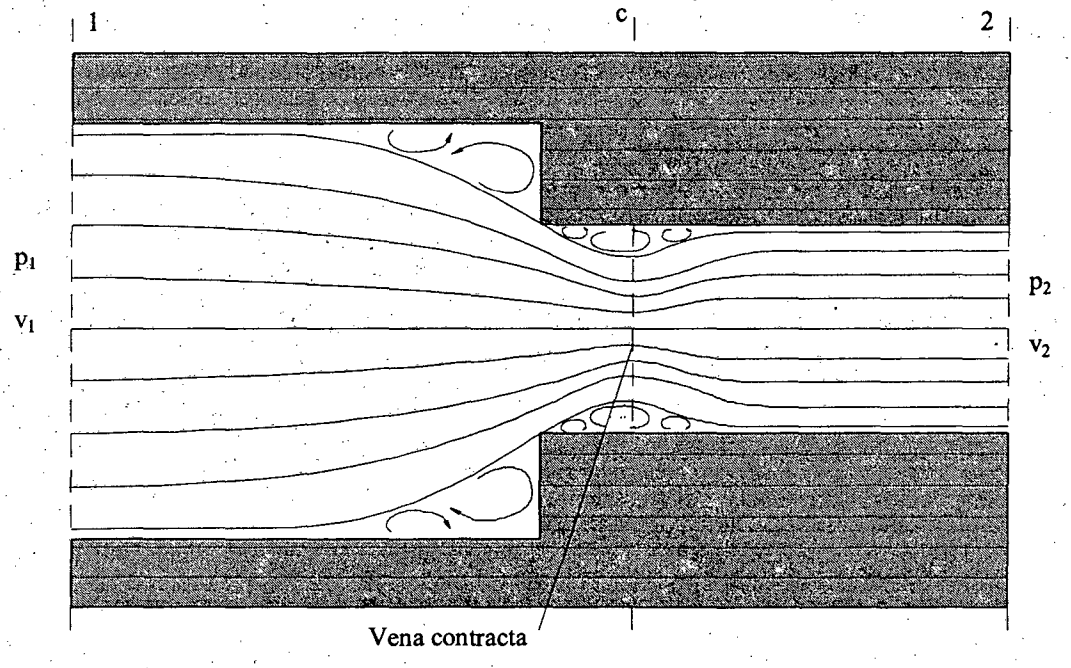

Figure 2.5: The streamline patterns in a single-phase fluid showing the vena contracta and eddies at a sudden contraction in the flow cross-sectional area of a duct.

where $\sigma_c = A_c/A_2$ is the jet contraction ratio and A_c is the vena contracta cross-sectional area. The value of σ_c is usually determined experimentally. According to Kröger [89KR1], Weisbach (1966) determined σ_c as a function of the area contraction ratio, σ_{21}, for round tubes and parallel plates and presented his results graphically. The following polynomials are given by Kröger to approximate his data:

$$\sigma_c = 0.61375 + 0.13318\sigma_{21} - 0.26095\sigma_{21}^2 + 0.51146\sigma_{21}^3 \tag{2.40}$$

for round tubes, and

$$\sigma_c = 0.6144517 + 0.04566493\sigma_{21} - 0.336651\sigma_{21}^2 + 0.4082743\sigma_{21}^3 + 2.672041\sigma_{21}^4 - 5.963169\sigma_{21}^5 + 3.558944\sigma_{21}^6 \tag{2.41}$$

for parallel plates. Other analytical as well as semi-emperical contraction loss coefficients for single-phase flow are also used, but will not be considered here. For a summary thereof, the reader may consult Zipfel [96ZI1].

2.2.2 Two-phase contraction losses

The two-phase pressure loss over a sudden contraction tends to be higher than for single-phase flow due to the interaction between the liquid and vapor phases. In the case of countercurrent flow, this effect is further enhanced since the downward flowing liquid disturbs the upward flowing vapor, and the vapor causes wave formation on the surface of the liquid. This is especially evident during reflux condensation where both the vapor and liquid velocities are at a maximum at the tube entrance, the tube entrance acting as a sudden contraction for the vapor. It is therefore not possible to directly make use of a single-phase inlet pressure loss coefficient to determine the pressure drop over a sudden contraction for two-phase flow. Unfortunately, the literature applicable to two-phase flow contraction losses is fairly limited, and furthermore, most of the existing literature mainly concerns cocurrent flow with low void fractions [89TA1, 97SC1].

Similar to the pressure drop in a dephlegmator tube, the inlet pressure drop can be calculated by considering only the vapor flow. Funnell [91FU1], Groenewald [93GR1] and Zapke and Kröger [96ZA3] determined the two-phase inlet pressure drop for a single dephlegmator tube using this method. Funnell found that the inlet pressure drop was not only a function of the inlet gas Reynolds number, but also dependent to a large extent on the inlet vapor kinetic energy. A portion of the kinetic energy is converted to mechanical work to initiate the formation of waves on the liquid surface at the tube entrance [93GR1]. The vapor kinetic energy is expressed in terms of the densimetric vapor Froude number based on the superficial velocity of the vapor as follows:

$$Fr_{Hsv} = \frac{\rho_v v_{sv}^2}{(\rho_l - \rho_v)gH} \tag{2.42}$$

where H is the height of the tube.

To show the influence of the vapor Froude number on the contraction losses, the Reynolds number effects and the dependence on a specific inlet geometry need to be excluded. Therefore, the single-phase contraction loss coefficient, $K_{c,SP}$, was subtracted from the measured two-phase contraction loss coefficient, $K_{c,TP}$. The resulting value, $\Delta K_{c,TP}$ represents the influence of the vapor Froude number on the inlet contraction loss.

Groenewald [93GR1] presented $\Delta K_{c,TP}$ graphically as a function of the fourth root of the vapor Froude number. The inlet contraction pressure loss can then be calculated using equation (2.38) with

$$K_c = K_{c,TP} = K_{c,SP} + \Delta K_{c,TP} \tag{2.43}$$

In the case of a dephlegmator, Zapke and Kröger [97ZA1] assumed that the void fraction inside the inlet header is close to unity. An expression for the two-phase pressure drop at the tube inlet is obtained that is similar to equation (2.38) for single-phase flow:

$$p_1 - p_2 = \frac{1}{2}\rho_v v_{sv2}^2 \left[\frac{1}{\alpha_2^2} - \sigma_{21}^2 + K_{c,TP} \right] \tag{2.44}$$

Note that the contraction loss coefficient is based on the vapor superficial velocity at position 2 of Figure 2.1. Instead of having to determine values for $1/\alpha_2^2$ and $K_{c,TP}$, Zapke and Kröger [97ZA1] combined these two terms in a single two-phase loss coefficient, K_{TP}. This could be done since the actual separate values of the above mentioned terms are not necessary to calculate the inlet pressure loss. Zapke and Kröger [96ZA3] conducted experiments with air and water using the experimental rig mentioned in a previous section and measured the two-phase contraction loss coefficient at the tube entrance. They correlated the experimental data in terms of the superficial vapor Froude number as follows:

$$K_{TP} = a_c \exp(b_c \, Fr_{Hsv}) \tag{2.45}$$

where a_c = 1.6502 and b_c = 1.0166 for their particular experimental rig. The results from which this correlation has been obtained are given graphically inFigure 2.6.

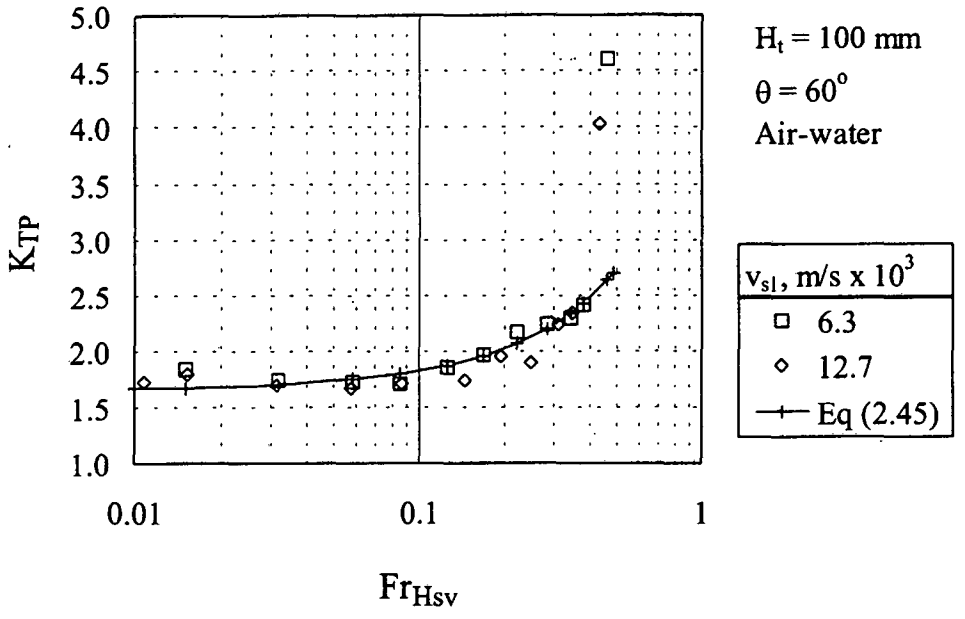

Figure 2.6: The experimental results of [96ZA3] of the combined two-phase inlet loss coefficient plotted against the superficial densimetric vapor Froude number.

2.3. Flooding in a dephlegmator tube

As was mentioned in the beginning of this chapter, flooding is an important flow characteristic that has an influence on the heat transfer performance of a dephlegmator. Flooding can occur in a duct operating in the reflux condensation mode, when the flow direction of the downward flowing liquid is reversed by the upward flowing vapor. The flow becomes unstable and the liquid tends to accumulate in the duct, which is accompanied by a sharp increase in the header-to-header pressure drop of the duct. The liquid build-up tends to decrease the thermal efficiency of the dephlegmator. It is therefore important to know at what vapor velocity flooding will occur in a dephlegmator tube.

A vast amount of literature concerning flooding exists, but the majority thereof pertains to adiabatic two-phase countercurrent flow using a variety of gases and liquids. A considerable amount of work has, however, also been done on flooding during reflux condensation by various researchers including Russell [80RU1], Banerjee et al. [83BA1], Girard and Chang [92GI1], Obinelo et al. [94OB1] and Reuter and Kröger [96RE1]. The available flooding literature, pertaining to both adiabatic two-phase flow

and reflux condensation, has been well surveyed by amongst others, Bankoff and Lee [86BA1], Bellstedt [91BE1] and Zapke [94ZA1, 97ZA2]. From the existing literature it is clear that the term 'flooding' has been used to describe various aspects of the above-mentioned liquid accumulation and accompanying sharp increase in pressure drop. Definitions of flooding velocity include:

a) The vapor flow rate at which liquid begins to be carried upwards above the liquid inlet (adiabatic flow) [96ZA1, 91GO1];
b) The vapor flow rate at which liquid is ejected from the top of the tube [91BE1, 89FU1];
c) The vapor flow rate at which the flow pattern in the tube becomes chaotic [80CH1];
d) The vapor flow rate at which a sharp increase in pressure drop in the tube takes place [63EN1, 69DI1, 96RE1];
e) The vapor flow rate at which a water column starts to build up in the tube [92GI1, 83BA1].

Differences in the definitions used for flooding and the large variation in the types of experimental rigs and procedures used to investigate flooding have resulted in considerable scatter in the available flooding data. Bellstedt [91BE1] demonstrated this scatter by plotting 2132 flooding data points obtained from the literature. Numerous models and flooding correlations exist which have been developed in an effort to correlate the flooding data. However, most of these tend only to correlate accurately the data from which they were derived and not data obtained by other researchers. A few of these correlations will now be considered.

One of the most frequently used correlations [86BA1] to predict when flooding occurs was derived by Wallis. The correlation took the following form:

$$v_{sv}^{*1/2} + m\, v_{sl}^{*1/2} = C \qquad (2.46)$$

where v_{sv}^{*} and v_{sl}^{*} are the dimensionless superficial vapor and liquid velocities respectively and are defined as

$$v_{sn}^{*} = \left[\frac{\rho_n v_{sn}^2}{(\rho_l - \rho_v)gd}\right]^{0.5} \qquad n = l, v \tag{2.47}$$

and $0.8 \leq m \leq 1.0$ and $0.7 \leq C \leq 1.0$, the exact values depending primarily on the tube end conditions. A correlation, similar in form to that of equation (2.46), but based on the liquid and vapor Kutateladze numbers and not the dimensionless superficial velocities, has also been suggested by several researchers. The Kutateladze number is defined as

$$Ku_n = \left[\frac{\rho_i^2 v_{sn}^4}{(\rho_l - \rho_v)g\sigma}\right]^{0.25} \qquad n = l, v \tag{2.48}$$

Zapke and Kröger [96ZA1] conducted experiments to determine the flooding vapor velocities for adiabatic countercurrent two-phase flow in a 30 mm ID tube with a sharp inlet. Experiments were performed with the tube in a vertical position and inclined at 60° to the horizontal. By making use of different liquids and gases, they were able to ascertain that flooding, defined as that condition where the vapor flow starts to carry the liquid up past the liquid feed point, is dependent on the phase Froude numbers and a certain combination of the fluid properties, expressed as a dimensionless group:

$$Zk = \sqrt{(\rho_l d_h \sigma)} / \mu_l \tag{2.49}$$

Using this dimensionless group, the flooding data was initially correlated in terms of the phase Froude numbers and the above-mentioned dimensionless group, Zk as follows:

$$Fr_{sv}^{0.25} + a\, Fr_{sl}^{0.25} = b\, Zk^{c}, \tag{2.50}$$

the values of a, b and c depending upon the tube inclination angle and inlet geometry.

Zapke and Kröger [97ZA2] conducted further flooding tests using flattened tubes of varying height and width, inclined at angles between 0° and 90°. They expressed the flooding data in terms of the superficial vapor Froude number as a function of the liquid

Froude number and the Zk number. The correlation takes into account the effect of tube geometry (height and hydraulic diameter) and inclination angle and is expressed as

$$Fr_{Hsv} = K_{fl} \exp\left(- n_{fl} \times Fr_{dsl}^{0.6} / Zk_{d_h}^{0.2}\right) \tag{2.51}$$

where

$$K_{fl} = 7.9143 \times 10^{-2} + 4.9705 \times 10^{-3} \times \theta + 1.5183 \times 10^{-4} \times \theta^2 - 1.9852 \times 10^{-6} \times \theta^3 \tag{2.52}$$

and

$$n_{fl} = 18.149 - 1.9471 \times \theta + 6.7058 \times 10^{-2} \times \theta^2 - 5.3227 \times 10^{-4} \times \theta^3 \tag{2.53}$$

and θ the inclination angle in degrees.

Both equations (2.50) and (2.51) were derived for adiabatic two-phase flow. Reuter and Kröger [96RE1] investigated flooding during reflux condensation in a water-cooled vertical and inclined (60° to the horizontal) tube. Using equation (2.50) as a basis, they derived a correlation that was directly applicable to flow in a dephlegmator tube. Since all the steam condenses in the tube, the relation

$$\rho_v v_{sv2} = \rho_l v_{sl2}$$

at the tube inlet was used to express the dimensionless superficial vapor flooding velocity only as a function of the Zk number and the phase densities. For a 30 mm I.D. round tube at an inclination angle of 60°, they correlated their flooding data as follows:

$$v_{sv}^{*0.5} = \frac{0.869\, Zk^{0.014}}{1 + 1.734\left(\rho_v / \rho_l\right)^{0.25}} \tag{2.54}$$

2.4. The Zapke-Kröger dephlegmator header-to-header pressure drop model

In the previous sections, various models and correlations to calculate two-phase contraction and frictional pressure losses have been discussed. Most of these models and correlations tend to be complex and not particularly suited to flow in a dephlegmator tube. Zapke and Kröger [97ZA1] however, developed an analytical pressure drop model applicable specifically to dephlegmators with flat or elliptical tubes. This model will now be applied to a single dephlegmator tube.

Referring to Figure 2.1, if it is assumed that all the steam condenses in the tube, and the ejector suction rate is negligible, then the condensate mass flow rate flowing out of the bottom of the tube must equal the vapor mass flow rate entering the tube:

$$m_{c2} = m_{v2} \tag{2.55}$$

Generally the heat transfer can be considered a constant heat flux process which implies that the steam condensed uniformly along the length of the tube. The vapor superficial velocity at any position z, where z is in the axial direction, can therefore be related to the vapor superficial inlet velocity as follows:

$$v_{sv} = v_{sv2}\left(1 - \frac{z}{L_t}\right) \tag{2.56}$$

The tube inlet pressure drop, Δp_{12}, may be calculated using the two-phase contraction coefficient, K_{TP}:

$$\Delta p_{12} = p_1 - p_2 = \frac{1}{2}\rho_v v_{sv2}^2\left(K_{TP} - \sigma_{21}^2\right) \tag{2.57}$$

where K_{TP} is evaluated using equation (2.45). The pressure drop in the tube, Δp_{23}, is broken into 3 components, symbolically expressed in equation (2.2). In integral form, Δp_{23} can be expressed as

$$\Delta p_{23} = \int_0^{L_t} \beta (dp_f/dz)_{TP} dz + \int_0^{L_t} g\rho_v \sin(\theta) dz + \int_0^{L_t} -\frac{d}{dz}(\rho_v v_{sv}^2) dz \qquad (2.58)$$

The two-phase frictional pressure gradient is determined by rearranging equation(2.24) as follows:

$$\left(\frac{dp_f}{dz}\right)_{TP} = \frac{1}{2}\rho_v v_{sv}^2 \frac{K_f}{d_h} Re_{sv}^{n_f} \qquad (2.59)$$

and the condensation enhancement factor, β, is calculated using equation (2.31). The pressure drop in the tube is calculated by substituting equation (2.56) into each term on the right hand side of equation (2.58) and integrating over the length of the tube. The frictional pressure change component is evaluated as

$$\Delta p_{f23} = \frac{1}{2}\rho_v v_{sv2}^2 \left[\frac{L_t}{d_h} K_f \, Re_{sv2}^{n_f} \left(\frac{a_n}{n_f + 3} + \frac{b_n}{(n_f + 2) Re_{sv2}}\right)\right] \qquad (2.60)$$

The gravitational component is given by:

$$\Delta p_{g23} = \rho_v g L_t \sin(\theta) \qquad (2.61)$$

The assumption that no vapor exits the tube, firstly means that the change in pressure due to the momentum change of the vapor can be expressed directly in terms of the momentum of the vapor entering the tube. The pressure change due to a change in momentum is

$$\Delta p_{m23} = -\rho_v v_{sv2}^2 \qquad (2.62)$$

Secondly, the change in pressure due to the flow area expansion, Δp_{34} is zero. The total header-to-header pressure drop for a single row dephlegmator is therefore the sum of equations (2.57) and (2.60) to (2.62). The vapor velocity at which flooding occurs,

resulting in a sharp increase in the pressure drop across the headers, can be calculated using equation (2.51).

The pressure drop model described above presents a fairly simple means of calculating the header-to-header pressure drop in a dephlegmator tube. It is, however, based on adiabatic two-phase flow pressure gradient and inlet loss measurements. One of the aims of this investigation is to verify by experiment the applicability of the model to a dephlegmator with reflux condensation. Note that in Appendix A the Zapke-Kröger pressure drop model has been applied to two tubes of a double row dephlegmator.

CHAPTER 3

PREDICTING THE HEAT TRANSFER RATE OF A DEPHLEGMATOR TUBE

In the previous chapter a two-phase pressure drop model proposed by Zapke and Kröger [97ZA1], with which the header-to-header pressure drop in a dephlegmator tube can be calculated, was considered. In order to calculate the pressure drop, the superficial vapor velocity at the tube entrance (v_{sv2} in Figure 2.1) must be known. The vapor superficial velocity at this point can be calculated from the condensate mass flow rate exiting the tube:

$$v_{sv2} = m_c / (\rho_v A_c) \tag{3.1}$$

The condensate mass flow rate is a function of the heat transfer rate in the tube:

$$m_c = Q / i_{fg} \tag{3.2}$$

where Q is the heat transfer rate in the dephlegmator tube.

Therefore, in order to predict the header-to-header pressure drop in a dephlegmator tube, it is necessary that the heat transfer rate of the dephlegmator tube be determined accurately. An analytical method of predicting the heat transfer rate using the air mass flow rate and inlet temperature will now be discussed.

3.1. An analytical method of predicting the heat transfer rate in an air-cooled dephlegmator tube

Consider a forced draft air-cooled dephlegmator tube as depicted schematically in Figure 2.1. For the purpose of this analysis, it is assumed that the air inlet temperature and the air mass flow rate flowing over the dephlegmator are known. The airside heat transfer rate can then be expressed as

$$Q_a = m_a c_{pa} (T_{ao} - T_{ai}) \tag{3.3}$$

where the specific heat is evaluated at the mean air temperature. The airside heat transfer rate equals the steamside heat transfer rate, the latter expressed in terms of the condensate mass flow rate as

$$Q_s = m_c i_{fg} \tag{3.4}$$

Alternatively, the heat transfer rate can be expressed in terms of the theoretical maximum possible heat transfer rate and the heat exchanger effectiveness:

$$Q = e m_a c_{pa} (T_s - T_{ai}) \tag{3.5}$$

In an air-cooled dephlegmator tube the steam condenses at essentially a constant temperature. When the temperature of the fluid within the heat exchanger tubes remains constant, the effectiveness of a single tube heat exchanger is given by Holman [92HO1] as

$$e = 1 - \exp(-NTU) \tag{3.6}$$

where NTU is the number of transfer units, given as

$$NTU = UA / C_{min} = UA / m_a c_{pa} \tag{3.7}$$

According to Kröger [86KR1], the overall heat transfer coefficient based on the airside heat transfer area may be expressed as

$$U_a = \left[\frac{1}{h_a e} + \frac{A_a}{h_c A_c} + \sum_n \frac{A_a R_n}{A_n} \right]^{-1} \tag{3.8}$$

where the summation term represents all the thermal resistances other than the air- and steamside values. These include the thermal contact resistance, tube wall resistance and

the resistance due to fouling and corrosion. It is possible to define an effective heat transfer coefficient based on the airside heat transfer surface area as follows [86KR1]:

$$h_{ae}A_a = \left[\frac{1}{h_a e A_a} + \sum_n \frac{R_n}{A_n}\right]^{-1} \tag{3.9}$$

Substituting equation (3.9) into equation (3.8), the overall heat transfer coefficient based on the airside heat transfer surface area is expressed as

$$U_a A_a = \left[\frac{1}{h_{ae}A_a} + \frac{1}{h_c A_c}\right]^{-1} \tag{3.10}$$

Kröger [86KR1] defined a dimensional characteristic heat transfer parameter, Ny, i.e.

$$Ny = \frac{h_{ae}A_a}{A_{fr}k_a\,Pr_a^{0.333}} \tag{3.11}$$

The characteristic heat transfer parameter is determined experimentally as a function of a dimensional characteristic flow parameter for a specific finned tube. It is normally expressed in the following form

$$Ny = a_{Ny}Ry^{b_{Ny}} \tag{3.12}$$

where Ry is the characteristic heat exchanger flow parameter defined as

$$Ry = m_a / \mu_a A_{fr} \tag{3.13}$$

Referring to equation (3.10), an expression for the condensation heat transfer coefficient is necessary. Groenewald [93GR1] derived an expression for the mean heat transfer coefficient for filmwise condensation on one wall of a flattened tube. Since geometrically there is not a significant difference between an elliptical and a flattened tube, the condensation heat transfer coefficient for an elliptical tube can be

approximated using the condensation coefficient for a flattened tube. Groenewald expressed the condensation coefficient as

$$h_c = 0.9245\left[\frac{L_t k_l^3 \rho_l^2 g \cos\theta\, i_{fg}}{\mu_l m_{aw} c_{pam}(T_s - T_{ai})\left[1-\exp\left(-\frac{L_t H_t U_c}{m_{aw} c_{pam}}\right)\right]}\right]^{\frac{1}{3}} \tag{3.14}$$

where

$$m_{aw} = m_a / 2 \tag{3.15}$$

is the air mass flow rate over one side or half of the tube. The overall heat transfer coefficient based on the condensation surface area of a single tube can be approximated as

$$U_c = h_{ae} A_a / 2 H_t L_t \tag{3.16}$$

The surface area exposed to the vapor in a dephlegmator tube is

$$A_c = P_{et} L_t \tag{3.17}$$

In order to determine the heat transfer rate of an air-cooled dephlegmator tube, an iterative process is necessary. Usually an initial air outlet temperature is chosen. The thermophysical properties of the air are then calculated at the mean air temperature. Using the mean air properties, the heat transfer rate is calculated from equation (3.5). Rearranging equation (3.3) as follows:

$$T_{ao} = T_{ai} + \frac{Q_a}{m_a c_{pa}} \tag{3.18}$$

a new air outlet temperature can be calculated. This process is repeated until T_{ao} has converged satisfactorily.

3.2. The effect of the accumulation of non-condensable gases

In the heat transfer analysis described above, it was assumed that the finned tube was completely filled with vapor. However, in most industrial applications where a vapor is condensed, there are small concentrations of non-condensable contaminants. When the condensing system operates below atmospheric pressure as in most air-cooled steam condensers, air also tends to leak into the system and often accumulates in certain tubes or entire tube rows of a condenser. The effect that the accumulation of non-condensable gases has on the heat transfer of the condenser was not considered in the above analysis.

Various researchers, including Berg and Berg [80BE1] and Breber et al. [82BR1], have investigated the cause and effect of the accumulation of non-condensable gases on the performance of a condenser. Non-condensable gas accumulation normally takes place if a backflow region is present in certain tubes of a condenser. A backflow region is that region in a tube where the direction of the vapor flow is opposite to the normal flow direction and is caused by an unequal heat transfer in the finned tubes. The tubes exhibiting a higher condensation rate will potentially have a higher header-to-header pressure drop. However, since the inlet and outlet headers are common to all the tubes, the tubeside pressure drop must be the same for every tube and vapor therefore flows from the tubes with a lower condensation rate via the outlet header into the tubes with the larger heat transfer. At the front where the upward flowing vapor meets the downward flowing vapor, the system pressure is at its lowest value and it is at this point that non-condensable gases usually start to collect, i.e. at point 5 in Figure A.1.

According Berg and Berg [80BE1], the accumulation of non-condensables will continue until the non-condensable pocket in each tube reaches the tube outlet. Both [80BE1] and Breber et al. [82BR1] proposed methods with which the portion of the tube occupied by the non-condensable gases may be calculated. Berg and Berg showed that in certain cases up to approximately 35% of the entire tube can be filled with non-condensables. This results in a decrease in the effective length of the finned tube and thus a decrease in the thermal efficiency of the condenser. Further detrimental effects of such an accumulation of non-condensable gases include increased corrosion within the tubes and an increased probability that the condensate might freeze in the tubes during winter when ambient temperatures are below 0 °C.

CHAPTER 4

THE EXPERIMENTAL APPARATUS

The Zapke-Kröger pressure drop model, with which the header-to-header pressure drop in a dephlegmator tube can be calculated, depends to a certain extent on adiabatic two-phase countercurrent flow experimental measurements in a flat-profile tube. However, the applicability of this model to vapor flow during reflux condensation in a dephlegmator tube had, prior to the work done for this thesis, not been verified by experiment. This chapter describes the experimental apparatus used and the procedure followed to ascertain experimentally whether the Zapke-Kröger pressure drop model is applicable to reflux condensation.

4.1. Design specifications and basic design of the apparatus

Bellstedt [91BE1] and Groenewald [93GR1] conducted two-phase pressure drop tests in round and flattened finned tubes respectively. Elliptical finned tubes are also used in industry, but very limited two-phase pressure drop data are available in literature for these tubes. Therefore a typical industrial elliptical finned tube was chosen for this investigation. However, due to the size of the laboratory (7.5 m high x 10 m x 8 m), the length of the finned tube had to be restricted to 7 m.

When designing the apparatus, various specifications had to be met. They included:

a) The inclination angle of the finned tube used in the investigation had to be approximately 60°;
b) Dry steam ranging in temperature from 45°C to 65°C was to be used in the experimental tests;
c) The heat transfer had to be accurately controlled and measured in the range 8 kW to 30 kW;
d) The accumulation of non-condensable gases had to be minimized;
e) The header-to-header pressure drop had to be accurately measured within the aforementioned steam temperature and heat transfer ranges;

f) It had to be possible to study the occurrence of flooding during reflux condensation using the apparatus.

The specifications listed above were set to ensure that firstly, the operation of the experimental apparatus simulated an actual industrial dephlegmator tube, and secondly, that the experimental data measured would be sufficiently accurate to compare them with the theoretical predictions of the Zapke-Kröger pressure drop model and flooding correlation.

Apart from the header-to-header pressure drop and flooding tests, it was required that the effect of the presence of a backflow region and the subsequent accumulation of non-condensable gases in the finned tube be investigated. Although not required for the present investigation, provision also had to be made to study the effect of a net outflow of steam from the top of the finned tube.

The experimental apparatus is schematically depicted in Figure 4.1. The apparatus consists of a steam generator (1) that supplies steam to an elliptical finned tube (5). The steam is introduced into the tube via a radial steam inlet and inlet header (4). An outlet header (6) is connected to the top end of the tube. The entire finned tube is mounted in a wooden casing (8), which also serves as a support frame. An air outlet manifold (9) is situated on the wooden casing and is connected to a centrifugal fan (10) situated outside the laboratory. The fan is used to suck air over the finned tube, through the air outlet manifold and out of the laboratory. A water-driven ejector (18) evacuates the entire system of non-condensable gases. To cause the formation of a backflow region in the finned tube, a steam by-pass pipe (11) is used to supply steam directly to the outlet header. A water-cooled aftercondenser (12) draws steam from the outlet header when connected to it, thereby making it possible to study the effect of a net outflow of steam from the top of the tube. Each component will now be discussed in detail.

4.2. The steam generator

The steam generator or boiler, depicted in Figure 4.2, is a shell and tube heat exchanger consisting of 2 passes with 25 stainless steel tubes per pass. The water from which the

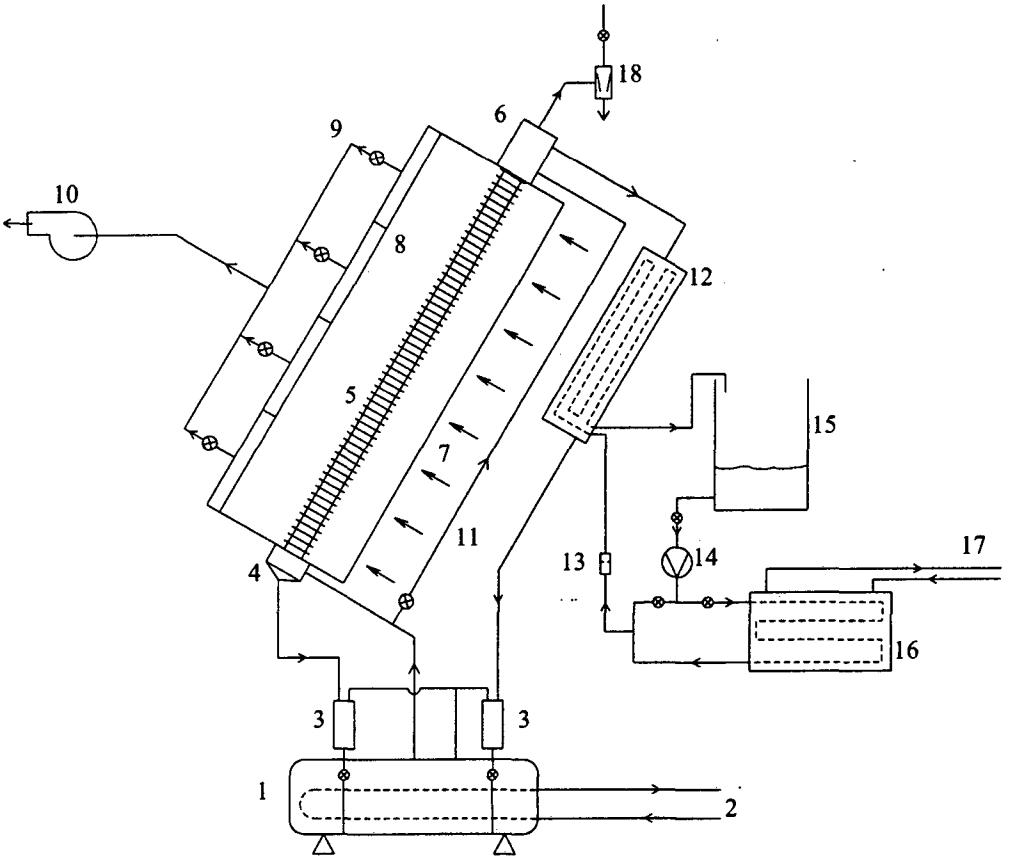

Figure 4.1: A schematic representation of the experimental apparatus

1	Steam generator / Boiler	10	Centrifugal fan
2	Hot water supply lines	11	Steam by-pass pipe
3	Condensate mass flow rate measuring flask	12	Steam aftercondenser
		13	Orifice plate flow meter for aftercondenser cooling water
4	Steam inlet header and condensate drainage point	14	Cooling water pump
5	Elliptical fin tube	15	Cooling water reservoir
6	Steam outlet header	16	Shell-and-tube cooling water chiller
7	Air inlet		
8	Wooden casing and frame	17	Cold water supply lines
9	Air outlet manifold	18	Ejector

steam is generated covers the tubes, while heating water from a remote hot water supply tank is pumped through them. The temperature of the hot water supply is controlled by

means of a combination of 6 electrical elements with power ratings of 1.5 kW, 2 kW, 4 kW, 9 kW, 18 kW and 32 kW respectively. The advantage of this system is that steam at a constant temperature can be generated as opposed to the direct use of electrical elements resulting in the delivery of a constant heat flux.

Additional devices include a water level sightglass, 3 condensate inlets located at the bottom of the generator to which measuring flasks are attached (only 1 measuring flask has been indicated in Figure 4.2.), a drain pipe and a conical sieve that serves as an entrainment limiting device.

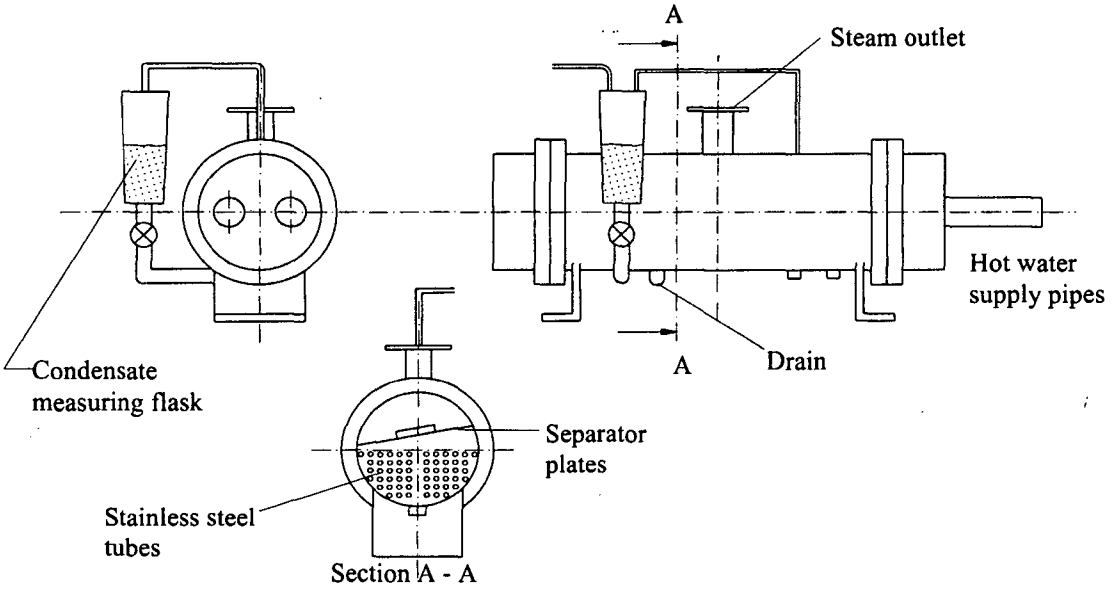

Figure 4.2: The steam generator with only one measuring flask depicted

4.3. The radial steam inlet and inlet header

Figure 4.3 is a schematic diagram of the radial steam inlet. Steam is supplied via a 75 mm ID flexible stainless steel tube from the steam generator to the steam inlet. This tube is insulated to minimize heat loss to the surroundings as well as to ensure that dry steam enters the tube. The inlet, designed and used initially by Bellstedt [91BE1], has a spiral inlet duct and guide vanes that ensure the steam is vortex free on entering the finned tube. The condensed steam flows via an outlet pipe situated at the bottom of the inlet into a measuring flask that is connected to the steam generator.

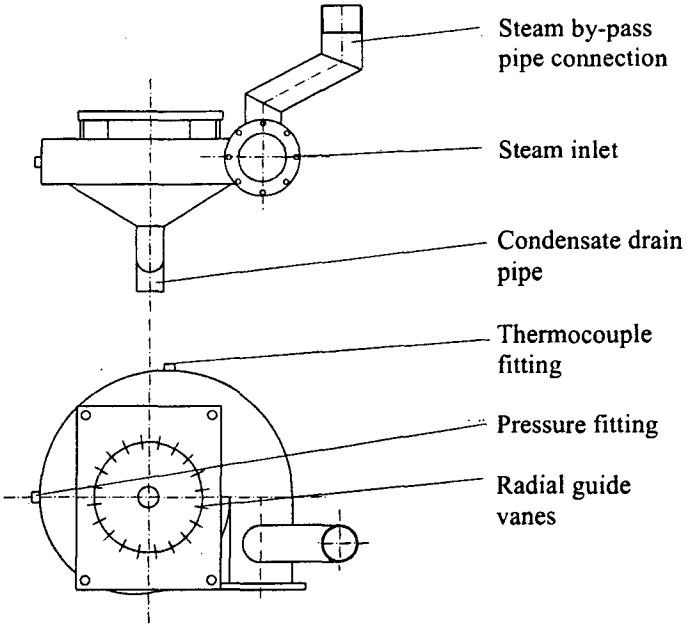

Figure 4.3: The radial steam inlet

Temperature and pressure tapping points are also located at the inlet. Furthermore, a connection for a steam by-pass pipe is attached through which steam can be directly supplied to the steam outlet header. A ball valve (not indicated in Figure 4.3) controls the steam flow in the by-pass pipe.

As shown in Figure 4.4, the inlet header comprises the radial steam inlet, a sightglass

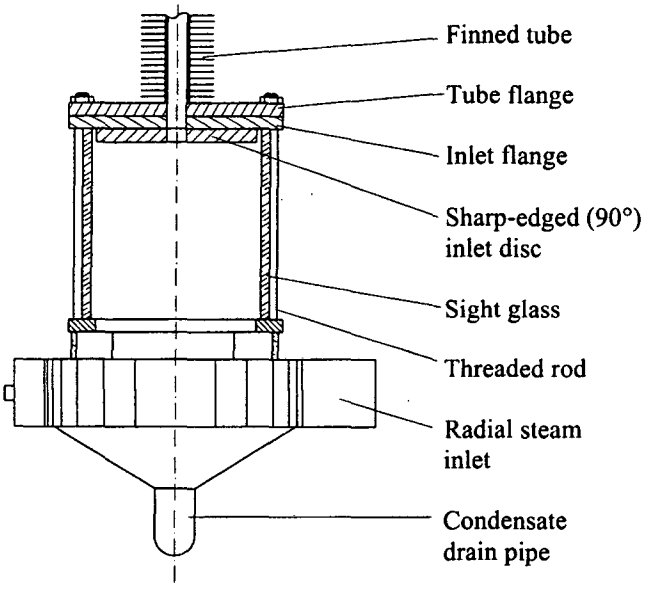

Figure 4.4: The steam inlet header

and an inlet flange. Sandwiched between the radial steam inlet and an inlet flange is a 140 mm ID glass cylinder, thereby making it possible to visually study the condensate-vapor interaction at the bottom of the tube. The inlet flange connects directly to the bottom flange of the finned tube. Attached to this flange is a removable inlet disc. A sharp- or a rounded tube inlet can be obtained by using the appropriate inlet disc. In this investigation a sharp-edged inlet was used.

4.4. The finned tube

The industrial finned tube used for the purpose of this investigation is a hotdipped galvinized elliptical finned tube made of carbon steel. The tube, schematically depicted in Figure 4.5, has the following geometrical specifications:

Tube length,	L_t	= 7 m
Tube inside height,	H_t	= 0.097 m
Tube inside width	W_t	= 0.016 m
Tube cross-sectional area,	A_{tc}	= 1330×10^{-6} m^2
Tube hydraulic diameter,	d_h	= 25.922×10^{-3} m
Tube inside perimeter,	P_{et}	= 205.2×10^{-3} m^2/m
Fin pitch,	P_{fin}	= 2.5 mm
Fin width,	W_{fin}	= 0.050 m
Fin height,	H_{fin}	= 0.120 m
Tube flange thickness,	t_{tf}	= 0.009 m
Tube frontal area,	A_{fr}	= $(L_t - 2 \times t_{tf}) \times W_{fin}$
		= $(7 - 2 \times 0.009) \times 0.05$
		= 0.3491 m^2

For this particular tube, the characteristic heat transfer parameter is expressed as

$$Ny = 2594.951\ Ry^{0.3184} \qquad (4.1)$$

Steel flanges, 9 mm thick x 200 mm x 160 mm, are attached to either end of the tube. O-rings on both flanges ensure a good seal between the tube flanges and the inlet flange and the outlet header flange.

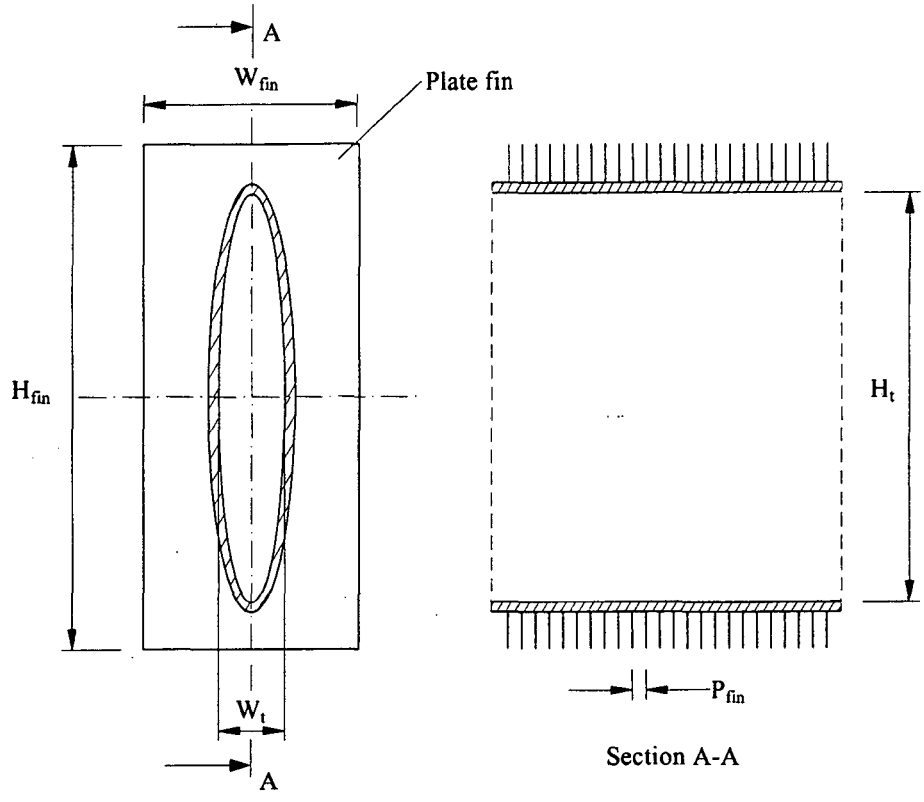

Figure 4.5: A schematic diagram of the experimental elliptical finned tube

4.5. Steam outlet header

The steam outlet header is depicted in Figure 4.6. Basically the outlet header is a stainless steel box with dimensions 250 mm x 170 mm x 80 mm. Two sightglasses are located on either side of the header to aid visual observation of steam flow and condensate build-up in the header.

The outlet header contains three ducts. A 25 mm duct is located at the bottom of the header through which condensate can be drained. Another 25 mm duct located on one side of the header connects the outlet header and an aftercondenser when the latter is in use. On the other side of the header a 50 mm duct serves as the steam inlet when steam is supplied directly to the outlet header. The ducts are sealed with vacuum fittings when not in use.

Pressure and temperature tapping points are located on either side of the outlet header. The pressure in the header is measured at the top two tapping points where condensate

splashing is probably at a minimum, thereby reducing the possibility of condensate build-up in the pressure lines. A suction point where the ejector is connected to the system to remove non-condensable gases is also located on the steam outlet header.

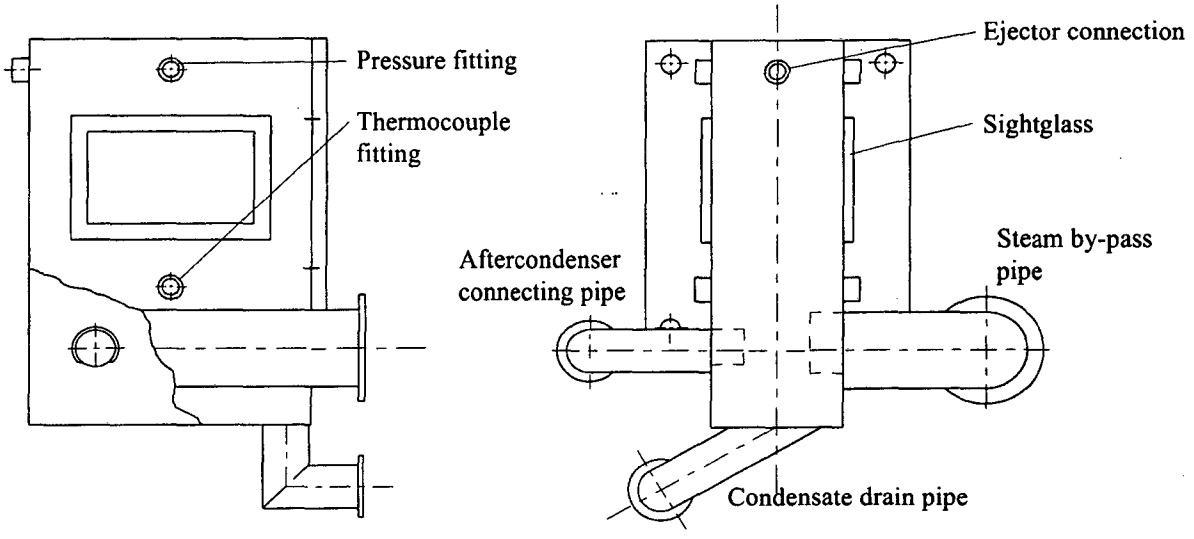

Figure 4.6: The steam outlet header

4.6. Wooden casing and support frame

A wooden casing is used to channel air over the finned tube. The wooden casing and support frame are essentially one structure as can be seen in Figure 4.7. Each side of the frame consists of two 76 mm x 38 mm aluminium tubes, 7.25 m in length. Three plywood sheets, 610 mm wide and with a total length of 6.982 m are attached to the aluminium tubes by means of wooden struts. Rounded aluminium plates are mounted at the bottom of the wooden sheets to form a smooth air inlet.

The two sides of the casing are bolted together with the finned tube mounted between them. The tube is held in place by bolts above and below the fins. The tube rests on the bottom bolts, thereby allowing relative movement between the tube and the casing as the tube expands along its length when heated. The tube is positioned in the wooden casing such that a fully developed air velocity profile is obtained before the tube.

The frame is pivot-mounted at one end to a stand that is bolted to the floor. It is hoisted up to the required elevation angle by means of a cable and pulley system. The cable is

attached to the other end of the frame by means of a bracket. Although beyond the scope of this thesis, provision was also made to tilt the tube and casing around the tube's central axis when it is in a horizontal position.

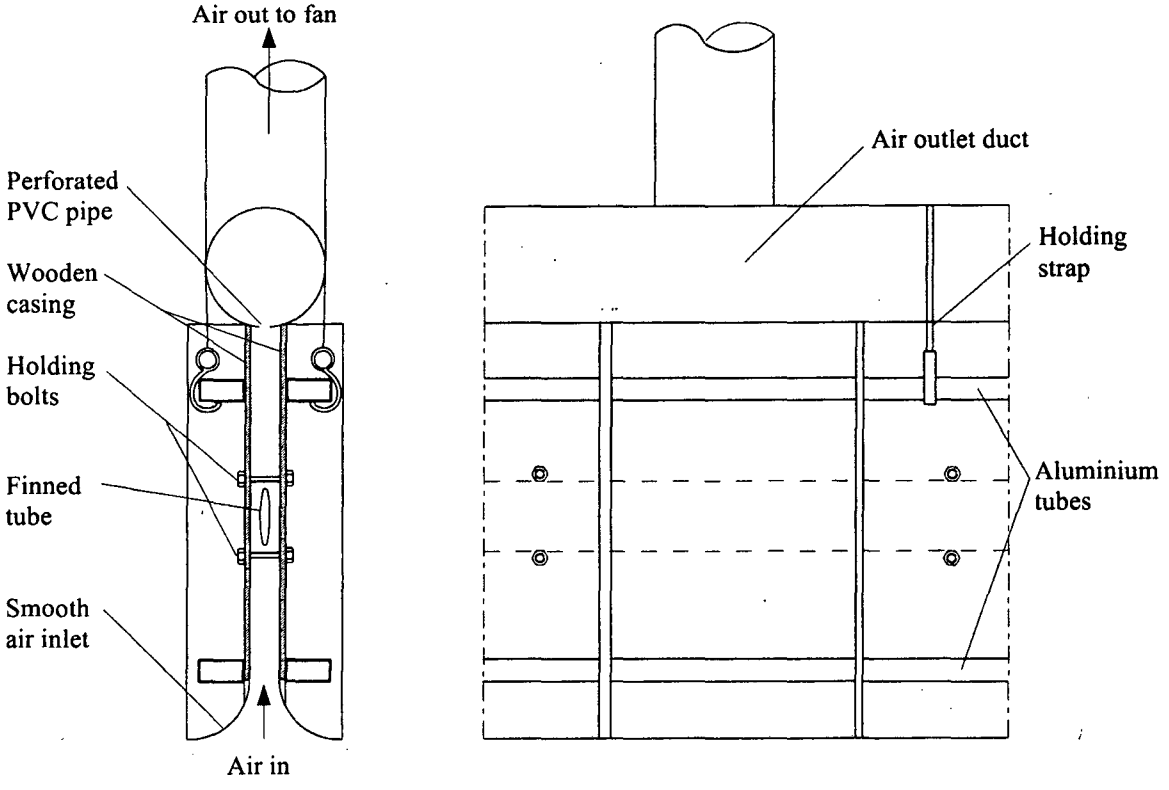

Figure 4.7: A schematic diagram of a portion of the wooden casing and support frame

4.7. The flow-measuring ducts and outlet manifold

As can be seen in Figure 4.7, a 200 mm PVC pipe is placed on top of the wooden casing. This is depicted more clearly in Figure 4.8. The PVC pipe is divided into 4 sections of equal length, each section being sealed at either end. The pipe sections are perforated along the bottom with a large number of 20 mm holes through which the air flowing through the wooden casing is sucked. These holes determine the air flow resistance behind the finned tube and make it possible to obtain a fairly uniform air flow distribution over the entire tube.

Connected to each individual pipe section is a flow-measuring duct, also of 200 mm PVC. Housed in each duct is an anemometer with which the air volume flow rate

through the specific pipe section is measured. The anemometers were calibrated before commencement of the experimental tests. A detailed description of the calibration process can be found in Appendix C. Flow resistance valves are located near the outlets of the ducts and can be adjusted to ensure equal air volume flow rates over each section of the finned tube.

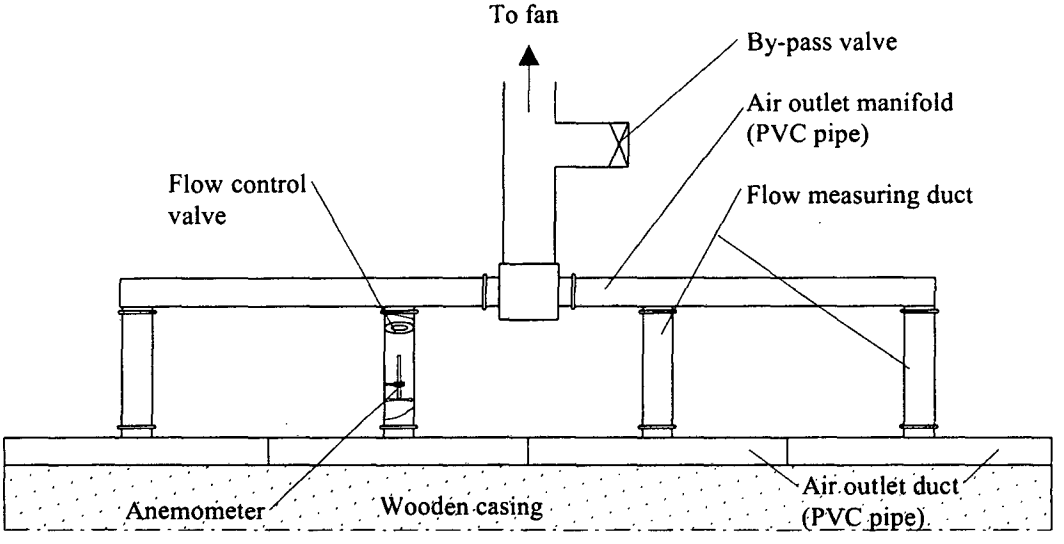

Figure 4.8: The flow measuring ducts and outlet manifold

An outlet manifold ducts the air from each flow-measuring duct via a 400 mm flexible pipe to a fixed speed centrifugal fan. The fan is situated outside the laboratory thereby ensuring that no air recirculation can take place. A by-pass valve, situated between the manifold and the fan, is used to regulate the total air volume flow rate over the finned tube.

4.8. The steam by-pass pipe

A by-pass pipe is used to supply steam to the outlet header when the formation of a backflow region in the top part of the finned tube is desired. A 47.5 mm ID stainless steel tube is used for this purpose. The steam flow in the tube is regulated by means of a ball valve. The total steam volume flow rate through the pipe is determined by measuring the pressure drop along a portion of the tube. The vapor volume flow rate

versus tube pressure drop was calibrated by blowing air through the tube and measuring the corresponding pressure drop.

4.9. The aftercondenser

To obtain a net outflow of steam at the outlet header, an aftercondenser, schematically depicted in Figure 4.9, can be used. Note though that it was not used in this investigation. The aftercondenser is attached to one of the ducts of the outlet header using a vacuum fitting and is mounted on one side of the support frame. The condenser was designed and built by Bellstedt [91BE1], but it had to be slightly modified in order to connect it to the outlet header. The condenser is a shell-and-tube heat exchanger with 6 passes and one tube per pass. Cold water is pumped through the 22 mm copper tube causing the steam to condense on the tube. The water mass flow rate flowing through the condenser is determined by measuring the pressure drop across an orifice plate using a Foxborough pressure transducer. By varying either the water mass flow rate or the average temperature of the cooling water flowing through the tube, the amount of steam flowing into the condenser is regulated. Circulating some of the water through a chiller using two flow-control valves controls the cooling water temperature. The chiller was designed and used by Reuter [94RE1].

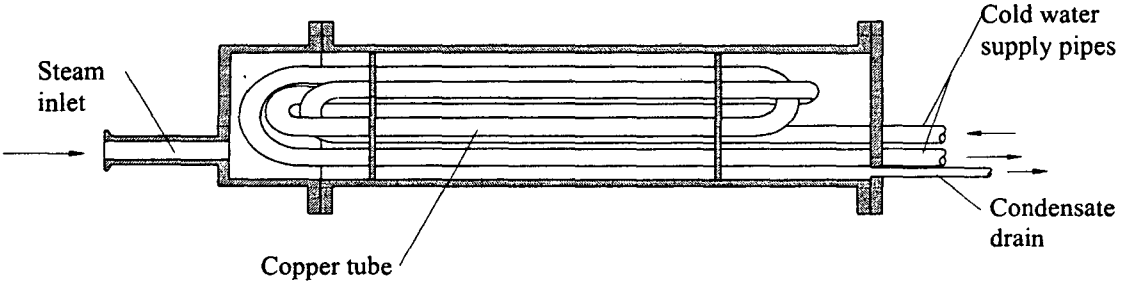

Figure 4.9: A schematic diagram of the aftercondenser

4.10. The vacuum pump

To evacuate the entire system and to ensure that a build-up of non-condensable gases does not take place, a venturi-type vacuum pump is used. The pump is powered directly from the water mains and is connected to the system at the outlet header.

4.11. Measuring instrumentation

Temperatures, pressure differences and air and steam volume flow rates are measured during an experimental run. Each type of measurement will now be described briefly.

4.11.1 Temperature measurements

Copper-constantan thermocouples (T-type thermocouples) are used to measure the various temperatures necessary for experimental and calculation purposes. Thermocouples are located in the following places:

- One thermocouple measures the steam inlet temperature at the steam inlet.
- Two thermocouples are used to measure the steam outlet temperature in the outlet header.
- Six thermocouples equally spaced on the rounded air inlet plates measure the air inlet temperature over the entire length of the tube. This is necessary as a temperature variation occurs between ground level and the roof of the laboratory. The average air inlet temperature for each section of the tube is determined using these thermocouples.
- Twelve thermocouples, also equally spaced, are located in the wooden casing downwind of the finned tube to give an indication of the air outlet temperature profile. These temperature measurements are not very accurate since the air does not mix sufficiently in the wooden casing.
- Two thermocouples per air measuring duct are used to obtain an accurate reading of the average air outlet temperature in each section of the tube.
- One thermocouple is used to measure the steam temperature in the aftercondenser when it is in use.
- The cooling water inlet and outlet temperatures flowing through the after-condenser are measured by two thermocouples in both the water inlet and outlet pipes.

4.11.2 Pressure measurements

During the experiments it is required to measure the header-to-header steam pressure drop. The pressure drop over the length of the steam by-pass pipe when steam is being supplied to the outlet header is also measured. When the aftercondenser is used, the pressure drop across the orifice plate is also needed to determine the cooling water mass flow rate. These pressure readings are done using differential inductive Foxborough

pressure transducers. The output current of these transducers is converted to an output voltage using a resistance. This output voltage is then measured. All three pressure transducers were calibrated prior to being mounted on the apparatus.

It was found that steam tended to condense in the pressure lines between the pressure tapping points and the pressure transducers. To prevent this, a heating coil was wrapped around the pressure lines. The temperature between the wire and the tube wall is maintained at a temperature approximately 5°C higher than the steam temperature. This is achieved using a rheostat and a control system. A heating coil is also used to prevent excess condensation in the steam by-pass pipe.

Occasionally, especially when evacuating the entire system, it is required that the system pressure be monitored. For this purpose a mercury manometer is used.

4.11.3 Volume flow rate measurements

The air volume flow rate flowing over each section of the tube is measured in each flow-measuring duct using propeller type anemometers. Their output voltage is proportional to the volume flow rate in each duct. The output voltage-volume flow relationship of each anemometer was determined prior to testing during the calibration process. The calibration is described in detail in Appendix C.

The steam volume flow rate at the tube inlet can be determined by measuring the total condensate volume flow rate. For this purpose three measuring cylinders are used. The largest measuring cylinder is used to measure the condensate flow rate that flows out of the bottom of the finned tube. It is situated between the steam inlet and the steam generator. A second measuring cylinder (not indicated in Figure 4.1) is used to measure the condensate volume flow rate that flows out of the steam outlet header. The third measuring cylinder measures the condensate volume flow rate that condenses in the aftercondenser. In all three cases the condensate gravity feeds back to the steam generator.

As mentioned in the previous section, the steam volume flow rate flowing into the outlet header via the steam by-pass pipe is determined by measuring the pressure drop in the

pipe. The aftercondenser water mass flow rate is similarly calculated using the measured pressure drop across a calibrated orifice plate.

4.12. The data logging system

As can be seen from the previous section a large number of experimental readings need to be taken for each experimental run. This is done using a Schlumberger multiple voltmeter datalogger. The Schlumberger has an internal reference point for T-type thermocouples and is thus ideal for monitoring temperatures. It is also capable of measuring voltages and is therefore also used to monitor the output voltage of the pressure transducers and the anemometers. It scans all the channels once every second and communicates the results to a personal computer via an analog to digital card.

A computer program written in Turbo Pascal is used to visually monitor the data from the Schlumberger. This computer program makes it possible to:

- Monitor all the channels simultaneously;
- Monitor all the thermocouple readings;
- Monitor the pressure transducer and anemometer readings;
- Monitor the heat transfer on both the air and the steam side;
- Monitor the operating conditions of the aftercondenser;
- Obtain an average reading over a specified period by integrating the data during that period;
- Save the average readings to a specified file where the data may be retrieved later for further analysis;
- Do a transient analysis of the system by saving readings to a file at specified intervals for a specified length of time.

4.13. A description of the entire system

The components of the experimental apparatus have been described in the previous sections. The brief summary of the entire apparatus and its operation will now be given. Photographs of the apparatus can also be seen in Figures 4.10 and 4.11.

In Figure 4.10 the steam generator, condensate measuring cylinder and radial steam inlet are clearly visible. Note that when the photograph was taken, the two smaller measuring flasks were not connected to the system. The steam by-pass pipe, the air by-pass valve and the Schlumberger datalogger can also be seen in the photograph.

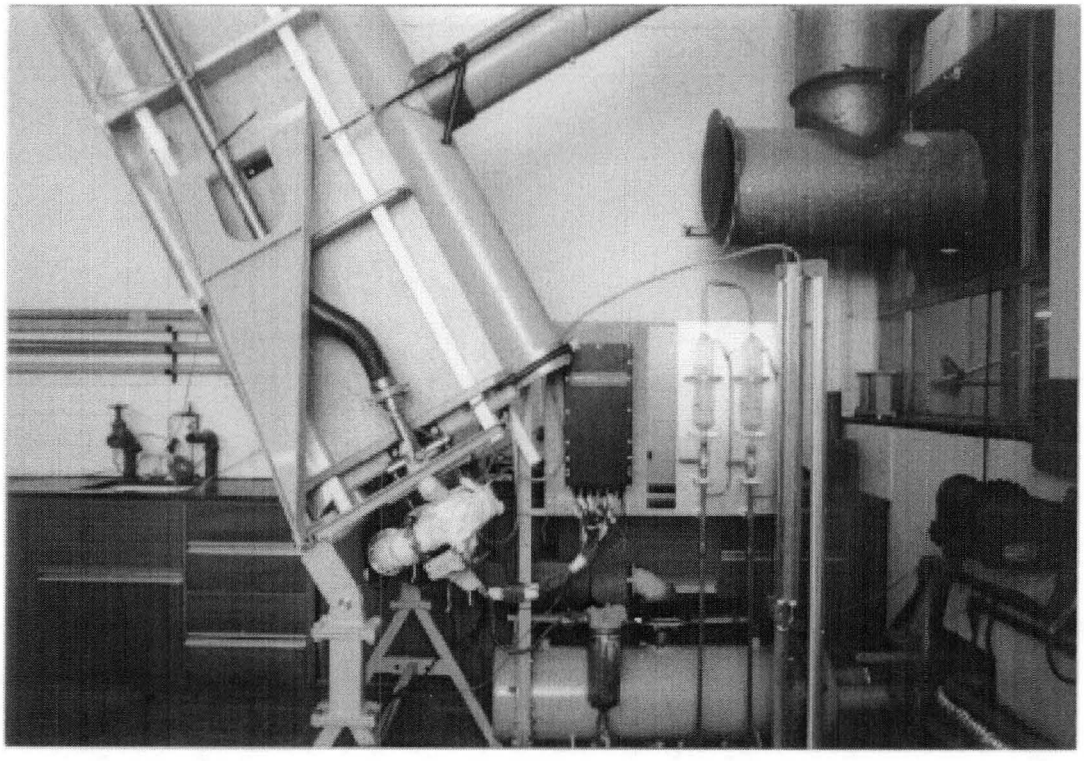

Figure 4. 10: A photograph showing amongst others the steam generator

Hot water at a certain controlled temperature is pumped from a remote hot water supply tank through the steam generator. The entire system on the steamside is under vacuum, a water-driven venturi vacuum pump having reduced the pressure to approximately 10 kPa absolute pressure. The vacuum pump is connected to the steam outlet header. The low system pressure makes it possible to generate steam ranging from 45 °C to 70 °C, depending upon the hot water supply temperature. The steam flows via an insulated flexible stainless steel tube to the radial steam inlet and inlet header. The inlet ensures that vortex free steam enters the tube while also serving as a condensate drain. Connected to the tube flange is an inlet flange and inlet disc. For this particular investigation a sharp-edged (90°) inlet disc was used. The steam flows into the finned tube where it is condensed. The condensate then drains back into the inlet header and from there into a measuring cylinder where the flow rate is measured before gravity

feeding back into the steam generator. However, in the event of condensate being carried up the tube, sightglasses on the steam outlet header make it possible to monitor the conditions at the top end of the tube. Thermocouples are used to measure the steam inlet and outlet temperatures, while a pressure transducer measures the header-to-header pressure drop.

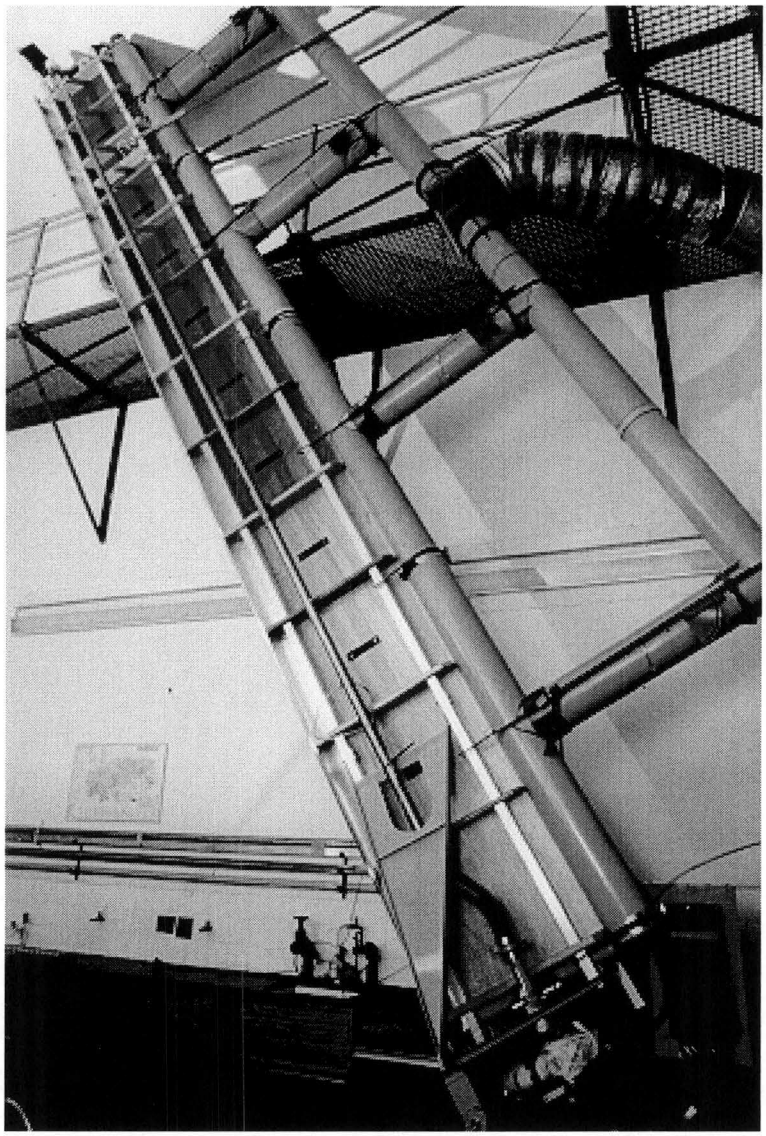

Figure 4. 11: A photograph of the wooden casing and support frame and air outlet manifold.

Figure 4.11 shows the wooden casing with the smooth air inlet and support frame. The air outlet manifold and flow-measuring ducts are also clearly visible. Note the control valves located in each flow-measuring duct. Air is sucked into the wooden casing and

over the finned tube located between each side of the wooden casing. Smooth inlet roundings minimize air entrance disturbances.

The air inlet temperature over the length of the tube is measured with 6 thermocouples, equally spaced over the length of the tube. Twelve thermocouples located above the finned tube measure the air outlet temperature profile, but they do not yield accurate readings for the air outlet temperature as the air has not mixed sufficiently by the time it flows passed these thermocouples. The air then flows into 4 perforated pipe sections located on top of the wooden casing and into the flow-measuring ducts. In these ducts the average air exit temperature in each section as well as the air volume flow rate using propeller-type anemometers is measured. Flow resistance valves in the ducts make it possible to individually adjust the air flow rate over each section. The air is then sucked out via an outlet manifold and ducting to a centrifugal fan located outside the laboratory. A by-pass valve in the air duct is used to adjust the total air volume flow rate over the finned tube. By expelling the air to the atmosphere, recirculation of the air is prevented.

In order to investigate the effect of the presence of a backflow region in a dephlegmator tube, a by-pass pipe is used to supply steam from the inlet header to the outlet header. The steam volume flow rate is controlled with a ball valve located near the inlet header. A pressure transducer measures the pressure drop in the pipe from which the steam volume flow rate may be determined. A heating coil heats the by-pass pipe so as to minimize condensation in the tube.

An aftercondenser, although not used in this investigation, can be used to obtain a net outflow of steam in the outlet header. It is attached to the outlet header using a vacuum fitting and is mounted on one side of the support frame. Cold water is pumped through the condenser, causing the steam to condense on the outside of the condenser tubes. By varying the water mass flow rate and/or the cooling water temperature, the steam flow rate out of the outlet header can be controlled. The flow rate is determined by measuring the condensate mass flow rate in the aftercondenser using a measuring cylinder that is connected to the boiler. The cooling water temperature is controlled using ball valves that adjust the amount of water that is pumped through a chiller. The water inlet and outlet temperatures as well as the water mass flow rate are measured.

4.14. Experimental procedure

To minimize the potential for errors during an experimental run the same procedure is followed each time. Prior to a run, the hot water supply is heated to a temperature about 5°C higher than the required steam temperature. The temperature of the hot water is controlled using a combination of the 6 available heating elements. When the correct temperature is reached, the hot water is pumped through the steam generator. While the heating water is being heated, the vacuum pump is used to evacuate the entire system. The heating wire is also switched on to heat the pressure lines to a temperature approximately 5°C higher than the steam temperature. This prevents any condensate build-up in these lines. The atmospheric pressure and temperature are also noted.

As soon as the entire finned tube has been filled with steam, the centrifugal fan is switched on and the control valves located in the measuring ducts adjusted so that the air volume flow rate over each section of the tube is approximately the same. By adjusting the by-pass valve in the air duct before the fan, the total air volume flow rate flowing over the entire finned tube is reduced to a minimum. Approximately half an hour is then required for the system to stabilize. Here the computer program proved to be invaluable since the temperatures and pressures monitored by the computer give a good indication of when the system has stabilized.

Once the system has stabilized, the first experimental reading can be taken. The condensate volume flow rate is measured using the condensate measuring flask and a stopwatch. The flow rate data are inputted into the computer and the energy balance checked. If the energy balance is satisfactory, the average values of the relevant measured temperatures, pressures and flow rates are obtained using the integration function of the computer program. These average values are then saved to a file where they are retrieved later for calculation purposes.

The air duct by-pass valve is now adjusted again to increase the air flow rate over the tube. Once the system has stabilized again, the next reading can then be taken. The entire process is repeated until the maximum air flow rate possible over the finned tube is reached.

To determine when flooding occurs, it is necessary that the pressure drop in the tube be monitored carefully. The heat transfer, and thus the inlet vapor velocity is increased gradually by increasing the air flow rate over the tube. As the vapor velocity increases, the pressure drop in the tube also increases. At a certain vapor velocity, the pressure drop suddenly rises sharply. This specific velocity is considered the flooding velocity. When flooding occurs in the finned tube, the condensate volume flow rate tends to vary substantially. It is therefore necessary to take about five readings to obtain an average value of the flow rate.

Finally, it is important to note that the vacuum pump continually evacuates the system and is not switched off during an experimental run to prevent the build-up of non-condensable gases in the system. These gases would accumulate in the system over a long period of time if not removed as the system although ideally vacuum tight, tended to leak slightly. Reuter [94RE1] calibrated the vacuum pump and he found that the mass of steam sucked out of the system by the vacuum pump is negligible. The vacuum pump can therefore be used continuously without affecting the experimental results.

CHAPTER 5

EXPERIMENTAL RESULTS

In a typical dephlegmator tube the heat transfer, the header-to-header pressure drop and the occurrence of flooding are all related. Each of these three performance characteristics must therefore be considered to determine the overall performance of such a tube. Experiments were performed using the apparatus described in Chapter 4 to verify whether the pressure drop model proposed by Zapke and Kröger [97ZA1] and the flooding correlation proposed by Zapke [97ZA2] can be used for a pressure drop and flooding analysis in a dephlegmator tube. While condensing steam ranging in temperature from 45 °C to 65 °C in the elliptical finned tube, the heat transfer rate and the pressure drop across the tube headers were measured. The flooding vapor velocity, defined as that velocity at which a sharp increase in the pressure drop in the tube occurs, was also determined for a number of steam temperatures. In this chapter the experimental results obtained in this investigation are presented. Note that most of the data from which the graphs in the following sections were generated have been tabulated in Appendix E.

5.1. The dephlegmator tube header-to-header pressure drop

The procedure followed for each experimental run, during which the header-to-header pressure drop was measured, has been described in section 4.14. According to Zapke and Kröger [96ZA3], at low vapor flow rates the pressure drop is Reynolds number related. However, at high vapor flow rates greater liquid-vapor interaction takes place, resulting in wave formation on the surface of the liquid. The vapor Froude number therefore becomes the governing dimensionless group and the duct height the characteristic dimension. In the experiments performed by Zapke and Kröger [96ZA3] the Reynolds number in the low to moderate vapor flow rate range varied between approximately 400 to 4000 while the vapor Froude number varied between 0.001 and 0.1. In this particular investigation the vapor Reynolds number at the tube inlet varies between approximately 5000 and 20000 and the vapor Froude number between 0.09 and 0.5 which implies that the vapor flow rates were in what [96ZA3] would consider the

moderate to high vapor flow rate range. Figures 5.1 and 5.2, which are plots of the dimensionless pressure drop versus the vapor Reynolds number and Froude number respectively, clearly show that the dimensionless pressure drop is predominately Froude number dependent, which is in agreement with the results obtained by [96ZA3].

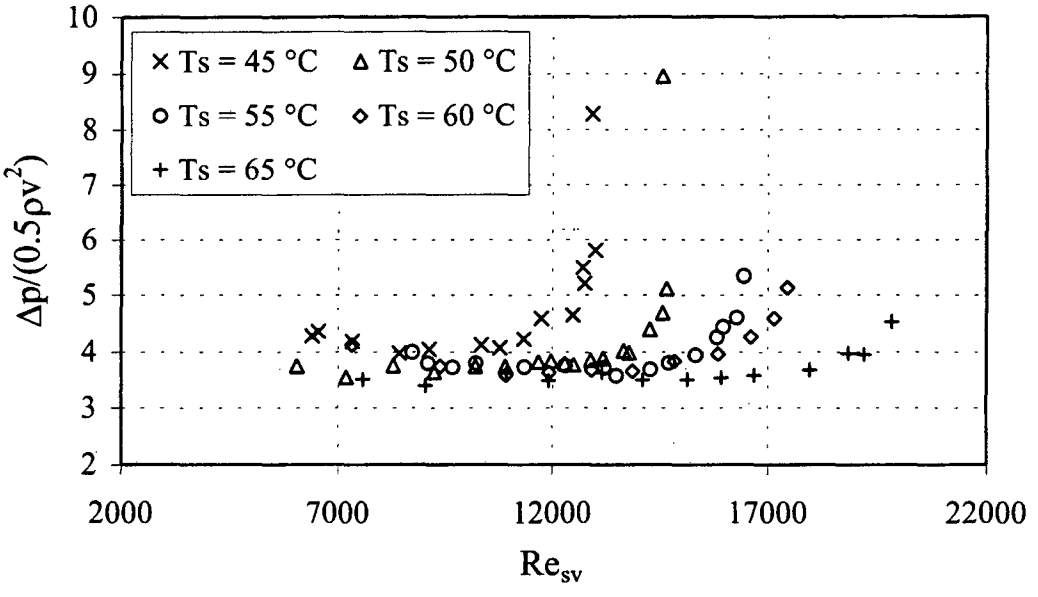

Figure 5.1: The dimensionless pressure drop data plotted versus the vapor Reynolds number.

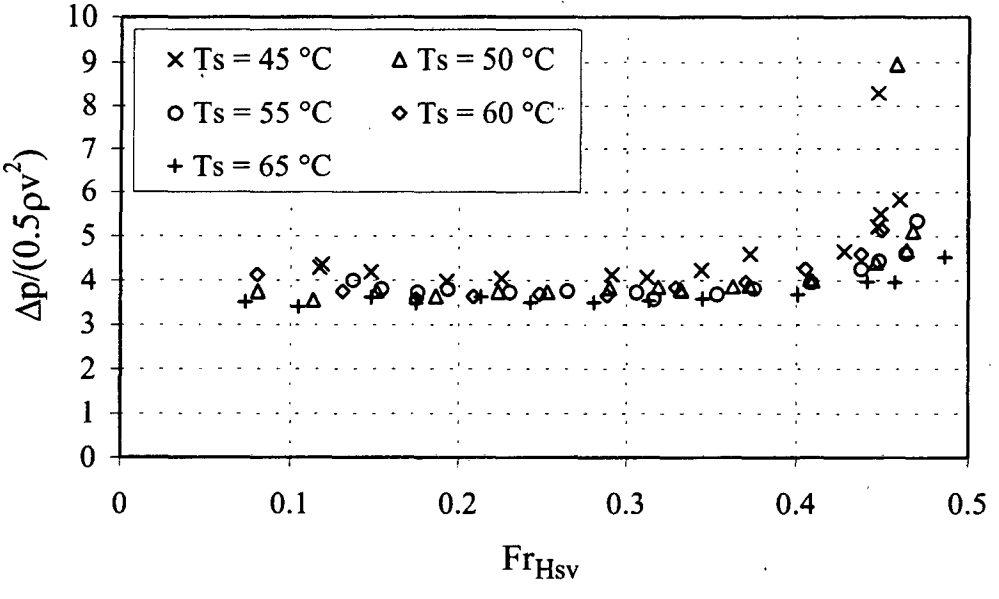

Figure 5.2: The dimensionless pressure drop data plotted versus the densimetric vapor Froude number.

The Zapke-Kröger pressure drop model discussed in Chapter 2 maintains that the header-to-header pressure drop in a dephlegmator tube is a function of both the vapor Reynolds number and the densimetric vapor Froude number. Since the theoretical pressure drop is a summation of pressure drop components that are either Froude or Reynolds number dependent, and these dimensionless groups are functions of amongst others the superficial vapor velocity, it is convenient to plot the pressure drop data in dimensional form in terms of the vapor velocity. This has been done in Figure 5.3 where the measured pressure drop data obtained for three different steam temperatures are compared to the predicted pressure drop as calculated using the Zapke-Kröger pressure drop model. It is clear from the figure below that the predicted and the measured pressure drop data are in close agreement when plotted against the superficial vapor velocity.

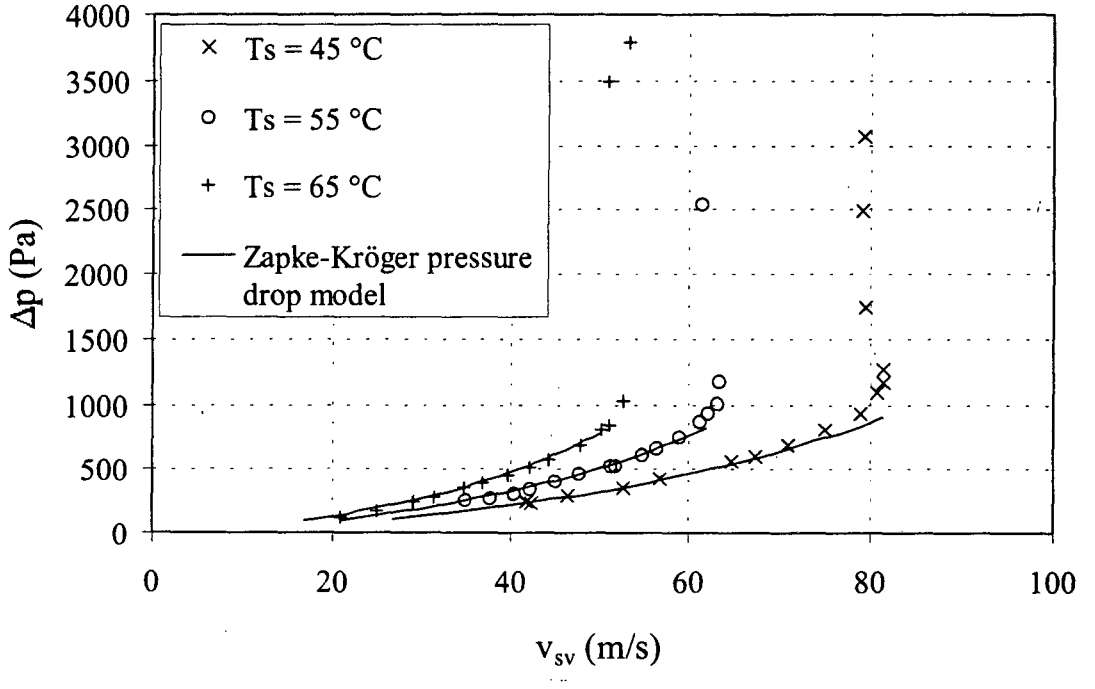

Figure 5.3: The header-to-header pressure drop during the reflux condensation of steam in the elliptical dephlegmator tube with a sharp-edged inlet.

Because Figure 5.3 is in dimensional form, it is difficult to determine from it the maximum vapor velocity for which the pressure drop model still yields satisfactory results for a particular steam temperature. Presenting the data of Figure 5.3 in

dimensionless form would therefore assist in determining the vapor velocity range in which the Zapke-Kröger pressure drop model may be used with confidence to determine the header-to-header pressure drop. As was mentioned above, the vapor Froude number is the dominating dimensionless group in the moderate to high vapor flow range. The data of Figure 5.3 has therefore been plotted in non-dimensional form in terms of the vapor Froude number in Figure 5.4.

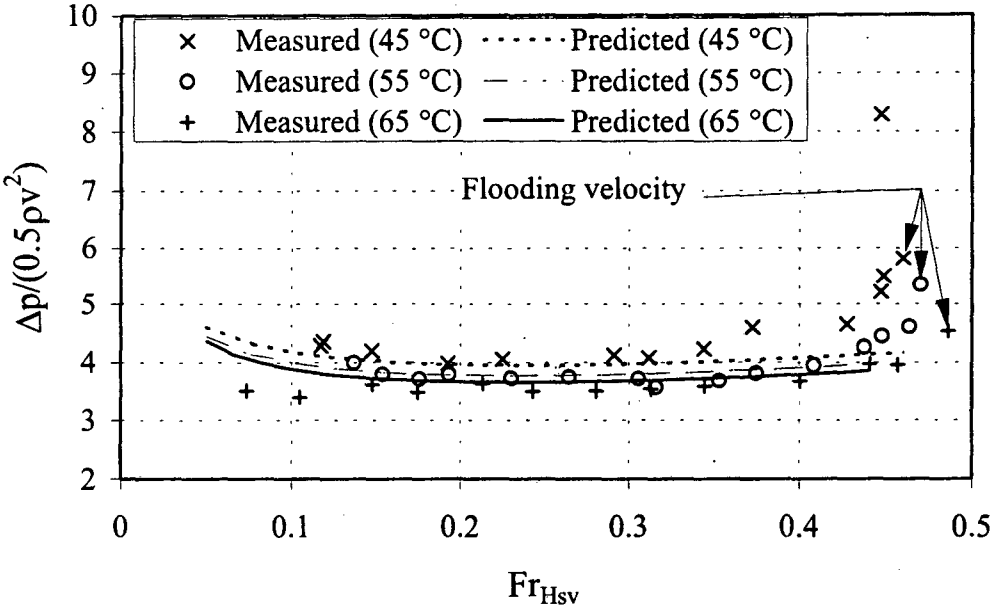

Figure 5.4: The dimensionless pressure drop data plotted against the superficial vapor Froude number for steam temperatures of 45, 55 and 65 °C.

Figure 5.4 clearly shows that the pressure drop model accurately predicts the header-to-header pressure drop in a dephlegmator tube in the range $0.1 \leq Fr_{Hsv} \leq 0.4$. Above $Fr_{Hsv} = 0.4$ the actual pressure drop is slightly greater than the predicted pressure drop. In this region the measured dimensionless pressure drop increases gradually until flooding occurs at which point there is a sharp increase in the pressure drop.

The deviation of the predicted pressure drop from the actual values for $Fr_{Hsv} \geq 0.4$ can possibly be explained if the individual components of the theoretical pressure drop are considered. The various theoretical pressure drop components, calculated using the Zapke-Kröger pressure drop model, as well as the total measured pressure drop have been plotted in Figure 5.5 for a steam temperature of 45 °C.

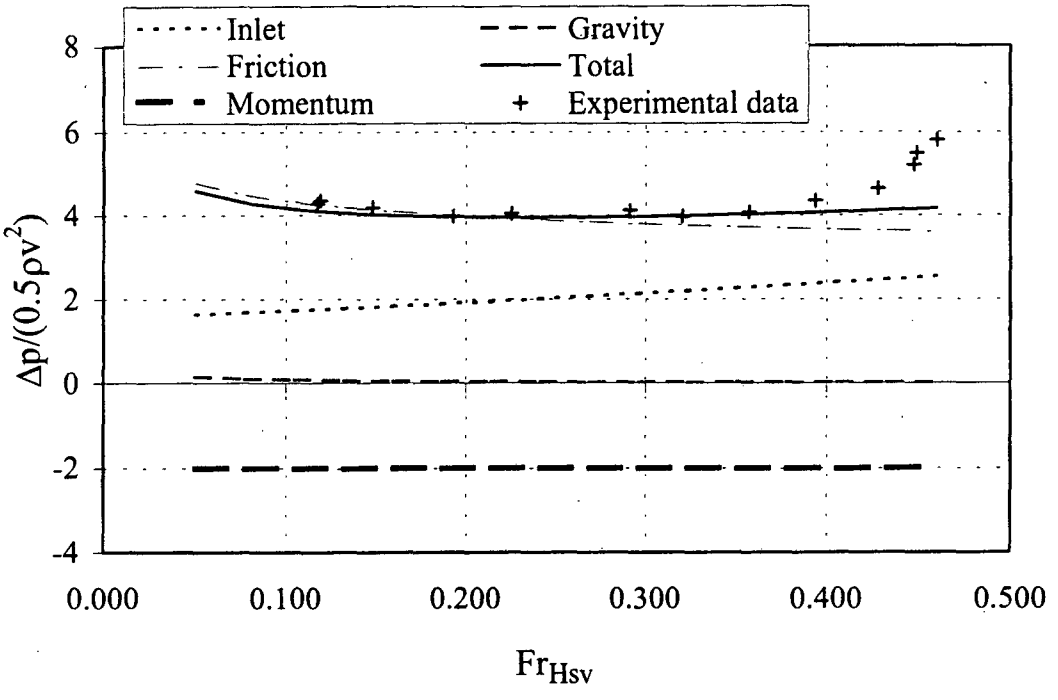

Figure 5.5: The dimensionless pressure drop components plotted versus the superficial vapor Froude number for a steam temperature of 45 °C.

From Figure 5.5 it can be seen that the gravitational component of the total pressure drop is negligible. The momentum change and inlet pressure drop components are of opposite sign, but the same order of magnitude for the specific elliptical tube under investigation and therefore tend to cancel each other out. The frictional component is the major contributing factor to the total header-to-header pressure drop. Note that the frictional component decreases with an increase in the vapor Froude number. It would however be expected that the two-phase friction factor should increase near flooding ($Fr_{Hsv} \geq 0.4$) since the liquid surface becomes more disturbed and the entrainment of liquid droplets in the vapor core increases. The correlation used for the friction factor, equation (2.24), does not exhibit this trend near flooding which possibly explains the deviation of the theoretical pressure drop from the actual measured pressure drop for $Fr_{Hsv} > 0.4$.

To verify the accuracy of the measured pressure drop data, the header-to-header pressure drop was also calculated using the steam inlet and outlet temperatures. Using the steam temperature in each header, the corresponding saturation vapor pressure in

each header was calculated and then subtracted from each other in order to obtain the pressure drop over the headers. This calculated pressure drop is plotted in dimensionless form together with the dimensionless measured pressure drop against the superficial vapor Froude number in Figure 5.6 for steam temperatures of 45, 55 and 65 °C.

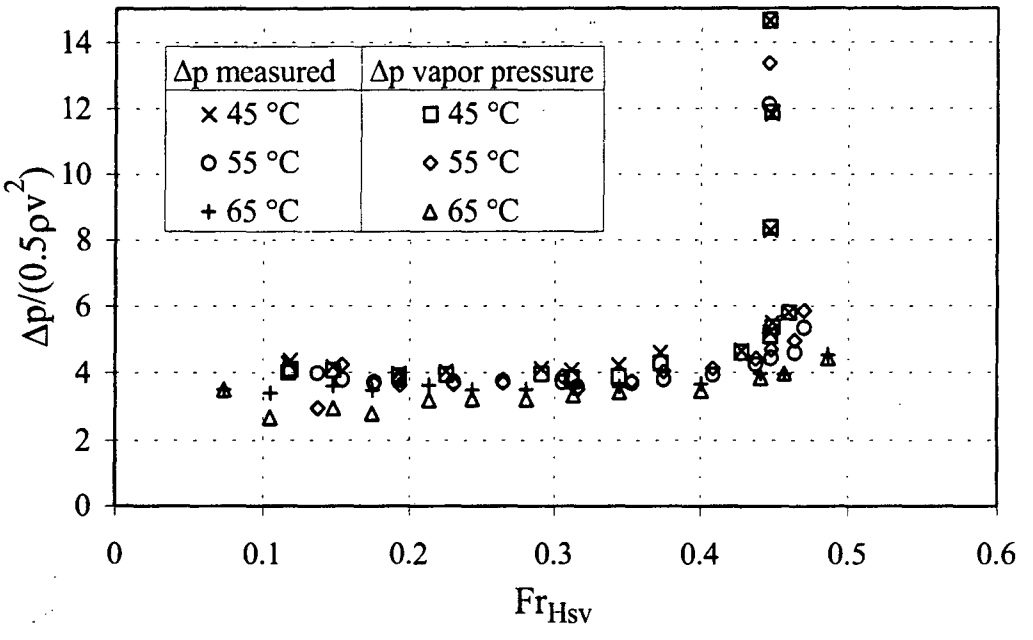

Figure 5.6: The measured pressure drop and the pressure difference between the vapor pressures in the inlet and outlet headers plotted in dimensionless form versus the superficial vapor Froude number for a steam temperatures of 45, 55 and 65 °C.

From Figure 5.6 it is evident that in general the measured pressure drop and the difference in the vapor pressures in the inlet and outlet headers corresponded very closely. However, occasionally during an experimental run the two pressure drop values differed slightly. This can probably be ascribed to the presence of non-condensable gases at the top of the tube, thereby causing the measured outlet temperature to be lower than the saturated steam temperature in the outlet header.

5.2. Flooding in the dephlegmator tube

As was mentioned earlier in this chapter, the flooding vapor velocity in this investigation is defined as that vapor velocity at which a sharp increase in the header-to-

header pressure drop in the tube occurs. This definition is in accordance with that used by other researchers [63EN1, 69DI1, 96RE1]. The procedure for determining the flooding velocity has been described in section 4.14. Note though that in Figure 5.4 the flooding vapor velocities, expressed in terms of the Froude numbers, have been indicated for the respective steam temperatures to visually clarify the definition thereof. Zapke and Kröger [96ZA1, 96ZA2] showed that flooding inside tubes is not related to the vapor Reynolds number, but that the superficial densimetric vapor Froude number is the governing dimensionless group and that the duct height is the characteristic dimension. This is very evident from Figures 5.1 and 5.2. In Figure 5.1 the flooding vapor Reynolds number varies from approximately 13000 to 20000 depending on the steam temperature. In terms of the Froude number flooding occurs at approximately 0.47 irrespective of the steam temperature as shown in Figure 5.2. The slight variation in the flooding vapor Froude numbers is due to the different condensate flow rates at the respective steam temperatures at flooding.

As was mentioned in Chapter 2, Zapke [97ZA2] proposed a correlation for flooding in an inclined flattened tube, expressed as

$$Fr_{Hsv} = K_{fl} \exp\left(- n_{fl} \times Fr_{dsl}^{0.6} / Zk_{d_h}^{0.2}\right) \tag{2.51}$$

where K_{fl} and n_{fl} are given by equations (2.52) and (2.53). In a dephlegmator tube the flooding fluid velocities and properties are such that the expression in brackets on the right hand side of equation (2.51) is very small. Therefore by making use of the Taylor series expansion for an exponential function and neglecting second and higher order terms, equation (2.51) may be written approximately as

$$Fr_{Hsv} = K_{fl} \left(1 - n_{fl} \times Fr_{dsl}^{0.6} / Zk_{d_h}^{0.2}\right) \tag{5.1}$$

For a tube at an inclination angle of 60°, this equation is further simplified to

$$Fr_{Hsv} = 0.49512 \left(1 - 27.7615 \times Fr_{dsl}^{0.6} / Zk_{d_h}^{0.2}\right) \tag{5.2}$$

Equation (5.2) is plotted together with the flooding data obtained using the elliptical finned tube in the present investigation and the flooding data obtained by Reuter and Kröger [96RE1] in terms of the Fr_{dsl}-Zk_{dh} parameter in Figure 5.7.

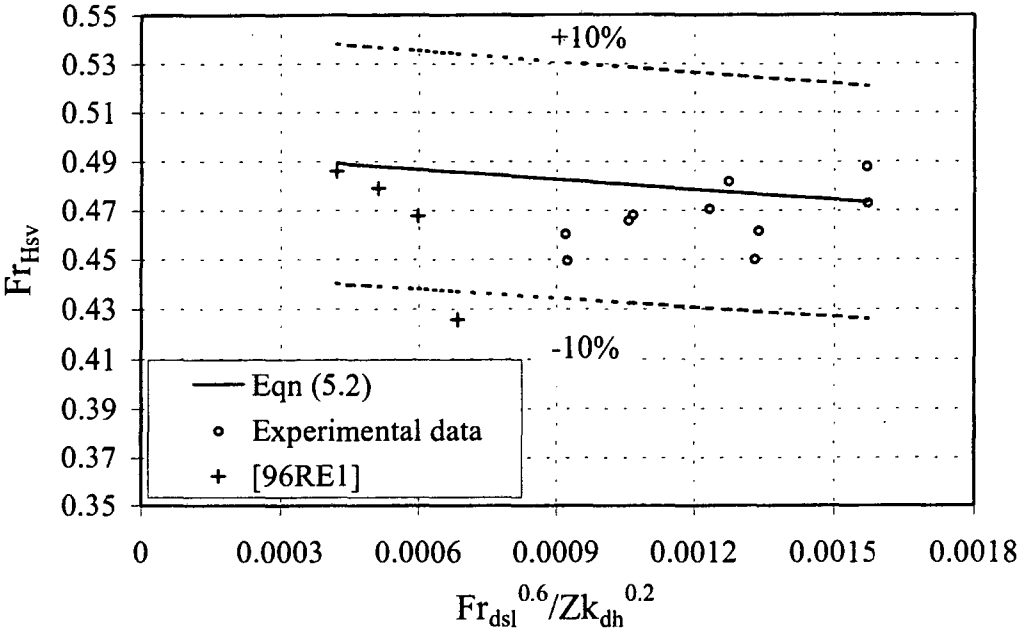

Figure 5.7: The flooding superficial vapor Froude number at the tube entrance.

In Figure 5.7 it can be seen that equation (5.2) correlates the experimental data obtained in this investigation to within ± 10%. The scatter in the experimental data for the elliptical finned tube can be ascribed mainly to experimental errors in measuring the data at or near flooding. Errors are liable to occur in this region firstly due to the manner in which the flooding vapor velocity is determined. Near flooding the vapor velocity is increased incrementally by gradually increasing the air mass flow rate and thus the heat transfer rate of the tube. The flooding velocity is that vapor velocity of which an incremental increase would result in a sudden sharp pressure drop. It therefore follows that the smaller the incremental increase in the vapor velocity, the more accurate the actual flooding velocity can be determined. Secondly, just before and at flooding liquid does not drain freely from the tube, some liquid being entrained by the vapor at the tube entrance and carried up the tube. This results in fluctuations in the condensate flow rate and the airside heat transfer, thereby making it difficult to obtain an accurate heat transfer reading which is necessary to calculate the vapor velocity.

When comparing the experimental flooding data to the flooding correlation, equation (5.2), it is important that the differences in the flow phenomena as observed in this investigation and by Zapke [97ZA2] be considered. As was mentioned in Chapter 2, Zapke conducted adiabatic two-phase flow tests in rectangular ducts inclined at various angles to the horizontal. Various gases and liquids were used as the working fluids. Flooding in the duct was defined as that condition where the gas flow starts to carry liquid up past the liquid feed point. Zapke found that prior to the liquid being carried up past the liquid feed point a transient process of liquid accumulation and draining in the duct took place. The liquid started to accumulate at the duct entrance and was then sporadically propelled up the duct with a rolling motion. Before reaching the liquid feed point the rolling motion broke down, and the liquid drained downward again in a stratified manner. This observed pulsating phenomenon had a significant influence on the various pressure drop components in the duct as shown in Figure 5.8. Note that although the specific data in Figure 5.8 were obtained using air and propanol in a duct inclined at 20° to the horizontal, similar tendencies were also observed for other working fluids and inclination angles.

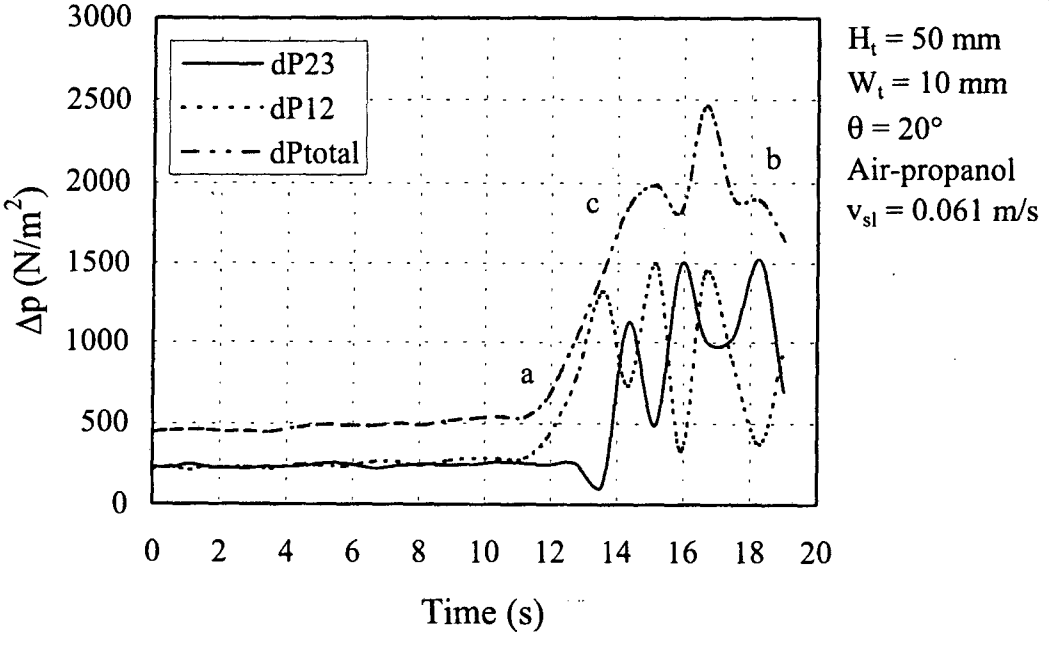

Figure 5.8: Transient pressure drop data measured by Zapke during adiabatic countercurrent two-phase flow in an inclined rectangular duct.

While gradually increasing the vapor flow rate through the duct, Zapke constantly monitored the inlet pressure drop, Δp_{12} and the pressure drop in a portion of the duct, Δp_{23}. The total pressure drop, Δp_{total} is the sum of Δp_{12} and Δp_{23}. Initially as the liquid accumulated at the duct entrance, Δp_{12} increased, but as soon as the liquid was propelled upwards, away from the duct entrance, Δp_{12} decreased and Δp_{23} increased. When the liquid rolling motion broke down, the pressure drop in the duct decreased, while the draining liquid started to accumulate at the duct entrance again resulting in an increase in Δp_{12}. This explains the fact that Δp_{12} and Δp_{23} appear to be out of phase in Figure 5.8. The magnitude of these pressure pulses increased gradually until the flooding velocity was reached at which point the liquid was propelled up beyond the liquid feed point. The cyclic nature of the flow did not cease at flooding though. Note that in Figure 5.8 there was a sharp increase in the total pressure drop in the duct as soon as the liquid started to accumulate and be propelled upwards (point *a* in Figure 5.8). Flooding as defined by Zapke did however only occur a little later when a sufficiently high vapor velocity was reached to carry the liquid up passed the liquid feed point (point *b* in Figure 5.8).

In the present investigation no pressure pulsation or transient phenomena were observed prior to flooding. However, as indicated in Figure 5.9 the pressure drop in the elliptical tube during flooding tended to be of a transient nature with pressure pulses clearly visible. Referring to Figure 5.8 and according to the definition used for flooding in the present investigation, the flooding velocity would be considered the velocity at point *a*, since it is at this point that a sharp increase in the pressure drop in the duct occurs. The transient nature of the pressure drop during flooding would then coincide with region *c-b* in Figure 5.8.

Since the vapor velocity was gradually increased in the time period depicted in Figure 5.8, it can be expected that the vapor velocity at point *a* is slightly lower than the velocity at point *b*. According to Zapke the percentage difference was normally not more than 5%. It can therefore be expected that the flooding velocity predicted by Zapke [97ZA2] will be approximately 3 to 5% higher than the flooding velocity determined in the present investigation. Referring to Figure 5.7, it can be seen that most of the data obtained in this investigation does lie slightly below the flooding correlation.

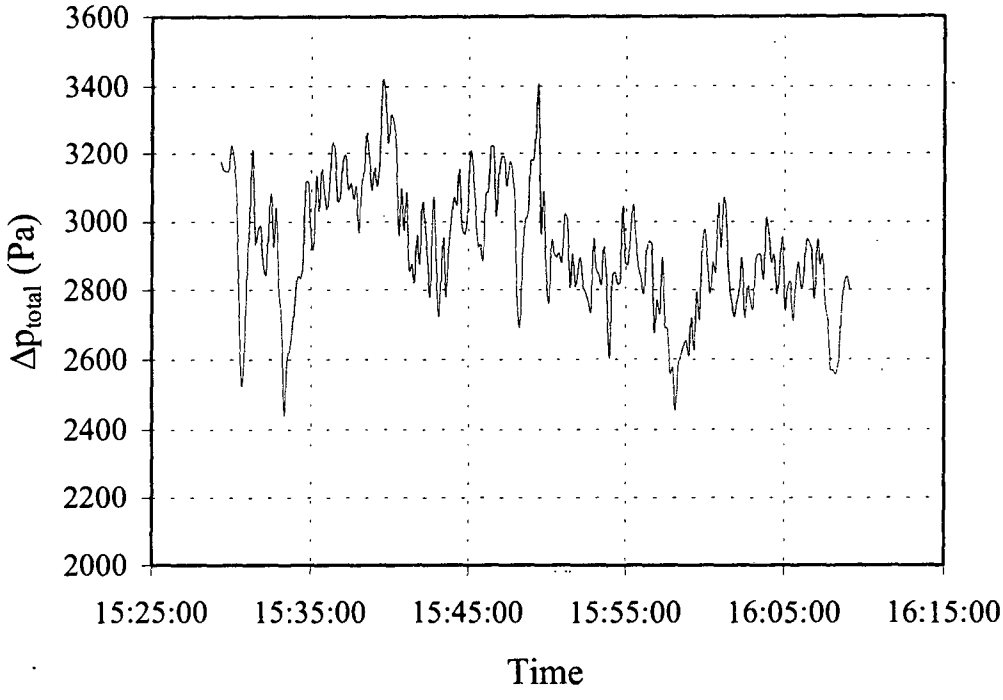

Figure 5.9: Transient pressure drop data inside the elliptical finned tube during flooding.

Numerous researchers [83BA1, 92GI1, 94OB1, 96RE1] have suggested that flooding determines the maximum heat transfer in a tube in which all the steam condenses in the reflux mode. Since the superficial vapor velocity at the tube entrance is indirectly representative of the heat transfer rate, it is useful to express the flooding data in terms of the flooding velocity. Upon rearranging equation (5.2), the predicted flooding velocity at the tube entrance can be expressed as

$$v_{sv} = 0.70367\left[(\rho_l - \rho_v)\, g\, H\left(1 - 27.7615 \times Fr_{dsl}^{0.6} / Zk_{d_h}^{0.2}\right)/\rho_v\right]^{0.5} \qquad (5.3)$$

where H is the duct height for an elliptical tube, or the diameter for a round tube. The right hand side of equation (5.3) is dependent on the fluid properties, which are temperature dependent. It is therefore possible to express the flooding vapor velocities in terms of the steam temperatures. This has been done graphically in Figure 5.7 where equation (5.3) is compared to experimentally determined flooding vapor velocities obtained in this investigation for the elliptical tube as well as for the 30 mm tube used by Reuter and Kröger [96RE1].

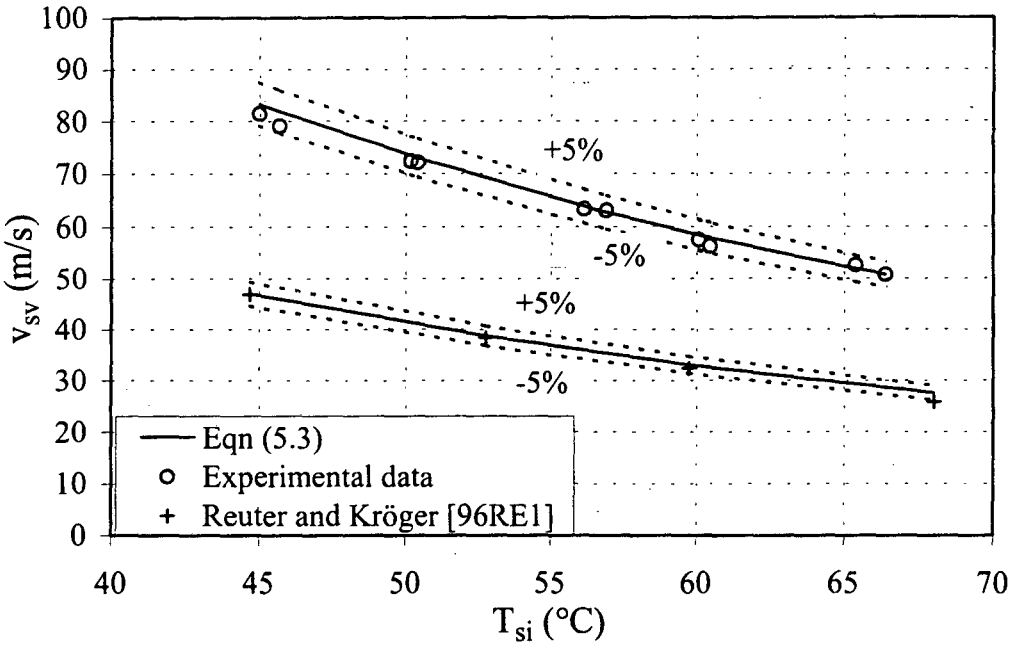

Figure 5.10: The flooding vapor velocity at the tube entrance as a function of steam temperature.

5.3. The heat transfer rate of the dephlegmator tube

The airside heat transfer rate of the dephlegmator tube is calculated using the measured air inlet and outlet temperatures and the air mass flow rate over the tube. To verify the accuracy of the airside heat transfer rate, the steamside heat transfer rate calculated using the condensate mass flow rate is compared to it. These values have been plotted against each other in Figure 5.11 for various steam temperatures.

At low heat transfer rates it was found that the steamside heat transfer was slightly higher than the airside value, while at higher heat transfer values, the airside heat transfer rate was slightly greater than the steamside value. It was assumed that at the low heat transfer rates, the steamside value was more accurate since in this region the condensate mass flow rate was slow and could be measured accurately. The potential for measurement errors by the anemometers in this region is greater due to the low air flow rates. At high heat transfer rates, it is more difficult to measure the condensate mass flow rate, and since the anemometers are probably more accurate at higher air flow rates, the airside heat transfer rate was considered more accurate in this region.

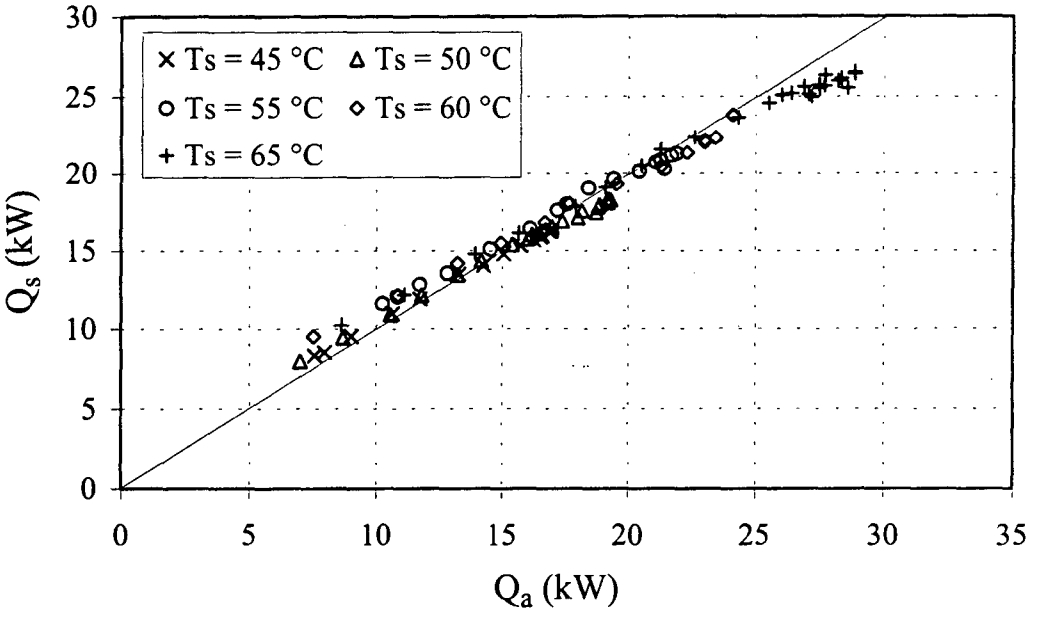

Figure 5.11: The measured airside heat transfer rate versus the measured steamside heat transfer rate.

Irrespective of the steam temperature, it was found that the heat transfer rate increased as the air mass flow over the dephlegmator tube was increased, but only until flooding occurred in the tube. Once flooding occurred, the heat transfer rate remained constant, or even decreased slightly with an increase in the air mass flow rate. This phenomenon seems to support the statement made by certain researchers [83BA1, 92GI1, 94OB1, 96RE1] that flooding determines the maximum heat transfer rate in a tube in which all the steam condenses in the reflux mode.

The heat transfer rate of the dephlegmator tube can also be predicted using the air inlet temperature and the air mass flow rate, as described in Chapter 3. In calculating the heat transfer rate, the effect of flooding on the thermal efficiency of the tube is not taken into account. The predicted heat transfer rate can therefore be considered the heat transfer rate under ideal conditions, i.e. flooding does not take place irrespective of the heat transfer rate. The superficial vapor velocity at the tube entrance under ideal conditions is then

$$v_{sv-ideal} = Q_{ideal} / (i_{fg} \rho_v A_{ct}) \tag{5.4}$$

which can then be used to calculate the vapor Froude number under ideal conditions. In Figure 5.12 the ideal heat transfer rate calculated assuming that flooding does not occur is plotted versus the corresponding ideal vapor Froude number. To demonstrate the effect that flooding has on the thermal effectiveness of a reflux condenser the measured heat transfer rate is also plotted versus the ideal Froude number.

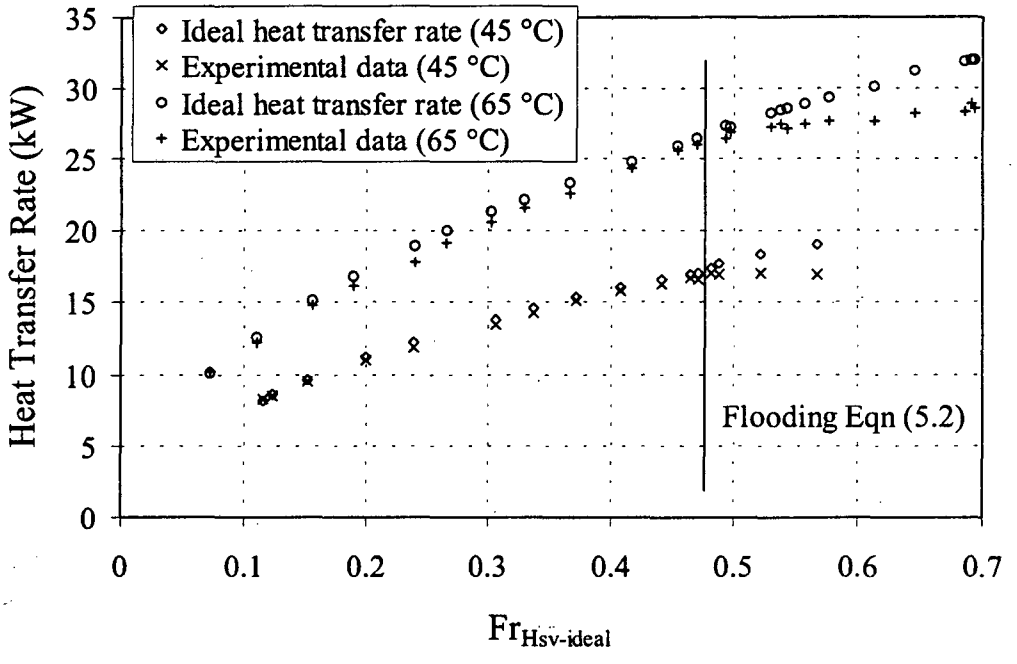

Figure 5.12: The ideal and experimental heat transfer rates plotted versus the vapor Froude number corresponding to the ideal heat transfer rate.

Figure 5.12 clearly shows the effect that flooding has on the heat transfer rate of an air-cooled reflux condenser tube. When flooding occurs in the elliptical tube, the thermal effectiveness thereof decreases, i.e. the actual heat transfer rate is lower than the heat transfer rate under ideal conditions.

5.4. The effect of a backflow region on the performance of the dephlegmator tube

In Chapter 3 mention was made of the negative effect that the accumulation of non-condensable gases has on the performance of a dephlegmator tube. Non-condensables tend to accumulate if a backflow region is present in the tube. Tests were performed to

study the effect of the presence of a backflow region in the dephlegmator tube used in this investigation. A backflow region in the dephlegmator tube was obtained by supplying steam via the steam by-pass pipe to the outlet header. The steam flow rate in the by-pass pipe was controlled by means of a ball valve. Unfortunately the steam flow rate in the by-pass pipe could not be determined accurately since a certain amount of reflux condensation took place inside the by-pass pipe which resulted in a fluctuating pressure drop inside the tube. The tests were therefore only of a qualitative nature.

In order to demonstrate the effect of the formation of a backflow region, a transient test was performed. The system was allowed to stabilise, and once this had happened, the ball valve in the steam by-pass pipe was then opened and steam allowed to flow to the outlet header. After a certain period the ball valve was closed again. During the entire run, experimental readings were taken at predetermined fixed intervals. Figure 5.13 shows the results of such a test performed over a 50-minute period for a steam temperature of 50 °C. The valve was opened at approximately 17:50 and closed again at 18:14. Note that flooding (evident from the high pressure drop) occurred in the tube prior to the valve being opened.

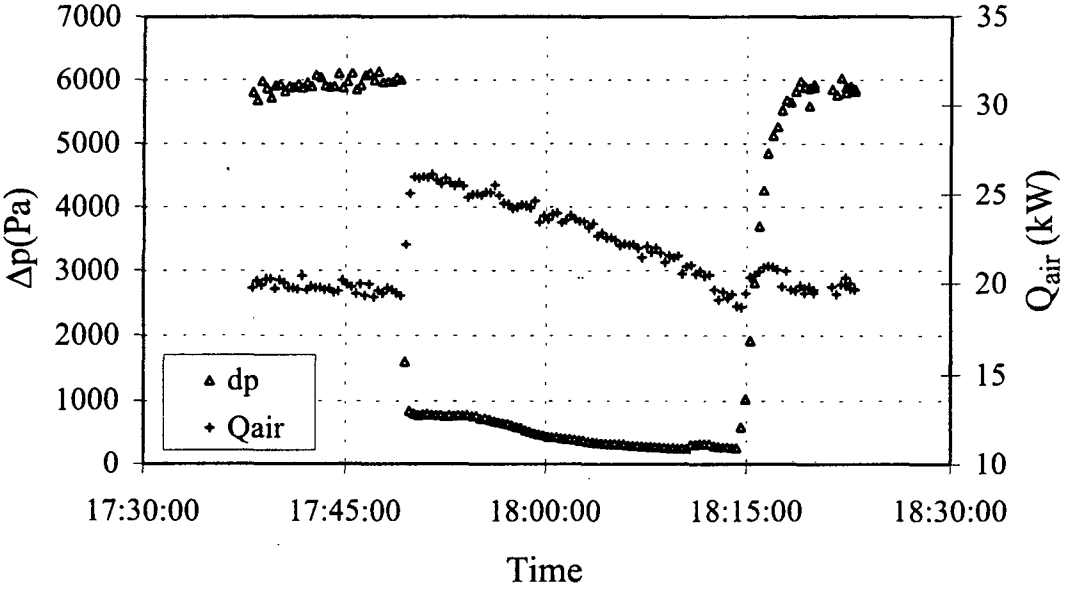

Figure 5.13: A transient analysis of the effect of the formation of a backflow region on the dephlegmator tube for a steam temperature of 50 °C.

Consider the pressure drop in the tube. As was mentioned above, it is clear from the high pressure drop that the tube was initially flooded. When the ball valve was opened at 17:50, the high pressure difference across the by-pass pipe caused a large amount of vapor to flow through it to the outlet header. This resulted in the pressure drop decreasing drastically thereby allowing the entrained liquid to drain out of the dephlegmator tube. Reflux condensation became the dominant flow mode in the major part of the tube. As the dephlegmator tube started to fill with non-condensable gases which were being trapped between the vapor flowing up the dephlegmator tube and the vapor flowing via the by-pass pipe, the header-to-header pressure drop started to decrease gradually. The decreasing pressure drop was a direct result of less vapor being condensed in the tube due to the continued accumulation of non-condensable gases. When the ball valve in the by-pass pipe was closed again at 18:14, the non-condensables were removed via the outlet header by the vacuum pump and the system reverted back to its initial flooded state.

A similar effect of the accumulation on non-condensable gases can be observed on the heat transfer performance of the dephlegmator tube. Initially while the tube was flooded, the heat transfer rate was relatively stable. However, as soon as the valve was opened, the entire tube was filled with vapor whose properties were the same as those of the vapor at the tube inlet. In other words, the temperature of the vapor in the entire tube was relatively high. As a result thereof the heat transfer rate increased dramatically. Non-condensable gases then started to accumulate in the tube, resulting in the formation of a dead zone. As the size of the dead zone grew, the heat transfer rate decreased. This decrease in the heat transfer rate continued until the ball valve was closed and all the non-condensables removed. The heat transfer rate then reverted back to its initial value.

The formation and increased growth of the dead zone in the dephlegmator tube can be seen in Figure 5.14. It is a plot of the air outlet temperatures over the length of the tube at various time intervals during the experimental run mentioned above. Initially the tube was flooded and since most of the entrained liquid was in the lower half of the tube, the air outlet temperature was slightly lower in this region as compared to the rest of the tube. When the valve was opened, all the liquid drained from the tube and the tube filled with high temperature vapor.

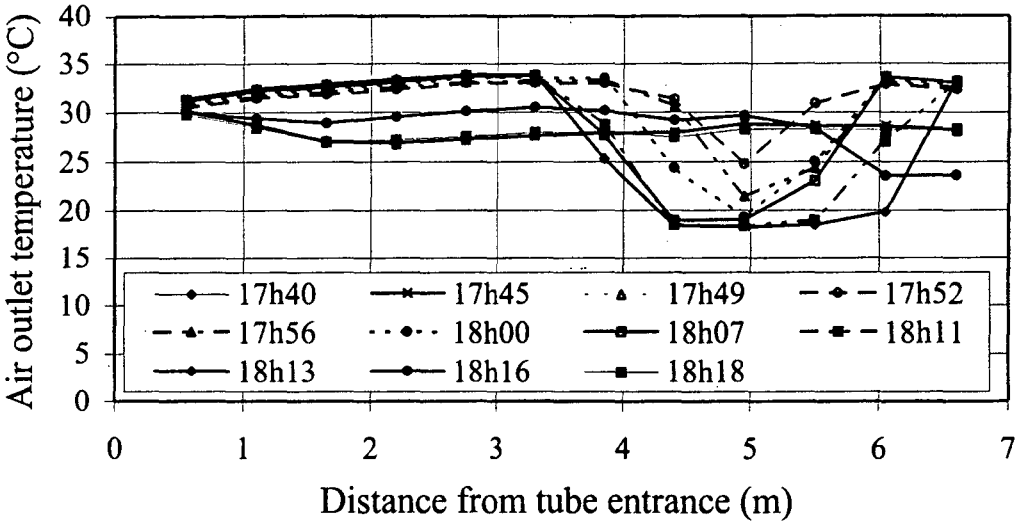

Figure 5.14: The air outlet temperatures along the length of the dephlegmator tube measured at certain times during a transient test wherein the ball valve in the by-pass pipe was opened and closed.

The majority of the vapor flowed up the tube, but a certain amount flowed via the by-pass pipe to the top of the tube. At the vapor interface between the up and down flowing vapor, non-condensable gases started to accumulate, resulting in a lower air outlet temperature at this point. As more non-condensable gases accumulated the size of the dead zone increased, evident from the lower air outlet temperatures in that region. When the ball valve in the by-pass pipe was closed again, the non-condensables began to move up the tube and were removed at the outlet header. The air outlet temperature at the top of the tube therefore decreased at this stage. Once all the non-condensable gases had been removed, the air outlet temperature assumed its initial profile.

CHAPTER 6
CONCLUSIONS AND RECOMMENDATIONS

In this investigation the header-to-header pressure drop and the occurrence of flooding inside a dephlegmator tube, as well as the heat transfer performance thereof were considered. A qualitative study on the effect of a backflow region was also conducted. An experimental rig consisting basically of an inclined air-cooled elliptical finned tube with a sharp-edged inlet in which steam ranging in temperature from 45 °C to 65 °C was condensed in the reflux mode, was used in this investigation.

It was found that in the experiments conducted the vapor flow rate at the entrance to the elliptical tube was in what Zapke and Kröger [96ZA3] would consider the moderate to high vapor flow rate range. The corresponding header-to-header pressure drop in the tube was predominantly dependent upon the superficial vapor Froude number. This is in agreement with the adiabatic two-phase pressure drop results obtained by Zapke and Kröger [96ZA3] for vapor flow in the moderate to high flow rate range.

The experimental results showed that the Zapke-Kröger pressure drop model, which models the header-to-header pressure drop as a function of both the vapor Reynolds and Froude numbers yields accurate results for the tube header-to-header pressure drop in the range $0.1 \leq Fr_{Hsv} \leq 0.4$. Above $Fr_{Hsv} \geq 0.4$ the actual pressure drop was slightly greater than the predicted pressure drop. The lack in accuracy of the model in this region can probably be attributed to the correlation used for the two-phase friction factor, which does not take into account the increase in the friction factor for $Fr_{Hsv} \geq 0.4$. Note that although the applicable range of the pressure drop model is expressed in terms of the vapor Froude number, it is probably more appropriate to express the predicted data in dimensional form in terms of the superficial vapor velocity.

The major drawback of the Zapke-Kröger pressure drop model is the fact that it makes use of correlations for the two-phase friction factor inside the tube and the two-phase contraction loss coefficient. These correlations are dependent on the cross-sectional geometry of the tube and are determined experimentally. Therefore, before the pressure drop model can be applied to a particular tube, the relevant adiabatic two-phase

experiments need to have been conducted in order to determine the above-mentioned correlations for that tube. This investigation has shown that this method is effective for reflux condensation in an elliptical tube. It is however recommended that tests similar to those conducted in this investigation be performed using other tube geometries to fully determine to what extent the Zapke-Kröger pressure drop model can be used and whether it yields accurate results when applied to for example round tubes.

As is the case for adiabatic two-phase countercurrent flow, flooding in a dephlegmator tube is governed by the superficial densimetric vapor Froude number with the duct height taken as the characteristic dimension. It was found that the flooding correlation that was proposed by Zapke [97ZA2] could be further simplified for flow in a dephlegmator tube and the simplified correlation predicts the flooding vapor Froude number to within ± 10%. Since the flow in a dephlegmator tube is such that there is a direct relationship between the vapor and liquid Froude numbers at the tube entrance, the above-mentioned correlation can be rearranged and expressed in terms of the vapor velocity. In that form the vapor velocity is then basically a function of the fluid properties which are temperature dependent. It is therefore possible to graphically express the vapor velocity as a function of steam temperature, and if this is done, the simplified Zapke flooding correlation predicts the flooding vapor velocity to within ± 5%.

It is important to note that the range of the flooding data obtained in this investigation constituted a very small portion of the range of the flooding data that Zapke [97ZA2] used to develop his flooding correlation. In the range tested, which is also the normal operating range of an industrial dephlegmator, Zapke's correlation predicts the flooding velocities during reflux condensation well. However, it is unsure whether the correlation is still accurate for higher liquid or vapor velocities during a heat transfer process. It is therefore recommended that further tests be conducted to increase the flooding data range. This can be done by firstly making use of an aftercondenser, which will increase the inlet vapor velocity without increasing the liquid velocity. Secondly, liquid can be supplied to the top of the tube. Note that these two methods have the added advantage of eliminating the direct relationship that exists between the vapor and liquid velocities at the tube entrance during reflux condensation.

It is useful to express the flooding data in terms of the vapor velocity since the vapor velocity is representative of the heat transfer rate. The experimental results of this investigation also proved that flooding has a limiting effect on the heat transfer rate in a dephlegmator tube in which all the steam condenses in the reflux mode. When flooding occurs the efficiency of the dephlegmator tube decreases significantly, resulting in no increase of the heat transfer rate for an increase in the air mass flow rate over the tube.

The effect of the presence of a backflow region on the performance of a dephlegmator tube was also highlighted by this investigation. The results showed that if there were no non-condensable gases in the system a backflow region would result in a much higher heat transfer rate than could normally be achieved. However, in most systems, and as was also the case for the experimental rig used in this investigation, non-condensable gases tend to leak into the system. These gases collect at the interface between the upward and downward flowing vapor in the dephlegmator tube. This results in the formation of a dead zone that increases gradually as more and more gases accumulate. As the dead zones increases in size, the heat transfer rate of the tube decreases.

REFERENCES

00KL1 Kliemann,S., Dry Cooling Towers, VDI-Berichte, no.236, pp. 229-238.

50KA1 Kays, W.M., Loss Coefficients for Abrupt Changes in Flow Cross Section with Low Reynolds Number Flow in Single and Multiple-Tube Systems, Trans. ASME, Vol. 72, no. 8, pp. 1067-1074, 1950.

63EN1 English, K.G., Jones, W.T., Spillers, R.C. and Orr, V., Flooding in a Vertical Updraft Partial Condenser, Chemical Engineering Progress, Vol. 59, No. 7, 1963.

69DI1 Diehl, J.E. and Koppany, C.R., Flooding Velocity Correlation for Gas-Liquid Countercurrent Flow in Vertical Tubes, Chemical Engineering Symposium Series, Vol. 65, No. 92, pp. 77-83, 1969.

71HE1 Heeren, H. and Holly, L., Dry Cooling Eliminates Thermal Pollution, Energie, Vol. 23, October and November, 1971.

72CO1 Collier, J.G., Convective Boiling and Condensation, McGraw-Hill Book Company, New York, 1972.

72RO1 Rossie, J.P. and Beck, R.W., Dry Cooling Towers, Energy Production and Thermal Effects, pp. 99-112, 1972.

72SH1 Shirazi, M.A., Dry Cooling for Steam Electric Power Plants in Arid Regions, Water Research, Vol. 6, pp. 1309-1319, 172.

73AG1 Agrawal, S.S., Gregory, G.A. and Govier, G.W., An Analysis of Horizontal Stratified Flow in Pipes, The Canadian Journal of Chemical Engineering, Vol. 51, pp. 280-286, June, 1973.

75HA1 Harris, P.J., Wilkes, B.T. and Coulthard, L.M.F., The Application of Dry Cooling Systems in Power Generation, BHRA Fluid Engineering, Cranfield, England, 1975.

75TO1 Tong, L.S., Boiling Heat Transfer and Two-Phase Flow, R.E. Krieger Publ. Co., New York, 1975.

76TA1 Taitel, Y. and Dukler, A.E., A Model for Predicting Flow Regime Transitions in Horizontal and Near Horizontal Gas-Liquid Flow, AIChE Journal, Vol. 22, No. 1, pp. 46-55, 1976.

77BU1 Butterworth, D. and Hewitt, G.F., Two-Phase Flow and Heat Transfer, Oxford University Press, Oxford, 1977.

77SU1 Surface, M.O., System Designs for Dry Cooling Towers, Power Engineering, September 1977.

79CH1 Cheremisinoff, N.P. and Davis, E.J., Stratified Turbulent-Turbulent Gas-Liquid Flow, AIChE Journal, Vol. 25, No.1, pp. 48-56, 1979.

80BE1 Berg, W.F. and Berg, J.L., Flow Patterns for Isothermal Condensation in One-Pass Air-Cooled Heat Exchangers, Heat Transfer Engineering, Vol. 1, no.4, pp. 21-31, 1980.

80CH1 Chung, K.S., Liu, C.P. and Tien, C.L., Flooding in Two-Phase Countercurrent Flow – II. Experimental Investigation, PhysicoChemical Hydrodynamics, Vol. 1, pp. 209-220, 1980.

80RU1 Russell, C.M.B., Condensation of Steam in a Long Reflux Tube, Heat Transfer and Fluid Flow Service, AERE Harwell and National Engineering Laboratory, July 1980.

81RI1 Richter, H.O., Flooding in Tubes and Annuli, International Journal of Multiphase Flow, Vol. 7, no. 4, pp. 674-658, 1981.

82BL1 Blangetti, F., Krebs, R. and Schlunder, E.U., Condensation in Vertical Tubes - Experimental Results and Modelling, Chemical Engineering Fundamentals, Vol. 2, No. 2, pp. 20-43, 1982.

82BR1 Breber, G., Palen, J.W. and Taborek, J., Study on Non-condensable Vapor Accumulation in Air-Cooled Condensers, Proc. 7th International Heat Transfer Conf., Vol. 6, pp. 263-268, 1982.

82HE1 Hewitt, G.F., Liquid-Gas Systems, in Handbook of Multiphase Systems, ed. Hetsroni, G., Chapters 2.1 - 2.3, 1982.

83BA1 Banerjee, S., Chang, J.S., Girard, R. and Krishnan, V.S., Reflux Condensation and Transition to Natural Circulation in a Vertical U-Tube, Journal of Heat Transfer, Vol. 105, pp. 717-727, November, 1983.

85TH1 Thies Clima Mercury Station Instruction Manual, 1985.

86BA1 Bankoff, S.G. and Lee, S.C., A Critical Review of the Flooding Literature, Multiphase Science and Technology, Chapter 2, pp. 95-180, ed. Hewitt, G.F., Hemisphere Publishing Corp., New York, 1986.

86KR1 Kröger, D.G., Performance Characteristics of Industrial Finned Tubes Presented in Dimensional Form, International Journal of Heat Mass Transfer, Vol. 29, no. 8, pp. 1119-1125, 1986.

87WH1 Whalley, P.B., Boiling, Condensation and Gas-Liquid Flow, Claredon Press, Oxford, 1987.

89FU1 Fürst, J., Kondensation in geneigten ovalen Rohren, Fortschrittberichte VDI, Reihe 19, Nr. 36, VDI Verlag, Düsseldorf, 1989.

89KR1 Kröger, D.G., Cooling Tower Performance and Design Class Notes, Dept. of Mechanical Engineering, University of Stellenbosch, South Africa, 1989.

89TA1 Tapucu, A., Teyssedou, N., Troche, N. and Merilo, M., Pressure Losses Caused by Area Changes in a Single-Channel Flow under Two-Phase Flow Conditions, International Journal of Multiphase Flow, Vol. 15, no. 1, pp. 51-64, 1989.

90FU1 Funnell, R.C., Prediction of Flow Patterns and Pressure Gradient in Inclined Two-Phase Flow Systems, M.Eng Thesis, University of Stellenbosch, South Africa, 1990.

91GO1 Govan, A.H., Hewitt, G.F., Richter, H.J. and Scott, A., Flooding and Churn Flow on Vertical Pipes, International Journal of Multiphase Flow, Vol. 17, No. 1, pp. 27-44, 1991.

90ID1 Ide, H. and Matsumura, H., Frictional Pressure Drops of Two-Phase Gas-Liquid Flow in Rectangular Channels, Experimental Thermal and Fluid Science, Vol. 3, pp. 362-372, 1990.

91BE1 Bellstedt, M.O., Condensation of Low-Pressure Steam in Inclined Air-Cooled Tubes, Ph.D. Thesis, University of Stellenbosch, South Africa, 1991.

92CA1 Carey, Van P., Liquid-Vapor Phase-Change Phenomena, Hemisphere Publishing Corporation, Washington, 1992.

92GI1 Girard, R. and Chang, J.S., Reflux Condensation Phenomena in Single Vertical Tubes, International Journal of Heat Mass Transfer, Vol. 35, No. 9, pp. 2203-2218, 1992.

93GR1 Groenewald, W., Heat Transfer and Pressure Change in an Inclined Air-Cooled Flattened Tube during Condensation of Steam, M. Eng. Thesis, University of Stellenbosch, South Africa, 1993.

94OB1 Obinelo, I.F., Round, G.F. and Chang, J.S., Condensation Enhancement by Steam Pulsation in a Reflux Condenser, International Journal of heat and Fluid flow, Vol. 15, no.1, pp. 20-29, 1994.

94RE1 Reuter, H.C., Flow Modes and Pressure Change in an Inclined Tube during Reflux Condensation of Steam, M. Eng. Thesis, University of Stellenbosch, South Africa, 1994.

94ZA1 Zapke, A., Pressure Gradient and Flooding during Two-Phase Counter-current Flow in Tubes, M. Eng. Thesis, University of Stellenbosch, South Africa, 1994.

95ZA1 Zapke, A., Matimba Power Station Dephlegmator Investigation, Dept. of Mechanical Engineering, University of Stellenbosch, South Africa, 1995.

96RE1 Reuter, H.C., and Kröger, D.G., Pressure Change and Flooding in Vertical and Inclined Tubes during Reflux Condensation of Steam, 9th International Symposium on Transport Phenomena in Thermal – Fluids Engineering, Singapore, June 25-28, 1996.

96ZA1 Zapke, A. and Kröger, D.G., The Influence of Fluid Properties and Inlet Geometry on Flooding in Vertical and Inclined Tubes, International Journal of Multiphase Flow, Vol. 22, no. 3, pp. 461-472, 1996.

96ZA2 Zapke, A. and Kröger, D.G., The Effect of Fluid Properties on Flooding in Vertical and Inclined Rectangular Ducts and Tubes, ASME Fluids Engineering Division Conference, FED-Vol. 239, Vol. 4, pp. 527-532, 1996.

96ZA3 Zapke, A. and Kröger, D.G., Pressure Drop during Gas-Liquid Countercurrent Flow in Inclined Rectangular Ducts, 5th International Heat Pipe Symposium, Melbourne, 1996.

96ZI1 Zipfel, T., Steam Flow Distribution in Air-Cooled Condensers, M. Eng. Thesis, University of Stellenbosch, South Africa, 1996.

97SC1 Schmidt, J. and Friedel, L., Two-Phase Pressure Drop Across Sudden Contractions in Duct Areas, International Journal of Multiphase Flow, Vol. 23, no. 2, pp. 283-299, 1997.

97ZA1 Zapke, A. and Kröger, D.G., Vapor-Condensate Interactions during Counterflow in Inclined Reflux Condensers, ASME National Heat Transfer Conference, HTD-Vol. 342, Vol. 4, pp. 157-162, 1997.

97ZA2 Zapke, A., The Characteristics of Gas-Liquid Counterflow in Inclined Ducts with Particular Reference to Reflux Condensers, Ph.D. Thesis, University of Stellenbosch, South Africa, 1997.

APPENDIX A

APPLICATION OF THE ZAPKE-KRÖGER PRESSURE DROP MODEL TO TWO TUBES OF A DOUBLE ROW DEPHLEGMATOR

Two tubes of an air-cooled dephlegmator are schematically depicted in Figure A.1. Since the bottom tube is in contact with cooler air than the top tube, the fin pitch of the bottom tube is often greater than that of the top tube so as to ensure that each tube transfers approximately the same amount of heat. However, should the bottom tube transfer more heat, it will condense more steam than the top tube. Since the outlet of each tube is connected to the outlet header, which implies that the pressure drop over each tube must be the same, a certain amount of steam will flow from the top tube into the bottom tube, causing a backflow region in the bottom tube. The header-to-header pressure drop for this flow situation will now be considered using the model developed by [97ZA1].

In Figure A.1 the length of the region wherein the vapor flows in the positive z-direction in the bottom tube is denoted as L_a and position 5 is located at the front where the upward and the downward flowing vapor meet. Assuming again that the ejector suction rate is negligible, the condensate mass flow rate flowing out of each tube must equal the net inflow of vapor in each tube:

$$m_{c-1} = m_{v2-1} + m_{v3-1} \tag{A.1}$$

$$m_{c-2} = m_{v2-2} - m_{v3-2} \tag{A.2}$$

Furthermore, the vapor mass flow rate entering the top of tube 1 must equal the vapor mass flow rate exiting the top of tube 2:

$$m_{v3-1} = m_{v3-2} \tag{A.3}$$

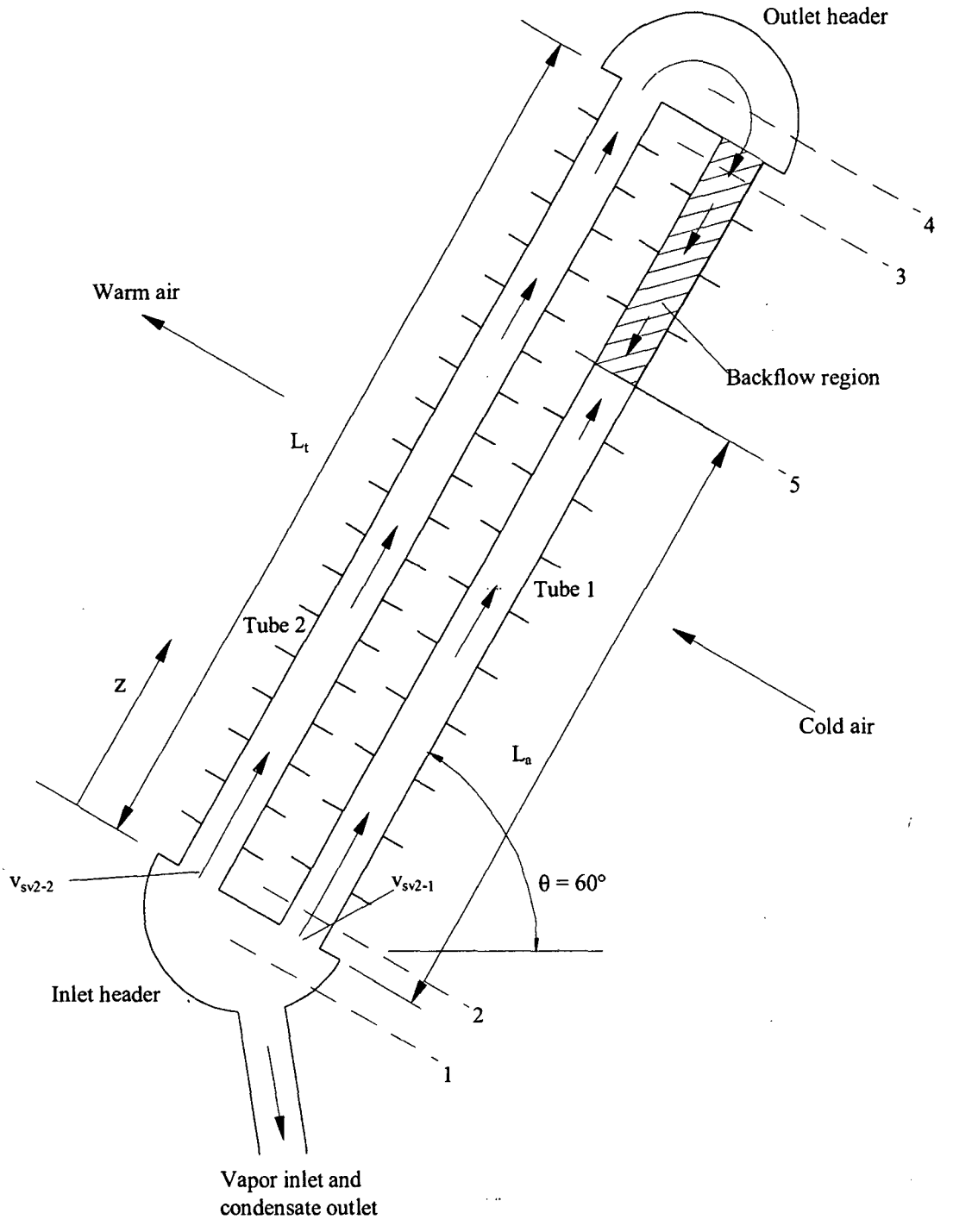

Figure A.1: A schematic of two tubes of a double row dephlegmator with a vapor backflow region in the bottom tube.

Considering the heat transfer to be a constant heat flux process, with the vapor condensing uniformly in each tube, it follows that

$$\frac{m_{v3-1}}{m_{c-1}} = \frac{(L_t - L_a)}{L_t} = 1 - \frac{L_a}{L_t} \tag{A.4}$$

and the vapor superficial velocity in each tube row expressed in terms of the superficial vapor velocity at each tube entrance is

$$v_{sv-1} = v_{sv2-1}(1 - z/L_a) \tag{A.5}$$

for tube 1 in the region where the vapor flow is in the positive z-direction, and for tube 2:

$$v_{sv-2} = v_{sv2-2}\left[1 - \frac{z}{L_t}\left(1 - \frac{v_{sv3-2}}{v_{sv2-2}}\right)\right] \tag{A.6}$$

The header-to-header pressure drop in tube 1 can be expressed as

$$\Delta p_{14-1} = \Delta p_{12-1} + \Delta p_{25-1} + \Delta p_{53-1} + \Delta p_{34-1} \tag{A.7}$$

The pressure drop in tube 1 between position 1 and position 5 can be calculated using the equations derived for the single row dephlegmator, i.e. equations (2.57) and (2.60) to (2.62). In these equations, L_t must however be replaced with L_a. The pressure change in the backflow region, where the vapor and the condensate flow cocurrently down the tube may also be calculated in this way. Note that only vapor flows into the top of the tube 1 from tube 2. The pressure change in tube 1 due to the inflowing vapor at the top of the tube may therefore be calculated using a single-phase contraction loss coefficient as follows:

$$\Delta p_{34-1} = -\frac{1}{2}\rho_v v_{sv3-1}^2\left[1 - \sigma_{34}^2 + K_{c,SP}\right] \tag{A.8}$$

where $K_{c,SP}$ is calculated from equation (2.41). The total header-to-header pressure drop in tube 1 is then given by

$$\begin{aligned}\Delta p_{14-1} = {} & \frac{1}{2}\rho_{v-1}v_{sv2-1}^2\left[\left(K_{TP}-\sigma_{21}^2\right)+\frac{L_a}{d_h}K_f\,Re_{sv2-1}^{n_f}\left(\frac{a_n}{n_f+3}+\frac{b_n}{(n_f+2)Re_{sv2-1}}\right)\right] \\ & -\frac{1}{2}\rho_{v-1}v_{sv3-1}^2\left[\left(1-\sigma_{34}^2+K_{c,SP}\right)\right] \\ & -\frac{1}{2}\rho_{v-1}v_{sv3-1}^2\left[\frac{(L_t-L_a)}{d_h}K_f\,Re_{sv3-1}^{n_f}\left(\frac{a_n}{(n_f+3)}+\frac{b_n}{(n_f+2)Re_{sv3-1}}\right)\right] \\ & -\left(\rho_{v-1}v_{sv2-1}^2-\rho_{v-1}v_{sv3-1}^2\right)+\rho_{v-1}g\,L_t\sin(\theta)\end{aligned} \tag{A.9}$$

The header-to-header pressure drop in tube 2 can be expressed symbolically using equation (2.2). However, unlike a single tube, the pressure change at the tube outlet, Δp_{34-2} is not negligible since there is a net outflow of vapor from the top of the tube. The pressure change due to the expansion must therefore be calculated using a single-phase expansion loss coefficient:

$$\Delta p_{34-2} = \frac{1}{2}\rho_{v-2}v_{sv3-2}^2\left[1-\sigma_{34}^2+K_{e,SP}\right] \tag{A.10}$$

and according to Kays [50KA1]:

$$K_{e,SP} = \left(1-\sigma_{34}\right)^2 \tag{A.11}$$

To calculate the pressure drop in row 2, substitute equation (A.6) into the terms on the right hand side of equation (2.58) and integrate over the length of the tube. The total header-to-header pressure drop in tube 2 is then

$$\begin{aligned}\Delta p_{14-2} = {} & \frac{1}{2}\rho_{v-2}v_{sv2-2}^2\left[\frac{L_t}{d_h}\frac{K_f\,Re_{sv2-2}^{n_f}}{\left(1-\frac{v_{sv3-2}}{v_{sv2-2}}\right)}\left(\frac{a_n\left(1-\left(\frac{v_{sv3-2}}{v_{sv2-2}}\right)^{n_f+3}\right)}{n_f+3}+\frac{b_n\left(1-\left(\frac{v_{sv3-2}}{v_{sv2-2}}\right)^{n_f+2}\right)}{(n_f+2)Re_{sv2-2}}\right)\right] \\ & +\frac{1}{2}\rho_{v-2}v_{sv2-2}^2\left(K_{TP}-\sigma_{21}^2\right)+\frac{1}{2}\rho_{v-2}v_{sv3-2}^2\left(\sigma_{34}^2-1+K_{e,SP}\right) \\ & -\left(\rho_{v-2}v_{sv2-2}^2-\rho_{v-2}v_{sv3-2}^2\right)+\rho_{v-2}g\,L_t\sin(\theta)\end{aligned} \tag{A.12}$$

Finally, since both tubes are connected to a common outlet header, the pressure difference across each tube must be the same

$$\Delta p_{14-1} = \Delta p_{14-2} \tag{A.13}$$

In the system of equations derived for the header-to-header pressure drop in the two tubes, there are 5 unknowns namely L_a, $v_{sv2\text{-}1}$, $v_{sv3\text{-}1}$, $v_{sv2\text{-}2}$ and $v_{sv3\text{-}2}$. These may be determined by simultaneously solving equations (A.1) to (A.4) and (A.12).

APPENDIX B

HEAT TRANSFER, PRESSURE DROP AND FLOODING SAMPLE CALCULATION

The elliptical air-cooled finned tube used in this investigation has the following specifications:

Tube length,	L_t	= 7 m
Tube inside height,	H_t	= 0.097 m
Tube inside width	W_t	= 0.016 m
Tube cross sectional area,	A_{tc}	= 1330×10^{-6} m^2
Tube hydraulic diameter,	d_h	= 25.922×10^{-3} m
Tube inside perimeter,	P_{et}	= 205.2×10^{-3} m^2/m
Tube flange thickness,	t_{tf}	= 0.009 m
Effective tube length for heat transfer,	L_{et}	= $(L_t - 2 \times t_{tf}) = 7 - 0.018 = 6.982$ m
Tube frontal area,	A_{fr}	= $L_{et} \times W_{fin} = 6.982 \times 0.05$
		= 0.3491 m^2
Characteristic heat transfer	a_{Ny}	= 2594.951
parameter characteristics,	b_{Ny}	= 0.3184

B.1. Measured and processed heat transfer and pressure drop data

For the purpose of this sample calculation, the experimental data from Reading 6 obtained for a steam temperature of approximately 45 °C will be used. The experimental data for the entire experimental run is tabulated in Appendix E. For Reading 6 the applicable data is as follows:

Ambient pressure,	p_{amb}	= 100359 Pa
Steam inlet temperature,	T_{si}	= 44.98 °C
Steam outlet temperature,	T_{so}	= 43.85 °C
Pressure drop across headers,	Δp	= 564.86 Pa
Condensate mass flow rate,	m_c	= 5.63×10^{-3} kg/s
Gravitational constant,	g	= 9.7962 m²/s

As was mentioned in Chapter 4, the air outlet duct mounted on top of the wooden casing in which the tube is situated is divided into 4 sections. The air inlet and outlet temperatures as well as the air volume flow rate over each corresponding section of the tube have been tabulated below.

Table B.1: The air temperatures and volume flow rates over each section of the elliptical finned tube.

	Air inlet temperature T_{ai} (°C)	Air outlet temperature T_{ao} (°C)	Air volume flow rate V_a (m³/s)
Section 1	18.07	35.24	0.162
Section 2	17.5	34.79	0.170
Section 3	17.28	34.52	0.173
Section 4	17.01	33.93	0.171
Average	17.47	34.62	-------

The steamside heat transfer rate is calculated using the average steam temperature on the inside of the tube, $T_{sm} = (T_{si} + T_{so})/2 = (44.98 + 43.85)/2 = 44.42\ °C = 317.57\ K$. At this temperature the latent heat of vaporization from equation (D.2.6) is

$$i_{fg} = 3.4831814\times10^{6} - 5.8627703\times10^{3}\times317.57 + 1.2139568\times10\times317.57^{2} - 1.40290431\times10^{-2}\times317.57^{3} = 2396327.0\ J/kg$$

The total steam side heat transfer, $Q_s = m_{sc} \times i_{fg} = 0.00563 \times 2396327.0 = 13491.3$ W.

The airside calculations will be done in detail for section 2 only. However, the processed data for all four sections have been tabulated below since they are necessary for subsequent calculations. The mean air temperature flowing through section 2, $T_{am2} = (T_{ai2} + T_{ao2}) / 2 = (17.50 + 34.79) / 2 = 26.15\ °C = 299.30\ K$. At this temperature the specific heat of the air is given by equation (D.3.2):

$$c_{pa} = 1.045356\times10^{3} - 3.161783\times10^{-1}\times299.30 + 7.083814\times10^{-4}\times299.30^{2} - 2.705209\times10^{-7}\times299.30^{3} = 1006.93\ J/kgK$$

The air volume flow rate is measured on the downstream side of the tube. Therefore, at the air outlet temperature, T_{ao2} = 34.79 °C = 307.94 K and at the ambient pressure, p_{amb} = 100359 Pa, the air density is given by equation (D.3.1):

$$\rho_{ao2} = 100359/(287.08 \times 307.94) = 1.135\ \text{kg/m}^3$$

Note that although there is a pressure drop over the tube, this pressure drop is never greater than 500 Pa. Therefore by approximating the air outlet pressure as the ambient pressure a maximum error of 0.5 % is made. The air mass flow rate over section 2 is

$$m_{a2} = \rho_{ao2} \times V_{a2} = 1.135 \times 0.170 = 0.1930\ \text{kg/s}.$$

The airside heat transfer in section 2 is then

$$Q_{a2} = m_{a2} \times c_{pa2} \times (T_{ao2} - T_{ai2}) = 0.193 \times 1006.93 \times (34.79 - 17.50) = 3356\ \text{W}.$$

The measured heat transfer data for each section of the tube as calculated above are given in the table here below.

Table B.2: Summary of relevant experimental results over each section of the tube.

	T_{am} (°C)	c_{pa} (J/kgK)	ρ_{ao} (kg/m³)	m_a (kg/s)	Q_a (W)
Section 1	26.66	1006.95	1.1336	0.184	3175
Section 2	26.15	1006.93	1.1352	0.193	3356
Section 3	25.90	1006.92	1.1362	0.197	3413
Section 4	25.47	1006.90	1.1384	0.194	3310
Total	-	-	-	0.768	13255

An energy balance performed using both heat transfer values yields:

$$EB = (Q_{a_T} - Q_s)/Q_{a_T} \times 100\% = (13255 - 13490)/13255 \times 100 = -1.77\%$$

The vapor pressure difference between the inlet and outlet headers is calculated using the steam temperatures in the inlet and outlet headers. At the steam inlet temperature, $T_{si} = 44.98$ °C = 318.13 K, the corresponding vapor pressure is given by equation (D.1.1):

$$x = 273.16/318.13 = 0.8586$$

$$z = 10.79586\times(1-0.8586) + 5.028081\times\log_{10}(0.8586) + 1.50474\times10^{-4}\times[1-10^{-8.29692(1/0.8586-1)}] + 4.2873\times10^{-4}\times[10^{4.76955(1-0.8586)}-1] + 2.786118312 = 3.9811$$

$$p_{vi} = 10^{3.9811} = 9574.9 \text{ Pa}$$

Similarly the vapor pressure at the steam outlet temperature, p_{vo}= 9032.2 Pa. The difference in the vapor pressures between the headers is thus 542.7 Pa. This compares very favourably with the measured pressure drop of 564.86 Pa.

The superficial velocities at the tube entrance can be calculated using either the airside or the steamside heat transfer rate. As explained in Chapter 5, the greater of the two heat transfer values is used which in this case is the steamside heat transfer rate. The applicable thermophysical properties of the steam and condensate are evaluated at the inlet temperature. From equation (D.1.3) the density of the vapor is

$$\rho_v = -4.062329056 + 0.10277044\times318.13 - 9.76300388\times10^{-4}\times318.13^2 + 4.475240795\times10^{-6}\times318.13^3 - 1.004596894\times10^{-8}\times318.13^4 + 8.9154895\times10^{-12}\times318.13^5 = 0.0654 \text{ kg/m}^3$$

The density of the condensate is obtained from equation (D.2.1):

$$\rho_l = (1.49343\times10^{-3} - 3.7164\times10^{-6}\times318.13 + 7.09782\times10^{-9}\times318.13^2 - 1.90321\times10^{-20}\times318.13^6)^{-1} = 990.34 \text{ kg/m}^3$$

The dynamic viscosity of the vapor from equation (D.1.2):

$$\mu_v = 2.562435\times10^{-6} + 1.816683\times10^{-8}\times318.13 + 2.579066\times10^{-11}\times318.13^2 - 1.067299\times10^{-14}\times318.13^3 = 1.0608\times10^{-5}\ \text{kg/ms}$$

The superficial vapor velocity at the tube entrance is then

$$v_{sv} = \frac{Q_s}{\rho_v A_{tc} i_{fg}} = \frac{m_{sc}}{\rho_v A_{tc}} = \frac{5.63\times10^{-3}}{(0.0654\times1330\times10^{-6})} = 64.736\ \text{m/s}$$

The superficial vapor Reynolds number at the inlet is therefore

$$Re_{sv} = \rho_v v_{sv} d_H / \mu_v = 0.0654\times64.736\times25.922\times10^{-3} / 1.0608\times10^{-5} = 10344$$

and the superficial densimetric Froude number for the vapor at the tube inlet

$$Fr_{Hsv} = \frac{\rho_v v_{sv}^2}{(\rho_l - \rho_v) g H} = \frac{0.0654\times64.736^2}{(990.34-0.0654)\times9.7962\times0.097} = 0.2912$$

The measured dimensionless header-to-header pressure drop in the tube is

$$\Delta p / (0.5\rho_v v_{sv}^2) = 564.86 / (0.5\times0.0654\times64.736^2) = 4.123$$

B.2. The predicted header-to-header pressure drop

Using the Zapke-Kröger pressure drop model described in Chapter 2, the header-to-header pressure drop can also be predicted. The theoretical pressure drop is calculated at the mean steam temperature of the entire experimental run, i.e. T_{sm} = 44.97 °C = 318.12 K. This temperature is the same as the measured steam inlet temperature from Reading 6. The relevant fluid properties calculated above can therefore be used for the theoretical pressure drop calculations. In calculating the pressure drop, the superficial densimetric vapor Froude number is considered the independent variable from which the vapor velocity, vapor Reynolds number and all other applicable data are calculated.

The pressure drop is calculated in the range $0.05 \leq Fr_{Hsv} \leq 0.46$ and for the purpose of this sample calculation a value of 0.296 will be used.

The superficial vapor velocity corresponding to the vapor Froude number is

$$v_{sv} = [Fr_{Hsv}(\rho_l - \rho_v)g\,H/\rho_v]^{0.5} = [0.296 \times (990.34 - 0.0654) \times 9.7962 \times 0.097/0.0654]^{0.5}$$
$$= 65.265 \text{ m/s}$$

and the vapor Reynolds number is then

$$Re_{sv} = \rho_v v_{sv} d_h / \mu_v = 0.0654 \times 65.265 \times 25.922 \times 10^{-3} / 1.0608 \times 10^{-5} = 10428$$

The inlet pressure drop is given by equation (2.57). The inside cross-sectional area of the steam inlet header before the contraction, $A_{hc} = 0.015394$ m^2. The area contraction ratio is therefore

$$\sigma_{21} = A_{tc} / A_{hc} = 1330 \times 10^{-6} / 0.015394 = 0.0857$$

From equation (2.45) the two-phase contraction loss coefficient is

$$K_{TP} = 1.6502 \exp(1{:}0166 \times 0.296) = 2.230$$

and the two-phase inlet pressure drop is then

$$\Delta p_{12} = 0.5 \times 0.0654 \times 65.265^2 [2.230 - 0.0857] = 298.56 \text{ Pa}$$

The pressure drop in the tube due to friction is given by equation (2.60) where $K_f = 0.2259$ and $n_f = -0.2088$. To calculate the condensation enhancement factors, a_n and b_n, the suction vapor Reynolds number is needed, which is given as

$$Re_{vn} = \frac{m_c d_h}{\mu_v L_t P_{et}} = \frac{Re_{sv}\, A_{ct}}{L_t P_{et}} = \frac{10428 \times 1330 \times 10^{-6}}{6.982 \times 0.2052} = 9.680$$

From equation (2.32):

$$a_n = 1.0649 + 1.041\times10^{-3}\times9.680 - 2.011\times10^{-7}\times9.680^3 = 1.0745$$

and from equation (2.33):

$$b_n = 290.1479 + 59.3153\times9.680 - 1.5995\times10^{-2}\times9.680^3 = 849.812$$

The frictional component of the pressure drop is then

$$\Delta p_{f23} = 0.5\times0.0654\times65.265^2\times\left[\frac{7.00}{0.025922}\times0.2259\times10428^{-0.2088}\times\left(\frac{1.0745}{2.7912}+\frac{849.812}{1.7912\times10428}\right)\right] = 529.81\ \text{Pa}$$

The momentum component of the total pressure drop is given by equation (2.62) and is

$$\Delta p_{m23} = -0.0654\times65.265^2 = -278.53\ \text{Pa}$$

The gravitational component from equation (2.61):

$$\Delta p_{g23} = 0.0654\times9.7962\times7.00\times\sin(60°) = 3.883\ \text{Pa}$$

The total predicted header-to header pressure drop is thus

$$\Delta p_T = 298.56 + 529.81 - 278.53 + 3.883 = 553.72\ \text{Pa}$$

or in dimensionless form this can be expressed as

$$\Delta p_T / \left(0.5\rho_v v_{sv}^2\right) = 553.72 / \left(0.5\times0.0654\times65.265^2\right) = 3.976$$

B.3. Prediction of flooding

During the experimental run the steam was at a temperature of 44.99 °C = 318.14 K when flooding occurred in the tube. This temperature will be used to determine the flooding velocity as predicted by the linearized Zapke-Kröger flooding correlation, equation (5.2) where from equation (2.52):

$$K_{fl} = 7.9143\times10^{-2} + 4.9705\times10^{-3}\times60 + 1.5183\times10^{-4}\times60^2 - 1.9852\times10^{-6}\times60^3$$
$$= 0.49516$$

and from equation (2.53):

$$n_{fl} = 18.149 - 1.9471\times60 + 6.7058\times10^{-2}\times60^2 - 5.3227\times10^{-4}\times60^3 = 27.7615$$

for an inclination angle of 60°. Since the steam temperature at flooding is practically the same as the steam temperature used in the pressure drop calculations in the previous section, the thermophysical fluid properties as calculated in the previous section will be used. Further fluid properties necessary are the condensate dynamic viscosity, which from equation (D.2.2) is

$$\mu_l = 2.414\times10^{-5}\times10^{247.8/(318.14-140)} = 5.9399\times10^{-4}\,\text{kg/ms}$$

and the surface tension, which from equation (D.2.3) is

$$\sigma_l = 5.148103\times10^{-2} + 3.998714\times10^{-4}\times318.14 - 1.4721869\times10^{-6}\times318.14^2$$
$$+1.21405335\times10^{-9}\times318.14^3 = 0.06878\ \text{N/m}$$

From equation (2.49), it follows that

$$Zk_{d_h} = \sqrt{(990.34\times0.025922\times0.06878)}/\left(5.9399\times10^{-4}\right) = 2237.1$$

Since the relation, $\rho_l v_{sl} = \rho_v v_{sv}$ exists between the superficial vapor and condensate velocities at the tube entrance when all the steam is condensed in the tube during reflux condensation, the flooding superficial vapor velocity can be solved iteratively using equation (5.2) or (5.3). Assume that the flooding superficial vapor velocity, $v_{sv} = 83.273$ m/s. The superficial liquid velocity is therefore

$$v_{sl} = 83.273 \times 0.0654 / 990.34 = 5.499 \times 10^{-3} \text{ m/s}$$

and the superficial liquid Froude number with the hydraulic diameter taken as the characteristic dimension is then

$$Fr_{dsl} = 990.34 \times \left(5.499 \times 10^{-3}\right)^2 / \left((990.34 - 0.0654) \times 9.7962 \times 0.025922\right) = 1.1910 \times 10^{-4}$$

Solving for the vapor Froude number using equation (5.2), it follows that

$$Fr_{Hsv} = 0.49515 \times (1 - 27.7615 \times \left(1.1910 \times 10^{-4}\right)^{0.6} / 2237.1^{0.2}) = 0.48215$$

The corresponding vapor velocity is then

$$v_{sv} = \left(0.48215 \times (990.34 - 0.0654) \times 9.7962 \times 0.097 / 0.0654\right)^{0.5} = 83.297 \text{ m/s}$$

which differs by less than 0.1 % from the assumed vapor velocity.

B.4. The predicted heat transfer rate

As was done for the measured heat transfer data, a sample calculation of the predicted heat transfer rate will be done for section 2 only. The steam temperature decreases over the length of the tube and it is assumed that this decrease in temperature is linear. Note that this is not strictly correct, since the steam temperature varies according to the pressure in the tube. However, since the temperature drop is relatively small, no appreciable errors are made using the assumption above. The average steam temperature in section 2 at which the condensate fluid properties are evaluated is then

$$T_{sm2} = T_{si} + 0.375(T_{so} - T_{si}) = 44.98 + 0.375(43.85 - 44.98) = 44.56\ °C\ =\ 317.71\ K\ .$$

From equation (D.2.1), the density of the condensate is

$$\rho_l = (1.49343\times10^{-3} - 3.7164\times10^{-6}\times317.71 + 7.09782\times10^{-9}\times317.17^2 - 1.90321\times10^{-20}\times317.71^6)^{-1} = 990.52\ kg/m^3$$

The condensate dynamic viscosity from equation (D.2.2):

$$\mu_l = 2.414\times10^{-5}\times10^{247.8/(317.71-140)} = 5.9861\times10^{-4}\ kg/ms$$

and the thermal conductivity from equation (D.2.5):

$$k_l = -6.14255\times10^{-1} + 6.9962\times10^{-3}\times317.71 - 1.01075\times10^{-5}\times317.71^2 + 4.74737\times10^{-12}\times317.71^4 = 0.63663\ W/mK$$

From equation (D.2.6), the latent heat of vaporization:

$$i_{fg} = 3.4831814\times10^6 - 5.8627703\times10^3\times317.71 + 1.2139568\times10\times317.71^2 - 1.40290431\times10^{-2}\times317.71^3 = 2395979\ J/kg$$

The method employed in calculating the heat transfer rate has been described in Chapter 3. The heat transfer rate is solved iteratively, and therefore for the purpose of these calculations assume an air outlet temperature of 35.41 °C = 308.56 K.

The thermophysical properties of the air flowing over the finned tube are evaluated at the mean air temperature, i.e.

$$T_{am2} = (T_{ai2} + T_{ao2})/2\ =\ (17.50 + 35.41)/2\ =\ 26.455\,°C = 299.61\,K$$

The specific heat of the air from equation (D.3.2):

$$c_{pa2} = 1.045356\times10^{3} - 3.161783\times10^{-1}\times299.61 + 7.083814\times10^{-4}\times299.61^{2} - 2.705209\times10^{-7}\times299.61^{3} = 1006.94 \text{ J/kgK}$$

From equation (D.3.3), the dynamic viscosity of the air is

$$\mu_{a2} = 2.287973\times10^{-6} + 6.259793\times10^{-8}\times299.61 - 3.131955\times10^{-11}\times299.61^{2} + 8.150380\times10^{-15}\times299.61^{3} = 1.8451\times10^{-5} \text{ kg/ms}$$

The thermal conductivity of the air from equation (D.3.4):

$$k_{a2} = -4.937787\times10^{-4} + 1.018087\times10^{-4}\times299.61 - 4.627937\times10^{-8}\times299.61^{2} + 1.250603\times10^{-11}\times299.61^{3} = 0.02619 \text{ W/mK}$$

The Prandtl number of the air is therefore

$$Pr_{a2} = \frac{\mu_{a2}c_{pa2}}{k_{a2}} = \frac{1.8451\times10^{-5}\times1006.94}{0.02619} = 0.70939$$

The characteristic heat exchanger flow parameter for section 2 using equation (3.13):

$$Ry_2 = \frac{0.1930}{1.8451\times10^{-5}\times0.3491/4} = 119853 \text{ m}^{-1}$$

and the corresponding characteristic heat transfer parameter from equation (3.12):

$$Ny_2 = 2594.951\times119853^{0.3184} = 107441 \text{ m}^{-1}$$

Upon rearranging equation (3.11), the effective air side thermal conductance is then

$$(h_{ae}A_a)_2 = 107441\times0.02619\times0.70739^{1/3}\times0.3491/4 = 218.81 \text{ W/K}$$

From equation (3.16), the overall heat transfer coefficient based on the condensation surface area in section 2 of the tube is approximately

$$U_{c2} = 218.1/(2 \times 0.097 \times 6.982/4) = 643.970 \text{ W/K}$$

Equation (3.14) is used to calculate the condensation heat transfer coefficient:

$$h_{c2} = 0.9245\left[\frac{6.982/4 \times 0.63663^3 \times 990.52^2 \times 9.7962 \times \cos(60) \times 2395979}{5.9861 \times 10^{-4} \times 0.193/2 \times 1006.94 \times (44.56 - 17.5)} \times \frac{1}{[1 - \exp\{-643.970 \times 6.982/4 \times 0.097/(0.193/2 \times 1006.94)\}]}\right]^{0.333}$$
$$= 15687.0 \text{ W/m}^2\text{K}$$

The condensation heat transfer area is

$$A_{c2} = L_{et}/4 \times P_{et} = 6.982/4 \times 205.2 \times 10^{-3} = 0.3582 \text{ m}^2$$

and the overall heat transfer coefficient from equation (3.10):

$$(U_a A_a)_2 = \left[\frac{1}{218.81} + \frac{1}{15687 \times 0.3582}\right]^{-1} = 210.62 \text{ W/K}$$

The effectiveness of section 2 of the finned tube is given by equation (3.6) as

$$e_2 = 1 - \exp[-210.62/(0.193 \times 1006.94)] = 0.6617$$

and finally the airside heat transfer rate in section 2 of the tube using equation (3.5):

$$Q_{a2} = 0.193 \times 1006.94 \times (44.56 - 17.5) \times 0.6617 = 3479.7 \text{ W}$$

The air outlet temperature is then obtained from equation (3.18):

$$T_{ao2} = 17.5 + 3479.7/(0.193 \times 1006.94) = 35.41\,°C,$$

exactly the same temperature as was initially assumed.

The predicted heat transfer data for the other tube sections have been tabulated in Table B.3.

Table B. 3: The predicted heat transfer data

	T_{sm} (°C)	T_{ao} (°C)	Ry m^{-1}	$h_{ae}A_a$ (W/K)	h_c (W/m^2K)	e	Q_a (W)
Section 1	44.84	36.13	114083	216.0	15924	0.6748	3347
Section 2	44.56	35.41	119853	218.8	15687	0.6617	3480
Section 3	44.27	35.00	122436	220.3	15599	0.6565	3515
Section 4	43.99	34.83	120639	219.2	15620	0.6603	3480
Total	-	-	-	-	-	-	13822

The measured steamside heat transfer rate, Q_s = 13491. The difference between the measured steamside heat transfer rate and the predicted heat transfer rates is therefore $(13822 - 13491)/13491 \times 100\,\% = 2.5\,\%$, which is within experimental error.

APPENDIX C

CALIBRATION OF THE ANEMOMETERS USED TO MEASURE THE AIR FLOW

As described in Chapter 4, and shown in Figures 4.7 and 4.8, a 200 mm PVC pipe is placed on top of the wooden casing in which the experimental finned tube is supported. This pipe is divided into 4 sections of equal length, each section closed at either end and perforated with a large number of 20 mm holes. Using a centrifugal fan, air is drawn into the wooden casing and over the finned tube. Thereafter it flows into the 4 pipe sections, and through flow-measuring ducts connected to each pipe section. An outlet manifold ducts the air via a 400 mm flexible pipe to the centrifugal fan.

In order to determine the air mass flow rate over each section of the finned tube, the air mass flow rate in each of the four flow-measuring ducts needs to be measured. Calibrated propeller-type anemometers are used for this purpose. Each anemometer was calibrated on an individual basis prior to the commencement of the experimental tests. The entire calibration procedure will now be described in detail.

C.1. The calibration apparatus and procedure

Figure C.1 is a diagrammatic representation of the apparatus used to calibrate the anemometers. The outlet manifold was removed and all the flow-measuring ducts except the duct housing the anemometer to be calibrated were sealed. A portable wind tunnel with a 100 mm inner diameter elliptical nozzle inside it was attached to the end of the air duct. Care was taken to ensure that the entire system between the tube and the wind tunnel was well sealed. A centrifugal fan attached to the other end of the wind tunnel was used to suck air over the finned tube and through the flow-measuring duct. With the aid of a valve situated between the fan and the wind tunnel the air volume flow rate through the duct could be regulated.

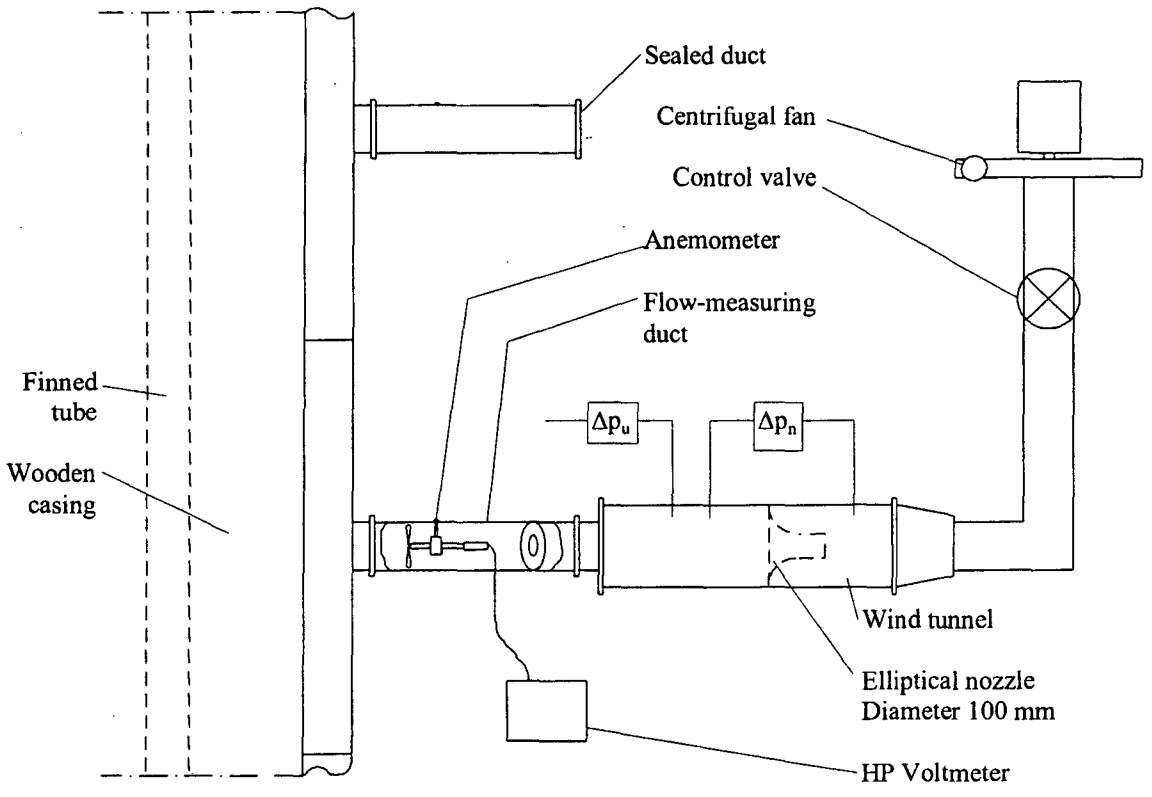

Figure C.1: The anemometer calibration apparatus

Prior to starting the calibration tests, the air temperature and pressure in the laboratory were noted. The centrifugal fan was then switched on and the air flow rate adjusted to a predetermined minimum value using the control valve. Once the flow through the system had settled, the pressure drop across the elliptical nozzle as well as the pressure upstream of the nozzle relative to atmospheric pressure were measured using a Betz water manometer. The corresponding output voltage of the anemometer was simultaneously measured using a HP integrating voltmeter. This process was repeated for each air volume flow rate until the maximum possible flow rate over the finned tube had been obtained. The data was then used to determine the relationship between the anemometer output voltage and the corresponding air volume flow rate.

C.2. Calibration sample calculation

The calibration experimental readings have been included in tables at the end of this Appendix. To demonstrate the calculations involved in calibrating the anemometers, a

sample calculation using one specific test reading will now be done. Consider Reading 6 taken for Anemometer 3. The applicable data for that specific test is as follows:

Ambient temperature in laboratory,	T_{amb}	= 25.5 °C
Barometer pressure reading,	$p_{barometer}$	= 100220 Pa
Temperature at barometer,	$T_{barometer}$	= 25.5 °C
Anemometer output voltage,	E_{anem}	= 0.454519 V
Pressure drop over nozzle,	Δp_n	= 324 Pa
Relative upstream pressure,	Δp_u	= -1192 Pa
Nozzle diameter,	d_n	= 0.100 m
Windtunnel cross-sectional area,	A_{tus}	= 0.09 m^2
Nozzle cross-sectional area,	A_n	= 0.007854 m^2

In order to calculate the actual atmospheric pressure, corrections due to temperature, latitude and altitude have to be made to the barometer reading. Stellenbosch is at an altitude of 200 m above sea level. The pressure correction due to altitude is therefore negligible and will be ignored.

According to [85TH1] the change in pressure due to temperature is given as

$$\Delta p_{temp} = -0.000162 \times p_{barometer} \times T_{barometer}(°C) \qquad (C.1)$$
$$= -0.000162 \times 100220 \times 25.5 = -414.01 \text{ Pa}$$

Stellenbosch is at a latitude of 34°S. [85TH1] gives the pressure change correction necessary due to latitude as

$$\Delta p_{lat} = -2.56 \times 10^{-4} \times \cos(2 \times \angle_{lat}) \times (p_{barometer} + \Delta p_{temp}) \qquad (C.2)$$
$$= -2.56 \times 10^{-4} \times \cos(2 \times 34) \times (100220 - 414.01) = -96.54 \text{ Pa}$$

The actual atmospheric pressure is then

$$p_{amb} = p_{barometer} + \Delta p_{lat} + \Delta p_{temp} \qquad (C.3)$$
$$= 100220 - 96.54 - 414.01 = 99709.45 \text{ Pa}$$

The pressure upstream of the nozzle is therefore

$$p_u = p_{amb} - \Delta p_u = 99705.45 - 1192 = 98517\,\text{Pa} \tag{C.4}$$

For an elliptical nozzle the mass flow rate through the nozzle is given by

$$m = C_n \phi_g Y \alpha A_n (2\rho_n \Delta p_n)^{0.5} \tag{C.5}$$

The nozzle discharge coefficient, C_n, is a function of the Reynolds number. For $30000 < Re_n < 100000$

$$C_n = 0.954803 + 6.37817 \times 10^{-7}\, Re_n - 4.65394 \times 10^{-12}\, Re_n^2 + 1.33514 \times 10^{-17}\, Re_n^3, \tag{C.6}$$

for $100000 < Re_n < 350000$

$$C_n = 0.9758 + 1.08 \times 10^{-7}\, Re_n - 1.6 \times 10^{-13}\, Re_n^2, \tag{C.7}$$

and for $Re_n > 350000$, $C_n = 0.994$.

The gas expansion factor ϕ_g is approximated as follows:

$$\phi_g = 1 - 3\Delta p_n / (4 p_u c_p / c_v) \tag{C.8}$$
$$= 1 - 3 \times 324 / (4 \times 98517.45 \times 1.4) = 0.9982$$

where for air $c_p/c_v = 1.4$. Air can be considered a compressible fluid and thus the approach velocity factor is approximately

$$Y = 1 + 0.5 (A_n / A_{tus})^2 + 2 (A_n / A_{tus})^2 \Delta p_n / (p_u c_p / c_v) \tag{C.9}$$
$$= 1 + 0.5 \times \left(\frac{7.854 \times 10^{-3}}{0.09} \right)^2 + 2 \times \left(\frac{7.854 \times 10^{-3}}{0.09} \right)^2 \times \frac{324}{98517.45 \times 1.4}$$
$$= 1.00384$$

The calibration tests were isothermal and therefore deformation of the nozzle due to thermal expansion can be neglected.

At the nozzle the air temperature is 25.5 °C and the pressure 98517.45 Pa. At these conditions the relevant air properties are as follows:
The air density from equation (D.3.1):

$$\rho_n = \frac{p_u}{RT} = \frac{98517.45}{287.08 \times (25.5 + 273.15)} = 1.14907 \text{ kg/m}^3$$

The dynamic viscosity of air as given by equation (D.3.3):

$$\mu_a = 2.287973 \times 10^{-6} + 6.259793 \times 10^{-8} \times 298.65 - 3.131956 \times 10^{-11} \times 298.65^2 + 8.150380 \times 10^{-15} \times 298.65^3 = 1.84065 \times 10^{-5} \text{ kg/ms}$$

The discharge coefficient, C_n, is a function of the Reynolds number and can be determined using an iterative procedure. It was found that $C_n = 0.988207$ and thus the air mass flow rate through the nozzle as calculated from equation (C.5) is

$$m_a = 0.988207 \times 0.9982 \times 1.00384 \times 7.854 \times 10^{-3} \times (2 \times 1.14907 \times 324)^{0.5} = 0.212226 \text{ kg/s}$$

The corresponding nozzle Reynolds number is then

$$Re_n = \frac{m_a d_n}{A_n \mu_a} = \frac{0.212226 \times 0.1}{7.854 \times 10^{-3} \times 1.84064 \times 10^{-5}} = 146804$$

Since $100000 < Re_n < 350000$, the discharge coefficient is calculated as

$$C_n = 0.9758 + 1.08 \times 10^{-7} \times 146804 - 1.6 \times 10^{-13} 146804^2 = 0.988207,$$

the same value as above. The mass flow rate through the nozzle is thus 0.212226 kg/s and the corresponding volume flow rate

$$V_a = m_a / \rho_n = 0.212226 / 1.14907 = 0.184693 \text{ m}^3/\text{s}$$

The results of the calculations performed for each experimental reading have been tabulated at the end of this Appendix.

C.3. The calibration curves of the anemometers

The air volume flow rate flowing through each flow-measuring duct was determined as a function of the anemometer output voltage. This relationship was obtained for each anemometer by performing a linear regression on the calibration data of each anemometer. The processed calibration data and corresponding calibration curve for each anemometer are given graphically below.

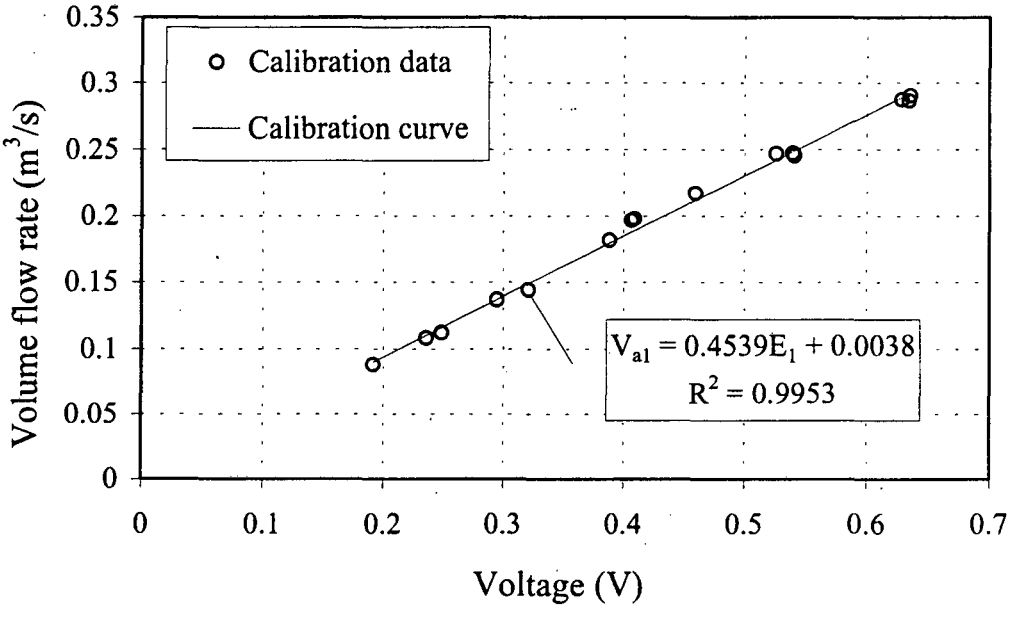

Figure C.2: The calibration data and calibration curve for Anemometer 1

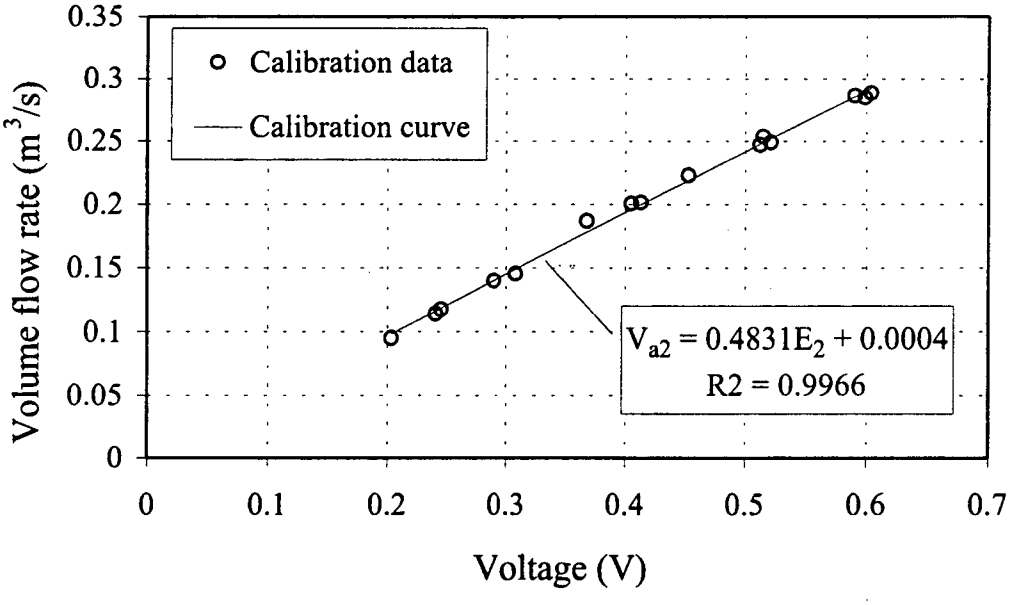

Figure C.3: The calibration data and calibration curve for Anemometer 2.

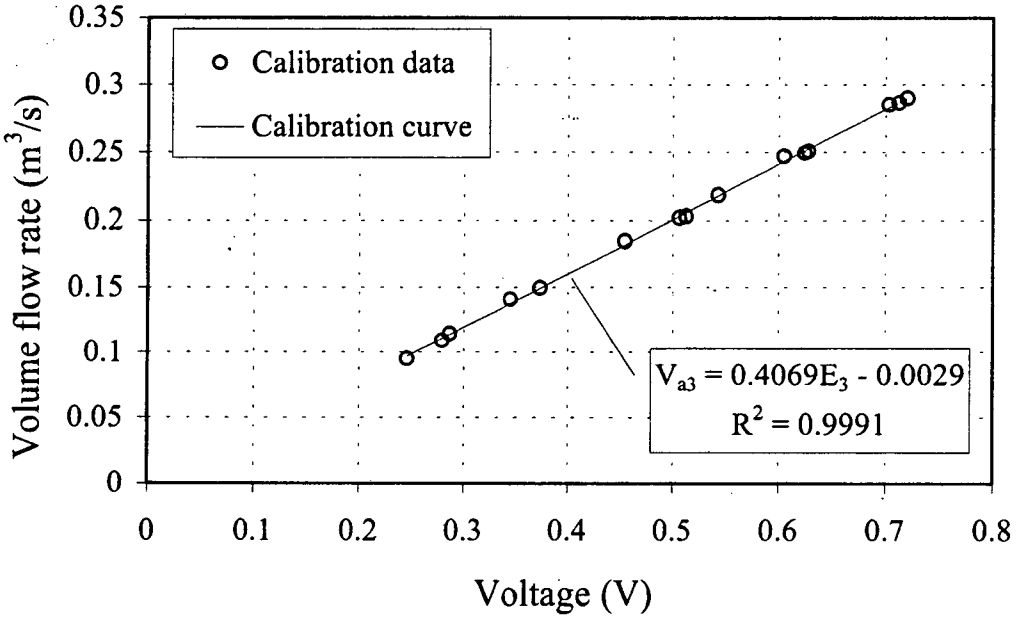

Figure C.4: The calibration data and calibration curve for Anemometer 3

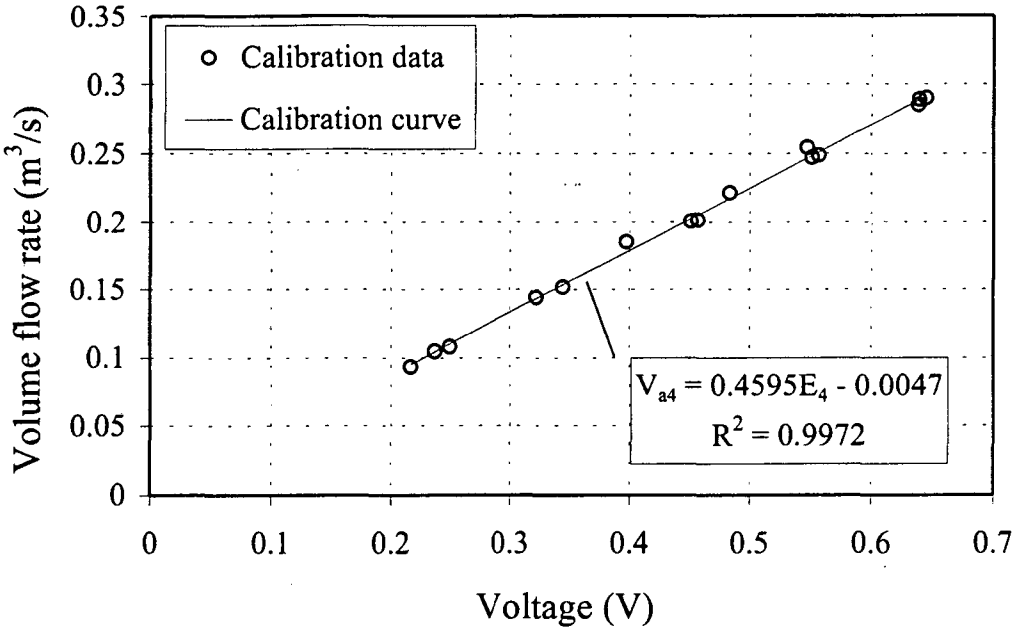

Figure C.5: The calibration data and calibration curve for Anemometer 4

Table C.1: The calibration data for Anemometer 1 and Anemometer 2

Anemometer 1				Anemometer 2			
T_{amb} (°C)	$p_{barometer}$ (Pa)		$T_{barometer}$ (°C)	T_{amb} (°C)	$p_{barometer}$ (Pa)		$T_{barometer}$ (°C)
25.5	100220		25.5	25.5	100220		25.5
Reading	Δp_n (Pa)	Δp_u (Pa)	E_{anem1} (V)	Reading	Δp_n (Pa)	Δp_u (Pa)	E_{anem1} (V)
1	76	33	0.19146	1	88	38	0.20343
2	113	382	0.23573	2	126	374	0.24066
3	122	52	0.24846	3	134	57	0.24505
4	180	634	0.29479	4	188	552	0.28967
5	200	86	0.321	5	204	86	0.30809
6	314	1099	0.38856	6	332	1006	0.36791
7	371	205	0.40636	7	386	205	0.40525
8	376	158	0.4089	8	389	162	0.41311
9	446	1568	0.45955	9	471	1418	0.45298
10	573	2074	0.52608	10	584	332	0.51235
11	585	240	0.53973	11	606	1822	0.51493
12	576	314	0.54115	12	593	242	0.5213
13	786	427	0.62891	13	782	413	0.59049
14	782	318	0.63477	14	775	336	0.5989
15	804	328	0.63577	15	795	325	0.6037

Table C.2: The calibration data for Anemometer3 and Anemometer 4

Anemometer 3				Anemometer 4			
T_{amb} (°C)	$p_{barometer}$ (Pa)		$T_{barometer}$ (°C)	T_{amb} (°C)	$p_{barometer}$ (Pa)		$T_{barometer}$ (°C)
25	100220		25.5	26.5	100180		26.5
Reading	Δp_n (Pa)	Δp_u (Pa)	E_{anem1} (V)	Reading	Δp_n (Pa)	Δp_u (Pa)	E_{anem1} (V)
1	88	34	0.24592	1	84	35	0.21658
2	115	429	0.27933	2	105	360	0.23692
3	126	49	0.28657	3	112	48	0.24935
4	190	713	0.34499	4	198	659	0.32231
5	215	85	0.37346	5	221	96	0.34479
6	324	1192	0.45452	6	326	1081	0.39742
7	390	203	0.50641	7	384	214	0.45128
8	394	156	0.51278	8	388	168	0.45711
9	450	1685	0.54327	9	463	1474	0.48355
10	572	2095	0.60521	10	607	1876	0.54769
11	594	312	0.62456	11	582	330	0.55161
12	601	236	0.62815	12	590	255	0.55727
13	776	306	0.7033	13	774	333	0.63854
14	782	466	0.71237	14	795	406	0.63905
15	803	318	0.72026	15	802	351	0.64495

Table C.3: Calculated data used to determine the calibration curves of Anemometer 1 and Anemometer 2

Anemometer 1					Anemometer 2				
Reading	C_n	m_a (kg/s)	Re_n	V_a (m^3/s)	Reading	C_n	m_a (kg/s)	Re_n	V_a (m^3/s)
1	0.981	0.103	70971	0.089	1	0.982	0.111	76596	0.095
2	0.984	0.125	86582	0.108	2	0.984	0.133	91675	0.114
3	0.984	0.130	90151	0.112	3	0.985	0.137	94723	0.118
4	0.986	0.158	109308	0.137	4	0.986	0.162	112008	0.140
5	0.986	0.167	115580	0.144	5	0.986	0.169	116984	0.146
6	0.988	0.209	144273	0.182	6	0.988	0.215	148758	0.187
7	0.989	0.228	157613	0.197	7	0.989	0.233	161123	0.201
8	0.989	0.230	158715	0.198	8	0.989	0.234	161787	0.201

Table C.3 continued

9	0.990	0.249	171685	0.217	9	0.990	0.256	176961	0.223
10	0.991	0.281	194180	0.247	10	0.991	0.287	198225	0.247
11	0.991	0.287	198071	0.248	11	0.991	0.290	200391	0.254
12	0.991	0.284	196463	0.246	12	0.991	0.289	199843	0.249
13	0.992	0.332	229416	0.287	13	0.992	0.332	229330	0.286
14	0.992	0.331	228960	0.286	14	0.992	0.330	228392	0.285
15	0.992	0.336	232145	0.290	15	0.992	0.334	231332	0.288

Table C.4: Calculated data used to determine the calibration curves of Anemometer 3 and Anemometer 4

Anemometer 3					Anemometer 4				
Reading	C_n	m_a (kg/s)	Re_n	V_a (m^3/s)	Reading	C_n	m_a (kg/s)	Re_n	V_a (m^3/s)
1	0.982	0.111	76597	0.095	1	0.982	0.108	74479	0.093
2	0.984	0.127	87517	0.109	2	0.983	0.121	83238	0.105
3	0.984	0.133	91827	0.114	3	0.984	0.125	86135	0.108
4	0.986	0.163	112514	0.141	4	0.986	0.166	114389	0.144
5	0.986	0.174	120117	0.149	5	0.987	0.176	121239	0.152
6	0.988	0.212	146804	0.185	6	0.988	0.213	146682	0.186
7	0.989	0.234	161962	0.202	7	0.989	0.232	159975	0.201
8	0.989	0.235	162834	0.203	8	0.989	0.233	160848	0.202
9	0.990	0.250	172716	0.218	9	0.990	0.253	174608	0.222
10	0.991	0.281	194398	0.247	10	0.991	0.289	199601	0.254
11	0.991	0.289	199940	0.249	11	0.991	0.286	197000	0.247
12	0.991	0.291	201196	0.251	12	0.991	0.288	198429	0.249
13	0.992	0.330	228574	0.285	13	0.992	0.329	227225	0.285
14	0.992	0.331	229268	0.286	14	0.992	0.334	230200	0.289
15	0.992	0.336	232501	0.290	15	0.992	0.335	231276	0.290

APPENDIX D

PROPERTIES OF FLUIDS

D.1. The thermophysical properties of saturated water vapor from 273.16 K to 380 K

D.1.1 Vapor pressure

$$p_{vsat} = 10^{z}, \quad N/m^2 \tag{D.1.1}$$

$$z = a \times (1 - x) + b \times \log_{10}(x) + c \times [1 - 10^{d \times (1/x - 1)}] + e \times [10^{f \times (1 - x)} - 1] + g$$

$$x = \frac{273.16}{T}$$

$a = 1.079586 \times 10$

$b = 5.02808$

$c = 1.50474 \times 10^{-4}$

$d = -8.29692$

$e = 4.2873 \times 10^{-4}$

$f = 4.76955$

$g = 2.786118312$

D.1.2 Dynamic viscosity

$$\mu_g = a + bT + cT^2 + dT^3, \quad kg/ms \tag{D.1.2}$$

$a = 2.562435 \times 10^{-6}$

$b = 1.816683 \times 10^{-8}$

$c = 2.579066 \times 10^{-11}$

$d = -1.067299 \times 10^{-14}$

D.1.3 Density

$$\rho_g = a + bT + cT^2 + dT^3 + eT^4 + fT^5, \quad kg/m^3 \tag{D.1.3}$$

$a = -4.062329056$

$b = 0.10277044$

$c = -9.76300388 \times 10^{-4}$

$d = 4.475240795 \times 10^{-6}$

$e = -1.004596894 \times 10^{-8}$

$f = 8.9154895 \times 10^{-12}$

D.2. The thermophysical properties of saturated water liquid from 273.16 K to 380 K

D.2.1 Density

$$\rho_w = (a + bT + cT^2 + dT^6)^{-1}, \quad kg/m^3 \tag{D.2.1}$$

$a = 1.49343 \times 10^{-3}$

$b = -3.7164 \times 10^{-6}$

$c = 7.09782 \times 10^{-9}$

$d = -1.90321 \times 10^{-20}$

D.2.2 Dynamic viscosity

$$\mu_w = a\ 10^{b/(T-c)}, \quad kg/ms \tag{D.2.2}$$

$a = 2.414 \times 10^{-5}$

$b = 247.8$

$c = 140$

D.2.3 Surface tension

$$\sigma_w = a + bT + cT^2 + dT^3, \quad N/m \tag{D.2.3}$$

$a = 5.148103 \times 10^{-2}$

$b = 3.998714 \times 10^{-4}$

$c = -1.4721869 \times 10^{-6}$

$d = 1.21405335 \times 10^{-9}$

D.2.4 Specific heat

$$c_{pw} = a + bT + cT^2 + dT^6, \quad J/kgK \tag{D.2.4}$$

$a = 8.15599 \times 10^3$

$b = -2.80627 \times 10$

$c = 5.11283 \times 10^{-2}$

$d = -2.17582 \times 10^{-13}$

D.2.5 Thermal conductivity

$$k_w = a + bT + cT^2 + dT^4, \quad W/mK \tag{D.2.5}$$

$a = -6.14255 \times 10^{-1}$

$b = 6.9962 \times 10^{-3}$

$c = -1.01075 \times 10^{-5}$

$d = 4.74737 \times 10^{-12}$

D.2.6 Latent heat of vaporization

$$i_{fg} = a + bT + cT^2 + dT^3, \quad J/kg \tag{D.2.6}$$

$a = 3.4831814 \times 10^6$

$b = -5.8627703 \times 10^3$

$c = 1.2139568 \times 10$

$d = -1.40290431 \times 10^{-2}$

D.3. The thermophysical properties of dry air from 220 K to 380 K at standard atmospheric pressure (101325 N/m^2)

D.3.1 Density

$$\rho_a = \frac{p}{R_a T}, \quad kg/m^3 \tag{D.3.1}$$

$R_a = 287.08$ J/kgK

D.3.2 Specific heat

$$c_{pa} = a + bT + cT^2 + dT^3, \quad J/kgK \tag{D.3.2}$$

$a = 1.045356 \times 10^{3}$

$b = -3.161783 \times 10^{-1}$

$c = 7.083814 \times 10^{-4}$

$d = -2.705209 \times 10^{-7}$

D.3.3 Dynamic viscosity

$$\mu_a = a + bT + cT^2 + dT^3, \quad kg/ms \tag{D.3.3}$$

$a = 2.287973 \times 10^{-6}$

$b = 6.259793 \times 10^{-8}$

$c = -3.131955 \times 10^{-11}$

$d = 8.150380 \times 10^{-15}$

D.3.4 Thermal conductivity

$$k_a = a + bT + cT^2 + dT^3, \quad W/mK \tag{D.3.4}$$

$a = -4.937787 \times 10^{-4}$

$b = 1.018087 \times 10^{-4}$

$c = -4.627937 \times 10^{-8}$

$d = 1.250603 \times 10^{-11}$

APPENDIX E

GRAPHICAL AND EXPERIMENTAL DATA

E.1. Tables of the data used to generate the graphs in Chapter 5

Table E.1: The measured vapor Froude number, Reynolds number and dimensionless pressure drop data used to generate Figures 5.1 and 5.2 as well as the vapor pressure dimensionless pressure drop data used to generate Figure 5.6.

T_s = 45 °C				Ts = 50 °C			T_s = 55 °C			
Fr_{IIsv}	Re_{sv}	Δp^+_{meas}	Δp^+_{vap}	Fr_{IIsv}	Re_{sv}	Δp^+_{meas}	Fr_{IIsv}	Re_{sv}	Δp^+_{meas}	Δp^+_{vap}
0.1173	6398	4.287	4.014	0.0806	6045	3.750	0.1371	8735	3.991	2.956
0.1188	6549	4.359	4.106	0.1137	7185	3.550	0.1540	9098	3.796	4.245
0.1478	7335	4.189	4.083	0.1510	8287	3.753	0.1759	9676	3.720	3.680
0.1928	8431	3.979	3.913	0.1866	9242	3.638	0.1934	10220	3.791	3.636
0.2253	9127	4.047	3.946	0.2234	10205	3.740	0.2304	11352	3.724	3.659
0.2912	10344	4.123	3.961	0.2532	10904	3.733	0.2648	12310	3.749	3.698
0.3120	10775	4.067	3.838	0.2897	11678	3.821	0.3058	13219	3.717	3.891
0.3442	11341	4.231	3.880	0.3187	11971	3.838	0.3160	13495	3.570	3.487
0.3729	11752	4.597	4.291	0.3317	12291	3.789	0.3533	14292	3.680	3.735
0.4279	12486	4.652	4.616	0.3324	12498	3.768	0.3750	14720	3.808	4.040
0.4474	12754	5.214	5.099	0.3627	12895	3.858	0.4086	15343	3.940	4.135
0.4602	13006	5.814	5.808	0.3722	13190	3.886	0.4377	15838	4.255	4.426
0.4473	12931	8.301	8.390	0.4077	13668	4.022	0.4481	15984	4.439	4.691
0.4481	13002	11.839	11.900	0.4093	13791	3.986	0.4640	16300	4.605	4.962
0.4465	12936	14.621	14.637	0.4463	14280	4.403	0.4705	16456	5.341	5.863
0.4491	12711	5.497	5.369	0.4643	14580	4.691	0.4464	16077	12.130	13.373
				0.4681	14663	5.119				
				0.4584	14566	8.955				
				0.4473	14319	14.269				
				0.4402	14216	19.741				

Table E.1 continued.

T_s = 60 °C			T_s = 65 °C			
Fr_{IIsv}	Re_{sv}	Δp^+_{meas}	Fr_{IIsv}	Re_{sv}	Δp^+_{meas}	Δp^+_{vap}
0.0803	7330	4.129	0.0735	7573	3.508	3.498
0.1308	9383	3.742	0.1048	9034	3.398	2.670

Table E.1 continued.

0.1748	10918	3.575	0.1478	10929	3.615	2.955
0.2091	11922	3.631	0.1747	11912	3.483	2.791
0.2485	12917	3.683	0.2134	13159	3.626	3.190
0.2883	13872	3.650	0.2430	14102	3.497	3.229
0.3290	14852	3.834	0.2807	15142	3.500	3.223
0.3702	15862	3.962	0.3130	15931	3.537	3.328
0.4051	16620	4.261	0.3446	16686	3.583	3.428
0.4376	17158	4.595	0.4005	17966	3.671	3.476
0.4499	17449	5.138	0.4410	18853	3.968	3.854
0.4291	17137	14.207	0.4572	19211	3.952	3.981
0.4460	17148	16.985	0.4864	19846	4.530	4.436
0.4920	17988	37.703	0.4621	19476	16.234	15.800
			0.4918	20052	17.709	17.983
			0.5035	20281	16.178	16.067
			0.4893	19973	27.521	28.014
			0.5042	20274	24.384	24.672
			0.5128	20428	30.637	30.822
			0.5202	20472	40.483	40.997
			0.5275	20816	47.723	47.969
			0.5516	21104	49.619	50.278
			0.5405	20925	52.501	52.900
			0.5616	21310	46.572	46.750
			0.5614	21317	54.257	54.984

Table E.2: The actual and predicted vapor velocities and pressure drop data that were used to produce Figure 5.3.

Ts = 45 °C				Ts = 55 °C				Ts = 65 °C			
Measured data		Theoretical data		Measured data		Theoretical data		Measured data		Theoretical data	
v_{sv} (m/s)	Δp (Pa)	v_{sv} (m/s)	Δp (Pa)	v_{sv} (m/s)	Δp (Pa)	v_{sv} m/s	Δp (Pa)	v_{sv} (m/s)	Δp (Pa)	v_{sv} (m/s)	Δp (Pa)
42.32	236.7	26.83	108.3	34.85	256.3	20.85	103.7	20.90	120.2	16.91	101.6
41.77	243.7	33.37	156.9	37.70	273.8	25.71	147.2	24.98	166.0	19.47	127.6
46.37	291.4	38.82	204.5	40.51	306.5	29.78	190.1	29.01	248.8	21.72	153.3
52.57	361.0	43.59	252.1	42.14	343.6	33.36	233.0	31.44	283.3	23.77	178.9
56.73	429.0	47.90	300.1	45.04	401.7	36.60	276.2	34.78	360.3	25.65	204.5
64.73	564.9	51.84	348.6	47.63	464.5	39.56	319.9	36.92	395.6	27.40	230.2
67.40	597.1	55.51	397.9	51.24	531.9	42.32	364.4	39.72	457.4	29.05	256.0

Table E.2 continued.

71.01	685.1	58.94	448.2	51.83	527.9	44.92	409.8	42.14	515.4	30.61	282.0
74.91	806.5	62.19	499.7	54.70	608.4	47.37	456.1	44.31	575.0	32.09	308.3
78.86	936.6	65.28	552.4	56.39	668.4	49.70	503.6	47.84	684.7	33.51	334.9
80.73	1097.6	68.23	606.5	58.95	753.5	51.92	552.3	50.20	814.8	34.86	361.8
81.36	1258.9	71.05	662.2	61.21	871.8	54.05	602.4	51.07	841.5	36.17	389.1
79.44	1746.8	73.77	719.4	62.11	931.1	56.11	653.9	52.57	1025.9	37.44	416.8
79.08	2495.6	76.39	778.4	63.05	1000.2	58.09	706.8	50.83	3492.8	38.66	444.9
79.25	3071.3	78.92	839.3	63.30	1176.1	60.00	761.4	52.56	4055.2	39.84	473.4
81.38	1161.9	81.38	902.1	61.43	2533.8	61.86	817.7	53.21	3792.3	40.99	502.5
								52.52	6270.4	42.11	532.0
								53.31	5724.5	43.20	562.0
								53.82	7315.2	44.26	592.6
								54.53	9807.0	45.30	623.8
								54.29	11720.8	46.32	655.5
								56.08	12745.3	47.31	687.9
								55.41	13215.4	48.28	720.8
								56.54	12179.5	49.23	754.5
								56.49	14183.4	50.17	788.8

Table E.3: The dimensionless pressure drop data as predicted using the Zapke-Kröger pressure drop model that were used in generating Figure 5.4.

T_s = 45 °C		T_s = 55 °C		T_s = 65 °C	
Fr_{llsv}	$\Delta p/(0.5\rho v^2)$	Fr_{llsv}	$\Delta p/(0.5\rho v^2)$	Fr_{llsv}	$\Delta p/(0.5\rho v^2)$
0.050	4.606	0.050	4.431	0.050	4.364
0.077	4.311	0.076	4.139	0.066	4.137
0.105	4.154	0.102	3.982	0.083	3.991
0.132	4.060	0.128	3.889	0.099	3.891
0.159	4.002	0.154	3.831	0.115	3.818
0.187	3.969	0.180	3.797	0.131	3.766
0.214	3.952	0.206	3.779	0.148	3.727
0.241	3.947	0.232	3.773	0.164	3.698
0.269	3.953	0.258	3.777	0.180	3.678
0.296	3.967	0.284	3.788	0.196	3.664
0.323	3.987	0.310	3.806	0.213	3.656
0.351	4.014	0.336	3.830	0.229	3.653
0.378	4.045	0.362	3.858	0.245	3.653

Table E.3 continued.

0.405	4.082	0.388	3.892	0.261	3.657
0.433	4.123	0.414	3.929	0.278	3.663
0.460	4.168	0.440	3.970	0.294	3.673
				0.310	3.685
				0.326	3.699
				0.343	3.715
				0.359	3.733
				0.375	3.753
				0.391	3.775
				0.408	3.798
				0.424	3.823
				0.440	3.849

Table E.4: The theoretical dimensionless pressure drop components of the total predicted pressure drop as well as the measured pressure drop data that were used in generating Figure 5.5

Predicted data						Measured data	
Fr_{llsv}	Δp_{inlet}^{+}	Δp_{fric}^{+}	Δp_{mom}^{+}	Δp_{grav}^{+}	Δp_{tot}^{+}	Fr_{llsv}	Δp_{tot}^{+}
0.050	1.650	4.791	-2	0.165	4.606	0.117	4.287
0.077	1.699	4.506	-2	0.106	4.311	0.119	4.359
0.105	1.749	4.326	-2	0.079	4.154	0.148	4.189
0.132	1.801	4.197	-2	0.062	4.06	0.193	3.979
0.159	1.854	4.097	-2	0.052	4.002	0.225	4.047
0.187	1.909	4.016	-2	0.044	3.969	0.291	4.123
0.214	1.965	3.949	-2	0.038	3.952	0.320	3.962
0.241	2.023	3.891	-2	0.034	3.947	0.357	4.076
0.269	2.082	3.84	-2	0.031	3.953	0.394	4.355
0.296	2.143	3.796	-2	0.028	3.967	0.428	4.652
0.323	2.206	3.756	-2	0.025	3.987	0.447	5.214
0.351	2.271	3.719	-2	0.023	4.014	0.460	5.814
0.378	2.337	3.687	-2	0.022	4.045	0.447	8.301
0.405	2.405	3.656	-2	0.02	4.082	0.448	11.839
0.433	2.475	3.628	-2	0.019	4.123	0.447	14.621
0.460	2.548	3.602	-2	0.018	4.168	0.449	5.497

Table E.5: The flooding superficial vapor Froude number data obtained in this investigation and by Reuter and Kröger [96RE1] as well as the predicted flooding data that were used to produce Figure 5.7.

	$Fr_{11sv\text{-}flooding}$		
$Fr_{dsl}^{0.6}/Zk_{dh}^{0.2}$	Eqn (5.2)	Exp. data	[96RE1]
0.000421	0.4894		0.4861
0.000512	0.4881		0.4792
0.000598	0.4869		0.4678
0.000684	0.4858		0.4258
0.000946	0.4822	0.4602	
0.000963	0.4819	0.4495	
0.001077	0.4804	0.4657	
0.001084	0.4803	0.4681	
0.001084	0.4803	0.4681	
0.001245	0.4780	0.4705	
0.001268	0.4777	0.4818	
0.001377	0.4762	0.4499	
0.001365	0.4764	0.4616	
0.001541	0.4740	0.4864	
0.001575	0.4735	0.4730	

Table E.6: the transient pressure drop data measured by Zapke [97ZA2] that were used to plot Figure 5.8.

Time (s)	Δp_{tot} (Pa)	Δp_{12} (Pa)	Δp_{23} (Pa)
0.00	446.31	217.32	228.99
0.55	458.15	231.34	226.81
1.10	459.51	210.83	248.68
1.65	460.22	231.72	228.50
2.20	449.31	226.16	223.16
2.75	452.53	232.32	220.21
3.52	450.45	218.90	231.56
4.34	477.78	245.19	232.59
5.00	492.62	240.07	252.56
5.77	486.62	234.06	252.56
6.60	488.09	265.59	222.50
7.31	499.38	262.92	236.46

Table E.6 continued

8.08	491.20	242.25	248.96
8.90	516.84	273.07	243.77
9.62	531.84	285.50	246.34
10.39	544.99	283.59	261.39
11.21	538.66	285.07	253.59
11.92	665.32	420.56	244.76
12.75	1023.48	767.65	255.83
13.57	1448.19	1324.42	123.77
14.34	1859.18	731.32	1127.85
15.16	1985.55	1496.58	488.96
15.93	1826.31	329.58	1496.73
16.65	2465.21	1445.76	1019.45
17.47	1907.29	880.89	1026.40
18.29	1896.05	374.47	1521.58
19.01	1647.46	952.52	694.94

Table E.7: The flooding vapor velocity as measured in this investigation and by Reuter and Kröger [96RE1] and the predicted flooding velocity data that were used in plotting Figure 5.10.

	vsv (m/s)		
Tsi (°C)	Eqn (5.3)	Exp. data	[96RE1]
44.67	47.024		46.867
44.99	83.276	81.361	
45.69	81.849	79.047	
50.16	73.432	72.300	
50.41	72.995	72.064	
50.41	72.995	72.064	
52.76	38.744		38.387
56.15	63.805	63.301	
56.91	62.702	62.970	
59.74	33.056		32.399
60.07	58.367	57.453	
60.45	57.872	56.248	
65.39	51.899	52.573	
66.39	50.788	50.758	
68.02	27.646		25.884

Table E.8: The airside and steamside heat transfer data used to generate Figure 5.11.

Ts = 45 °C		Ts = 50 °C		Ts = 55 °C		Ts = 60 °C		Ts = 65 °C	
Q_a (kW)	Q_s (kW)	Q_a (kW)	Q_s (kW)	Q_a (kW)	Q_s (kW)	Q_a (kW)	Q_s (kW)	Q_a (kW)	Q_s (kW)
7.57	8.33	7.00	7.96	10.25	11.61	7.54	9.53	8.63	10.25
7.96	8.53	8.70	9.46	10.85	12.06	10.86	12.18	11.12	12.21
9.03	9.55	10.55	10.92	11.74	12.84	13.21	14.19	13.92	14.80
10.64	10.99	11.80	12.18	12.81	13.57	14.96	15.49	15.66	16.14
11.74	11.91	13.23	13.46	14.53	15.09	16.69	16.79	17.91	17.83
13.26	13.49	14.16	14.38	16.11	16.39	17.68	18.02	19.08	19.11
14.24	14.06	15.42	15.41	17.20	17.59	19.54	19.30	20.52	20.51
15.07	14.80	16.07	15.76	17.57	17.98	21.30	20.45	21.28	21.58
15.75	15.33	16.18	16.03	18.42	19.04	22.32	21.36	22.60	22.38
16.27	15.70	16.48	16.11	19.42	19.62	23.02	22.03	24.33	23.65
16.62	15.94	16.99	16.50	20.43	20.13	23.42	22.33	25.53	24.59
16.96	16.20	17.39	16.88	21.09	20.72	23.02	22.10	26.01	25.11
16.87	16.27	18.00	17.09	21.28	20.88	22.99	22.18	26.88	25.62
16.97	16.33	18.18	17.55	21.70	21.16	24.11	23.80	26.39	25.22
16.88	16.23	18.81	17.78	21.91	21.31			27.17	24.95
16.55	15.85	19.20	18.07	21.42	20.28			27.48	25.52
		19.32	18.26					27.06	25.14
		19.20	18.35					27.47	25.72
		18.86	17.98					27.67	25.65
		18.73	17.43					27.72	26.32
								28.21	26.01
								28.58	25.54
								28.34	26.16
								28.86	26.54
								28.87	26.43

Table E.9: The ideal heat transfer data and the measured heat transfer data that were plotted in Figure 5.12.

Ts = 45 °C			Ts = 65 °C		
$Fr_{1lsv\text{-}ideal}$	Q_{ideal} (kW)	Q_{exp} (kW)	$Fr_{1lsv\text{-}ideal}$	Q_{ideal} (kW)	Q_{exp} (kW)
0.116	8.27	8.33	0.072	10.17	10.25
0.123	8.67	8.53	0.110	12.51	12.21
0.152	9.68	9.55	0.155	15.15	14.80

Table E.9 continued.

0.200	11.19	10.99	0.189	16.78	16.14
0.239	12.26	11.91	0.239	18.87	17.91
0.306	13.82	13.49	0.266	19.98	19.11
0.336	14.59	14.24	0.302	21.30	20.52
0.372	15.38	15.07	0.330	22.15	21.58
0.409	16.04	15.75	0.367	23.31	22.60
0.442	16.53	16.27	0.417	24.83	24.33
0.465	16.94	16.62	0.455	25.94	25.53
0.483	17.37	16.96	0.471	26.40	26.01
0.489	17.63	16.87	0.497	27.18	26.88
0.522	18.32	16.97	0.495	27.30	26.39
0.567	19.02	16.88	0.530	28.21	27.17
0.472	16.96	16.55	0.538	28.39	27.48
			0.543	28.52	27.06
			0.558	28.89	27.47
			0.577	29.35	27.67
			0.613	30.08	27.72
			0.646	31.21	28.21
			0.694	32.05	28.58
			0.686	31.93	28.34
			0.691	32.02	28.86
			0.717	32.63	28.87

E.2. Tables of the measured experimental data

Table E.10: The measured experimental data obtained from experiments performed at a steam temperature of 45 °C.

Read	T_{si} (°C)	T_{so} (°C)	T_{ai1} (°C)	T_{ai2} (°C)	T_{ai3} (°C)	T_{ai4} (°C)	T_{ao1} (°C)	T_{ao2} (°C)	T_{ao3} (°C)	T_{ao4} (°C)	Δp (Pa)	m_{sc} (g/s)	Q_s (kW)
1	43.77	43.29	17.91	17.59	16.68	16.37	37.97	37.56	37.21	36.54	236.67	3.47	8.33
2	44.56	44.08	18.12	17.5	17.08	16.95	38.59	38.18	37.81	37.11	243.69	3.56	8.53
3	44.76	44.17	18.08	17.74	17.14	16.92	38.15	37.75	37.37	36.71	291.35	3.99	9.55
4	45.06	44.33	18.1	17.75	17.09	16.86	37.53	37.13	36.76	36.15	360.95	4.59	10.99
5	45.13	44.27	18.14	17.6	17.3	17.07	36.75	36.34	36.01	35.46	429	4.97	11.91
6	44.98	43.85	18.07	17.5	17.28	17.01	35.24	34.79	34.52	33.93	564.86	5.63	13.49
7	45.28	44.09	18.14	17.91	17.3	16.94	35.14	34.77	34.46	33.87	597.06	5.87	14.06
8	45.38	44.04	18.1	17.86	17.37	16.91	34.61	34.25	33.95	33.36	685.05	6.18	14.8

Table E.10 continued

9	45.17	43.51	18.08	17.66	17.15	16.9	33.77	33.39	33.05	32.51	806.5	6.4	15.33
10	44.78	42.79	17.94	17.65	16.99	16.62	32.88	32.51	32.11	31.56	936.61	6.55	15.7
11	44.73	42.41	17.64	17.23	16.84	16.35	32.33	31.91	31.58	31.01	1097.57	6.66	15.94
12	44.99	42.28	17.56	17.32	16.58	16.06	32.05	31.69	31.23	30.64	1258.86	6.76	16.2
13	45.39	41.56	17.55	17.29	16.3	15.86	31.45	31.11	30.49	30.03	1746.75	6.79	16.27
14	45.61	40.01	17.55	17.14	16.08	15.68	30.06	29.53	28.7	28.58	2495.56	6.82	16.33
15	45.45	38.3	17.49	16.99	16.11	15.59	28.34	27.75	26.75	26.92	3071.28	6.78	16.23
16	44.48	41.99	17.6	17.08	15.92	15.38	32.15	31.63	30.98	30.36	1161.93	6.62	15.85

Table E.10 continued.

Read	V_{a1} (m^3/s)	V_{a2} (m^3/s)	V_{a3} (m^3/s)	V_{a4} (m^3/s)	m_{at} (kg/s)	Q_{a1} (kW)	Q_{a2} (kW)	Q_{a3} (kW)	Q_{a4} (kW)	Q_{at} (kW)	EB (%)
1	0.084	0.085	0.081	0.081	0.373	1.907	1.927	1.886	1.85	7.57	-1.7
2	0.087	0.088	0.084	0.084	0.385	2.006	2.058	1.977	1.92	7.961	0.79
3	0.102	0.101	0.098	0.097	0.447	2.311	2.279	2.248	2.187	9.025	1.1
4	0.123	0.121	0.119	0.119	0.543	2.703	2.67	2.655	2.607	10.635	2.54
5	0.142	0.14	0.136	0.136	0.626	3.007	2.982	2.905	2.844	11.737	3.91
6	0.162	0.17	0.173	0.171	0.767	3.175	3.356	3.413	3.31	13.255	2.94
7	0.189	0.184	0.181	0.179	0.832	3.667	3.548	3.547	3.478	14.24	5.7
8	0.206	0.199	0.197	0.196	0.908	3.893	3.741	3.744	3.695	15.073	5.98
9	0.224	0.217	0.216	0.215	0.994	4.026	3.914	3.945	3.86	15.745	6.64
10	0.243	0.236	0.233	0.231	1.08	4.174	4.036	4.069	3.992	16.27	7.36
11	0.252	0.243	0.241	0.243	1.123	4.262	4.122	4.109	4.124	16.617	7.82
12	0.26	0.25	0.25	0.25	1.159	4.353	4.148	4.231	4.222	16.955	8.15
13	0.266	0.258	0.257	0.259	1.196	4.276	4.118	4.222	4.255	16.87	7.31
14	0.297	0.285	0.286	0.288	1.337	4.315	4.11	4.208	4.337	16.97	7.46
15	0.338	0.327	0.328	0.331	1.539	4.275	4.113	4.1	4.39	16.878	7.54
16	0.249	0.241	0.239	0.239	1.112	4.167	4.053	4.174	4.16	16.554	8.02

Table E.11: The measured experimental data obtained from experiments performed at a steam temperature of 50 °C.

Read	T_{si} (°C)	T_{so} (°C)	T_{ai1} (°C)	T_{ai2} (°C)	T_{ai3} (°C)	T_{ai4} (°C)	T_{ao1} (°C)	T_{ao2} (°C)	T_{ao3} (°C)	T_{ao4} (°C)	Δp (Pa)	m_{sc} (g/s)	Q_s (kW)
1	50.09	49.77	22.69	20.42	19.4	19.23	44.32	43.74	43.2	42.24	141.8	3.34	7.96
2	50.12	49.67	22.64	20.16	19.41	19.22	44	43.25	42.59	41.64	189.5	3.97	9.46
3	50.17	49.6	22.09	20.67	19.89	19.63	43.15	42.39	41.65	40.8	266	4.58	10.92

Table E.11 continued.

4	50.32	49.7	21.67	20.87	20.13	19.86	42.47	41.73	40.99	40.25	318.7	5.11	12.18
5	50.78	50.05	21.73	20.73	20.15	19.93	41.74	41.04	40.6	40	392.1	5.65	13.46
6	50.96	50.17	21.41	20.86	20.3	19.91	41.15	40.51	40.09	39.45	443.5	6.04	14.38
7	51.02	50.08	21.06	20.78	20.26	20.04	40.28	39.7	39.33	38.71	519.4	6.47	15.41
8	49.88	48.9	19.94	18.91	18.23	17.66	38.96	38.28	37.79	37.1	574.2	6.61	15.76
9	50.2	49.16	20.03	18.71	18.22	17.87	39.05	38.23	37.8	37.16	589.9	6.73	16.03
10	50.98	49.94	20.95	20.55	20.09	19.86	39.64	39.06	38.64	38.04	587.7	6.77	16.11
11	50.36	49.2	20.45	19.03	18.28	18.01	38.82	37.94	37.39	36.77	656.8	6.93	16.5
12	50.84	49.67	21.1	20.24	19.74	19.58	39.04	38.24	37.8	37.18	678.9	7.09	16.88
13	50.35	49.02	20.86	19.29	18.66	18.38	38.22	37.2	36.75	36.1	769.6	7.17	17.09
14	50.7	49.32	21	19.95	19.39	19.07	38.44	37.57	37.04	36.35	765.6	7.37	17.55
15	50.28	48.65	20.43	19.36	18.78	18.36	37.36	36.53	36.08	35.44	922.3	7.46	17.78
16	50.33	48.5	20.5	19.53	19.06	18.7	36.97	36.25	35.81	35.15	1022	7.59	18.07
17	50.41	48.43	20	19.6	19.13	18.93	36.56	36.04	35.64	35.06	1125	7.66	18.26
18	50.6	47.19	19.68	19.23	18.91	18.62	35.49	34.98	34.51	34.09	1927	7.71	18.35
19	50.36	44.67	19.39	18.91	18.56	18.15	33.56	32.86	32.27	32.2	2996	7.55	17.98
20	50.4	42.37	19.05	18.66	18.34	18.24	30.9	30.27	29.56	30.33	4078	7.32	17.43

Table E.11 continued.

Read	V_{a1} (m^3/s)	V_{a2} (m^3/s)	V_{a3} (m^3/s)	V_{a4} (m^3/s)	m_{at} (kg/s)	Q_{a1} (kW)	Q_{a2} (kW)	Q_{a3} (kW)	Q_{a4} (kW)	Q_{at} (kW)	EB (%)
1	0.064	0.068	0.071	0.07	0.303	1.538	1.773	1.882	1.804	6.998	-4.83
2	0.081	0.085	0.089	0.089	0.383	1.94	2.203	2.311	2.245	8.698	-1.49
3	0.105	0.107	0.114	0.112	0.489	2.478	2.598	2.785	2.688	10.55	2.47
4	0.121	0.122	0.132	0.131	0.566	2.82	2.862	3.1	3.022	11.8	2.12
5	0.145	0.144	0.146	0.145	0.65	3.274	3.295	3.366	3.291	13.23	2.98
6	0.159	0.155	0.161	0.161	0.714	3.538	3.447	3.605	3.571	14.16	2.89
7	0.173	0.183	0.18	0.181	0.807	3.764	3.93	3.893	3.832	15.42	4.12
8	0.184	0.185	0.182	0.18	0.825	3.955	4.068	4.055	3.987	16.07	5.82
9	0.186	0.186	0.184	0.181	0.83	4	4.112	4.103	3.969	16.18	4.82
10	0.195	0.195	0.196	0.199	0.886	4.124	4.107	4.128	4.124	16.48	6.09
11	0.203	0.2	0.198	0.195	0.898	4.227	4.287	4.303	4.168	16.99	6.56
12	0.211	0.213	0.213	0.216	0.965	4.305	4.367	4.379	4.337	17.39	6.55
13	0.226	0.223	0.222	0.219	1.006	4.445	4.554	4.571	4.433	18	8.55
14	0.224	0.226	0.228	0.232	1.032	4.448	4.552	4.595	4.582	18.18	6.9
15	0.244	0.241	0.238	0.238	1.091	4.706	4.725	4.713	4.664	18.81	8.8
16	0.256	0.252	0.252	0.252	1.149	4.801	4.821	4.831	4.75	19.2	9.17

Table E.11 continued.

17	0.261	0.256	0.257	0.256	1.169	4.925	4.801	4.849	4.74	19.32	8.74
18	0.27	0.265	0.266	0.267	1.217	4.884	4.795	4.771	4.744	19.2	7.67
19	0.294	0.291	0.292	0.292	1.341	4.805	4.682	4.633	4.741	18.86	7.99
20	0.346	0.337	0.346	0.346	1.59	4.771	4.551	4.53	4.875	18.73	10.26

Table E.12: The measured experimental data obtained from experiments performed at a steam temperature of 55 °C.

Read	T_{si} (°C)	T_{so} (°C)	T_{ai1} (°C)	T_{ai2} (°C)	T_{ai3} (°C)	T_{ai4} (°C)	T_{ao1} (°C)	T_{ao2} (°C)	T_{ao3} (°C)	T_{ao4} (°C)	Δp (Pa)	m_{sc} (g/s)	Q_s (kW)
1	55.3	55.0	19.67	18.62	17.04	16.78	47.53	46.77	46.28	45.18	256.3	4.9	11.61
2	54.4	54.0	19.67	18.88	17.29	17.07	46.43	45.84	45.34	44.28	273.8	5.09	12.06
3	54.1	53.7	19.71	18.96	17.73	17.2	45.77	45.15	44.6	43.56	306.5	5.41	12.84
4	54.5	54.1	19.58	18.81	18	17.62	45.49	44.88	44.45	43.46	343.6	5.72	13.57
5	55.4	54.9	19.29	18.63	18.09	17.66	45.31	44.78	44.41	43.42	401.7	6.37	15.09
6	56.0	55.4	18.97	18.38	18.19	17.4	44.88	44.37	44.09	43	464.5	6.92	16.39
7	56.0	55.3	18.72	18.42	17.86	16.93	44.01	43.58	43.21	42.05	531.9	7.43	17.59
8	56.2	55.5	17.99	17.61	16.94	16.41	43.92	43.4	43	41.98	527.9	7.59	17.98
9	56.3	55.5	18.03	17.6	16.88	16.33	43.2	42.7	42.29	41.25	608.4	8.04	19.04
10	56.3	55.3	17.82	17.5	16.82	16.3	42.69	42.13	41.74	40.79	668.4	8.28	19.62
11	56.2	55.2	17.79	17.34	16.7	16.13	42.14	41.54	41.09	40.21	753.5	8.5	20.13
12	56.0	54.9	17.6	16.6	16.66	16.23	41.45	40.71	40.41	39.73	871.8	8.75	20.72
13	55.9	54.6	17.64	16.74	16.5	16.25	41.14	40.4	40.04	39.41	931.1	8.81	20.88
14	56.0	54.6	17.52	16.66	16.43	16.19	40.95	40.22	39.84	39.21	1000	8.93	21.16
15	56.2	54.5	17.41	16.61	15.99	15.86	40.69	39.98	39.45	38.86	1176	9	21.31
16	56.3	52.5	17.34	16.27	16.12	15.75	39.35	38.67	38.14	37.85	2534	8.57	20.28

Table E.12 continued

Read	V_{a1} (m^3/s)	V_{a2} (m^3/s)	V_{a3} (m^3/s)	V_{a4} (m^3/s)	m_{at} (kg/s)	Q_{a1} (kW)	Q_{a2} (kW)	Q_{a3} (kW)	Q_{a4} (kW)	Q_{at} (kW)	EB (%)
1	0.083	0.078	0.081	0.083	0.358	2.552	2.443	2.638	2.617	10.25	-7.17
2	0.094	0.085	0.089	0.09	0.395	2.774	2.557	2.785	2.73	10.85	-5.44
3	0.101	0.098	0.1	0.101	0.442	2.92	2.854	2.996	2.97	11.74	-4.05
4	0.112	0.106	0.111	0.111	0.488	3.239	3.067	3.276	3.223	12.81	-1.1
5	0.13	0.121	0.125	0.125	0.554	3.751	3.51	3.671	3.595	14.53	0.43
6	0.143	0.135	0.138	0.141	0.619	4.141	3.908	4.004	4.054	16.11	2.17

Table E.12 continued

7	0.158	0.144	0.152	0.155	0.677	4.449	4.058	4.317	4.372	17.2	1.34
8	0.154	0.149	0.152	0.153	0.675	4.461	4.283	4.424	4.397	17.57	1.21
9	0.163	0.158	0.165	0.167	0.727	4.575	4.451	4.71	4.683	18.42	0.03
10	0.176	0.175	0.173	0.176	0.78	4.902	4.831	4.84	4.845	19.42	2.21
11	0.192	0.187	0.187	0.183	0.837	5.244	5.076	5.141	4.972	20.43	4.55
12	0.201	0.195	0.197	0.192	0.88	5.402	5.298	5.288	5.098	21.09	4.72
13	0.206	0.2	0.2	0.198	0.9	5.436	5.338	5.323	5.179	21.28	4.83
14	0.211	0.206	0.206	0.2	0.922	5.557	5.473	5.458	5.213	21.7	5.4
15	0.214	0.207	0.207	0.205	0.935	5.611	5.473	5.497	5.333	21.91	5.64
16	0.217	0.213	0.212	0.21	0.961	5.415	5.411	5.302	5.287	21.42	8.23

Table E.13: The measured experimental data obtained from experiments performed at a steam temperature of 60 °C.

Read	T_{si} (°C)	T_{so} (°C)	T_{ai1} (°C)	T_{ai2} (°C)	T_{ai3} (°C)	T_{ai4} (°C)	T_{ao1} (°C)	T_{ao2} (°C)	T_{ao3} (°C)	T_{ao4} (°C)	Δp (Pa)	m_{sc} (g/s)	Q_s (kW)
1	60.15	60.04	19.88	19.14	18.48	18.09	51.62	51.19	50.83	49.46	154.8	4.17	9.53
2	60.3	60.06	19.99	19.12	18.72	18.36	51.57	50.91	50.44	49.15	228.6	5.34	12.18
3	60.65	60.37	20.16	19.43	18.79	18.28	51.01	50.33	49.87	48.65	291.8	6.22	14.19
4	60.57	60.22	19.89	19.48	18.76	18.35	50.08	49.37	48.92	47.8	354.5	6.79	15.49
5	60.24	59.69	19.87	19.39	18.69	18.34	48.8	48.09	47.66	46.65	427.3	7.35	16.79
6	60.08	59.46	19.94	19.45	18.81	18.39	47.79	47.06	46.68	45.66	491.5	7.89	18.02
7	60.2	59.52	20.03	19.38	18.95	18.51	46.82	46.05	45.69	44.68	589.1	8.45	19.3
8	60.56	59.72	20	19.37	19	18.44	46.13	45.41	45.05	44.01	684.9	8.96	20.45
9	60.65	59.78	19.87	19.51	19.02	18.56	45.44	44.74	44.37	43.42	806	9.36	21.36
10	60.29	59.23	19.6	19.33	18.77	18.23	44.55	43.9	43.54	42.55	938.9	9.65	22.03
11	60.45	59.25	19.43	19.03	18.39	18.02	44.38	43.71	43.24	42.27	1079	9.78	22.33
12	60.75	57.64	18.93	18.79	18.11	17.66	42.95	42.24	41.65	41.19	2847	9.67	22.1
13	59.75	55.76	19.05	18.61	18.43	18.04	41.27	40.45	40.02	39.88	3538	9.69	22.18
14	59.68	48.01	18.97	18.67	18.17	17.84	33.26	32.37	31.78	34.78	8666	10.35	23.8

Table E.13 continued.

Read	V_{a1} (m^3/s)	V_{a2} (m^3/s)	V_{a3} (m^3/s)	V_{a4} (m^3/s)	m_{at} (kg/s)	Q_{a1} (kW)	Q_{a2} (kW)	Q_{a3} (kW)	Q_{a4} (kW)	Q_{at} (kW)	EB (%)
1	0.042	0.061	0.057	0.057	0.235	1.465	2.13	1.998	1.947	7.54	-16
2	0.07	0.085	0.08	0.081	0.343	2.419	2.946	2.772	2.726	10.86	-4.94

Table E.13 continued.

3	0.092	0.103	0.098	0.098	0.426	3.102	3.492	3.342	3.27	13.21	-1.53
4	0.112	0.116	0.114	0.114	0.497	3.683	3.816	3.764	3.699	14.96	1.71
5	0.131	0.134	0.132	0.129	0.577	4.177	4.243	4.227	4.045	16.69	4.11
6	0.146	0.142	0.145	0.144	0.635	4.493	4.34	4.473	4.371	17.68	2.47
7	0.162	0.169	0.166	0.166	0.729	4.803	4.98	4.924	4.83	19.54	5.2
8	0.186	0.188	0.183	0.182	0.815	5.385	5.421	5.308	5.181	21.3	7.65
9	0.201	0.201	0.197	0.196	0.878	5.692	5.63	5.553	5.441	22.32	7.78
10	0.212	0.21	0.207	0.207	0.927	5.901	5.762	5.725	5.635	23.02	7.69
11	0.215	0.214	0.21	0.211	0.942	5.973	5.892	5.83	5.727	23.42	8
12	0.219	0.218	0.215	0.216	0.967	5.89	5.723	5.68	5.722	23.02	7.38
13	0.238	0.233	0.23	0.231	1.044	5.936	5.747	5.613	5.692	22.99	6.91
14	0.363	0.35	0.356	0.358	1.636	5.991	5.545	5.612	6.963	24.11	4.52

Table E.14: The measured experimental data obtained from experiments performed at a steam temperature of 65 °C.

Read	T_{si} (°C)	T_{so} (°C)	T_{ai1} (°C)	T_{ai2} (°C)	T_{ai3} (°C)	T_{ai4} (°C)	T_{ao1} (°C)	T_{ao2} (°C)	T_{ao3} (°C)	T_{ao4} (°C)	Δp (Pa)	m_{sc} (g/s)	Q_s (kW)
1	64.35	64.24	22.53	20.84	19.64	19.17	55.26	55.04	54.29	53.53	120.2	4.36	10.25
2	64.29	64.17	22.44	20.59	19.73	19.2	55.34	54.79	53.97	53.19	166	5.2	12.21
3	65.34	65.16	21.95	20.38	19.77	19.4	55.42	54.71	53.85	53.19	248.8	6.31	14.8
4	65.48	65.28	21.77	20.55	19.94	19.52	54.9	54.08	53.21	52.54	283.3	6.88	16.14
5	65.45	65.17	21.64	20.48	19.85	19.63	53.84	52.87	52	51.35	360.3	7.6	17.83
6	65.69	65.37	21.51	20.39	20.02	19.67	53.27	52.3	51.5	50.9	395.6	8.15	19.11
7	65.64	65.27	21.38	20.49	20.17	19.72	52.36	51.32	50.55	49.91	457.4	8.75	20.51
8	65.43	65	21.34	20.3	19.99	19.65	51.44	50.3	49.54	48.9	515.4	9.2	21.58
9	65.33	64.84	21.19	20.27	19.93	19.59	50.64	49.52	48.71	48.03	575	9.54	22.38
10	65.26	64.68	21.05	19.89	19.67	19.29	49.72	48.49	47.64	46.9	684.7	10.08	23.65
11	65.26	64.55	20.98	19.67	19.23	18.86	49.04	47.7	46.77	45.98	814.8	10.48	24.59
12	65.3	64.54	20.99	19.65	19.13	18.75	48.81	47.49	46.46	45.64	841.5	10.71	25.11
13	65.39	64.49	21	19.74	18.99	18.76	48.38	47.04	45.96	45.11	1026	10.93	25.62
14	65.77	62.64	20.88	19.59	18.79	18.46	46.88	45.43	44.21	43.99	3493	10.76	25.22
15	65.66	61.8	20.83	19.78	18.7	18.43	45.62	44.16	42.79	42.93	4055	10.64	24.95
16	65.64	62.13	20.8	19.64	18.63	18.33	45.8	44.29	42.92	43.03	3792	10.89	25.52
17	65.58	59.3	20.74	19.75	19.12	18.81	43.05	41.94	41.01	42.12	6270	10.72	25.14
18	65.58	59.95	20.99	19.96	18.62	18.45	43.75	42.24	40.74	41.69	5724	10.97	25.72
19	65.53	58.12	20.97	20.06	18.75	18.61	42.06	40.64	39.16	40.85	7315	10.94	25.65

Table E.14 continued.

20	65.25	54.49	20.23	19.2	18.46	18.24	38.44	37.07	36.53	39.58	9807	11.22	26.32
21	65.79	52.76	21.45	20.31	19.57	19.42	36.72	35.23	35.31	38.7	11721	11.09	26.01
22	65.31	50.18	20.12	19.26	18.32	18.07	33.91	32.53	33.49	37.11	12745	10.89	25.54
23	65.4	49.69	20.11	19.26	18.28	17.97	33.72	32.29	33.28	37.02	13215	11.15	26.16
24	65.35	51.34	21.44	20.64	19.85	19.63	35.08	33.76	34.4	37.75	12180	11.32	26.54
25	65.38	47.83	20.19	19.78	18.5	17.88	32.23	31.23	32.35	35.92	14183	11.27	26.43

Table E.14 continued

Read	V_{a1} (m^3/s)	V_{a2} (m^3/s)	V_{a3} (m^3/s)	V_{a4} (m^3/s)	m_{at} (kg/s)	Q_{a1} (kW)	Q_{a2} (kW)	Q_{a3} (kW)	Q_{a4} (kW)	Q_{at} (kW)	EB (%)
1	0.057	0.061	0.06	0.058	0.252	1.995	2.238	2.234	2.165	8.632	-9.01
2	0.074	0.078	0.077	0.075	0.326	2.621	2.886	2.854	2.757	11.12	-2.3
3	0.094	0.096	0.097	0.094	0.407	3.374	3.558	3.552	3.431	13.92	-0.35
4	0.107	0.111	0.111	0.107	0.468	3.825	4.01	4	3.826	15.66	2.26
5	0.127	0.129	0.131	0.127	0.554	4.398	4.535	4.583	4.395	17.91	5.14
6	0.137	0.14	0.141	0.138	0.6	4.71	4.843	4.824	4.706	19.08	4.25
7	0.152	0.152	0.158	0.154	0.666	5.097	5.098	5.246	5.077	20.52	4.12
8	0.157	0.159	0.172	0.168	0.711	5.136	5.215	5.558	5.366	21.28	2.49
9	0.17	0.176	0.186	0.18	0.774	5.467	5.636	5.871	5.623	22.6	4.67
10	0.191	0.194	0.202	0.198	0.856	5.982	6.097	6.225	6.021	24.33	6.21
11	0.203	0.208	0.216	0.211	0.916	6.247	6.411	6.551	6.318	25.53	6.95
12	0.209	0.212	0.222	0.217	0.94	6.383	6.479	6.682	6.47	26.01	6.68
13	0.219	0.222	0.232	0.23	0.989	6.565	6.674	6.924	6.714	26.88	7.77
14	0.226	0.226	0.239	0.237	1.02	6.464	6.463	6.749	6.718	26.39	7.63
15	0.242	0.246	0.257	0.255	1.104	6.631	6.656	6.913	6.969	27.17	11.26
16	0.244	0.246	0.258	0.255	1.107	6.741	6.734	6.981	7.024	27.48	10.15
17	0.273	0.269	0.266	0.266	1.198	6.813	6.699	6.568	6.978	27.06	10.18
18	0.262	0.265	0.282	0.278	1.207	6.63	6.596	7	7.242	27.47	9.42
19	0.28	0.283	0.304	0.301	1.303	6.598	6.537	7.018	7.521	27.67	10.33
20	0.327	0.323	0.324	0.322	1.459	6.734	6.563	6.673	7.75	27.72	8.07
21	0.376	0.369	0.381	0.385	1.717	6.568	6.324	6.886	8.434	28.21	10.77
22	0.406	0.394	0.411	0.413	1.851	6.434	6.029	7.175	8.94	28.58	13.57
23	0.408	0.393	0.411	0.414	1.852	6.375	5.908	7.096	8.961	28.34	10.65
24	0.417	0.419	0.425	0.428	1.928	6.538	6.353	7.125	8.841	28.86	10.92
25	0.446	0.446	0.457	0.459	2.069	6.196	5.911	7.306	9.456	28.87	11.36